The book describes the creation of new and improvement of existing methods for studying nuclear quadruple resonance by solving an important application problem – the development of cheap, portable, digital, multipulse spectrometer to study the sensor properties, structure, defects of layered and organic semiconductors.
The experimental methods described in the book can find effective application in various branches of science and national economy. It is materials science (symmetry research; structures, phase transitions and crystal defect analysis); solid-state electronics (control of the structure of layered and organic semiconductors, creation of radiation-resistant devices on their basis); life safety (remote detection of explosives and drugs); radio engineering and communication technologies (algorithms for generating and processing information signals based on programmable logic integrated circuits), etc.

Andrii Samila is Doctor of Engineering, Associate Professor, Vice Rector for Scientific Research of Yuriy Fedkovych Chernivtsi National University.
Leonid Politanskyi is Doctor of Engineering, Professor and Chief of the Radio Engineering and Information Security Department, Yuriy Fedkovych Chernivtsi National University.

9 786203 839555

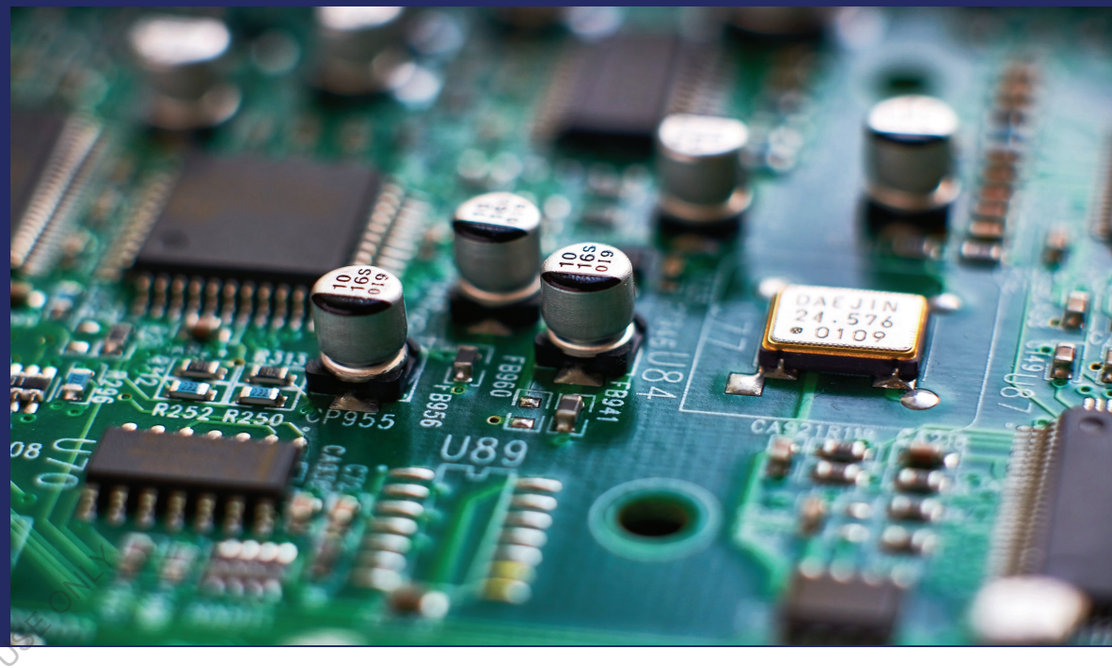

Andrii Samila
Leonid Politanskyi

Radioelectronics and information technologies in physical experiments

Part 1. General principles of development and applications of a simple handmade pulsed NQR device

LAP LAMBERT Academic Publishing

Andrii Samila
Leonid Politanskyi

Radioelectronics and information technologies in physical experiments

Andrii Samila
Leonid Politanskyi

Radioelectronics and information technologies in physical experiments

Part 1. General principles of development and applications of a simple handmade pulsed NQR device

LAP LAMBERT Academic Publishing

Imprint

Cover image: www.ingimage.com

Publisher:
LAP LAMBERT Academic Publishing
is a trademark of
International Book Market Service Ltd., member of OmniScriptum Publishing Group
17 Meldrum Street, Beau Bassin 71504, Mauritius
Printed at: see last page
ISBN: 978-620-3-83955-5

Andrii Samila
Leonid Politanskyi

Radioelectronics and information technologies in physical experiments

Part 1. General principles of development and applications of a simple handmade pulsed NQR device

Preface

The proposed book is dedicated to methods for observing a unique physical phenomenon in solids, namely nuclear quadrupole resonance (NQR) which has recently attracted the attention of both scientists engaged in basic research and application scientists. The rapid development of integral electronics and high-performance algorithms for processing information messages stimulated progress in the field of physical experiment. This is especially evident in the fields of radio physics, chemistry, medicine, biology and others. The results of research in recent years have opened up a world of unusual phenomena that enable the practical implementation of experimental methods of NQR radio spectroscopy and the use of the latter for further detection of new physical processes or effects in substances with quadrupole atomic nuclei. Promising in this direction is the development of inexpensive portable spectrometers with an integrated compute core, based on new algorithms for information transformations of free induction decay signal in the transmit and receive path and visualization of NQR spectra.

The relevance of the subject matter of this book is largely due to the variability of the applied application of the NQR method. High accuracy and informative value of this method allows its effective implementation in various fields of science and technology: materials science (study of symmetry, structure, phase transitions and analysis of crystal defects); solid-state electronics (control of the structure of semiconductors when creating radiation resistant devices on their basis); counter-terrorism and national security (remote detection of explosives and drugs). The development of theoretical aspects of the construction of systems for observation and registration of superweak resonance signals in materials with quadrupole atomic nuclei and their practical implementation is an urgent research direction. This enables effective development of modern radio engineering devices for radio spectroscopy, spintronics, magnetic resonance diagnostics, semiconductor sensors (precision sensors of temperature, pressure and weak magnetic fields). The use of NQR in the field of national security is especially relevant – the identification of explosives and drugs of small volumes in non-metallic containers. The methods of pulsed Fourier and relaxation spectroscopy of nuclear quadrupole resonance become relevant in the remote detection of resonance signals of the 14N isotope in solids. The results obtained by NQR are also unique in the study of complex multiplet spectra, which is characteristic of layered semiconductors due to polytypic modifications of their crystal structure.

Due to increasing rigidity of requirements for stability, accuracy, the influence of destabilizing factors on the technical parameters of modern radio equipment, the NQR monitoring methods require further development and improvement. Ensuring the invariance of the parameters of radioelectronic means of pulsed spectroscopy of materials with quadrupole atomic nuclei is one of the important requirements related to their miniaturization, energy and cost characteristics. This imposes a number of limitations on the existing analytical methods of their synthesis and increases the relevance of research in the direction of developing theoretical positions. At the same time, considerable emphasis should be placed on increasing the value of signal/noise ratio, provided by the spectrometer, to the required level for error-free detection of the NQR signal in the investigated small-volume substances with mass from tenths to several grams. Also, due attention should be given to the development of highly efficient methods for the formation of special multi-pulse sequences of nanosecond time intervals for stochastic NQR technique.

The book deals with the synthesis of structural, configurational and schematic electrical diagrams of radioelectronic devices of pulsed spectroscopy of nuclear quadrupole resonance with improved signal and energy characteristics. It is precisely the minimization of the duration of the experiment and the increase in energy efficiency that are one of the key requirements for modern portable devices for radiophysical research, which contributes to their effective use on unmanned aerial vehicles. The book not only reveals the concept of methods of pulsed NQR spectroscopy, but also in a logical sequence highlights the patterns of physical processes of registration of weak free induction decay signals. Analyzed: models of radio engineering systems of the pulse method of NQR observation; methods for configuring devices based on the syntax for modeling dynamic modes of logical structures; schematic models of functional modules of radio spectrometers and their experimental studies; implementation of the NQR data collection system. This is the first book in the series “Radioelectronics and information technologies in physical experiments” dedicated to experimental methods of pulsed NQR spectroscopy. It will be useful for researchers, graduate students and students working in this field of knowledge.

Chernivtsi, Ukraine Andrii Samila

About the Authors

Andrii Samila is Doctor of Engineering, Associate Professor of the Radio Engineering and Information Security Department, Chief Scientific Officer at the Nuclear Quadrupole Resonance Spectroscopy Lab, Yuriy Fedkovych Chernivtsi National University, and is currently Vice Rector for Scientific Research of Yuriy Fedkovych Chernivtsi National University. His research interests include radio engineering devices, telecommunication means theory and focus on the design and development of portable equipment for radio spectroscopic research methods, research of physical processes in solids by nuclear quadrupole resonance. He is led on the 'Development of NQR hardware and software applications for explosives and narcotics detection' project and was co-led on the 'Development of portable NQR radiospectrometer with improved signal and energy characteristics' project. His recent publications include *A Low-Cost Digital Pulsed Coherent Spectrometer for Investigation of NQR in Layered Semiconductor GaSe and InSe Crystals* (2020) with Oleksandra Hotra. He has published in a range of journals, notably in *Electronics, Solid State Nuclear Magnetic Resonance, Telecommunications and Radio Engineering, Measurement, Progress in Electromagnetics Research, Metrology and Measurement Systems and Semiconductors.*

Leonid Politanskyi is Doctor of Engineering, Professor and Chief of the Radio Engineering and Information Security Department, Yuriy Fedkovych Chernivtsi National University. His research interests include:

1) Physical constraints in nanostructured multilayer semiconductor structures.
2) Investigation of properties and possibilities of application of chaotic oscillations generated by multidimensional nonlinear systems in infocommunication systems.
3) Investigation of the properties of semiconductor metamaterials for broadband energy transmission of electromagnetic oscillations.
4) Development of methods to increase the noise immunity of information transmission systems based on chaotic and fractal signals.

Contents

Chapter 1
Nuclear quadrupole resonance and methods of nondestructive testing of parameters of primary electronic materials

1.1 Nuclear quadrupole resonance

The method of nuclear quadrupole resonance (NQR) is based on the absorption of radio wave energy by changing the orientation of the quadrupole moments of atomic nuclei in a non-uniform electric field created by external charges relative to the nucleus. The levels of quadrupole energy in solids arise when quadrupole moments interact with a non-uniform electric field at the location of the resonating nucleus, therefore the NQR spectrum reflects the distribution of electron density near a certain atom. Therein lies the uniqueness of the NQR method in the study of the subtle features of the structure of chemical compounds [1, 2].

At the present stage of development of pulsed radio spectroscopy, a significant number of scientific and experimental developments have been presented. Scientific papers cover a wide segment of resonance spectroscopy: the development of experimental methods for observing NQR [1–6]; the development of hardware and software tools for digital processing of microwave signals in real time [7, 8]; studies of the intramolecular structure and physicochemical properties of substances, development of NQR detectors of explosives and narcotic substances, nuclear magnetic resonance (NMR) tomography, etc. [9–13]. The choice of objects for research is to a certain extent limited by the presence of nuclei with a quadrupole moment in the substance under study (nuclear spin $I \geq 1$). However, the periodic system contains a sufficiently large number of elements with a nonzero nuclear quadrupole moment. The data on stable isotopes of some nuclei are summarized in Table 1.1 [14, 15]. The NQR method allows one to study the distribution of electron density in a large number of chemical compounds, which include atoms of elements containing quadrupole nuclei.

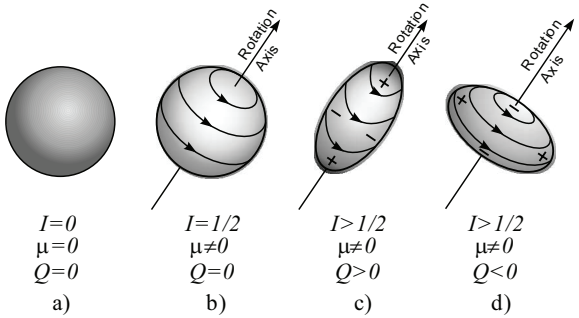

Fig. 1.1 Qualitative representation of the types of nuclei, (I – spin nucleus, μ – magnetic moment, Q – quadrupole moment): non-quadrupole nuclei (a, b); quadrupole nuclei (c, d) with different sign of quadrupole moment and $I > ½$ [16]

Table 1.1 Characteristics of stable isotopes of nuclei with spin $I \geq 1$

Element	Mass number	Natural contents	Nucleus spin, I	Magnetic moment	Gyromagnetic relation, (Hz · Gs^{-1})	Quadrupole moment, $Q \cdot 10^{-14}$ cm^2
N	14	99.635	1	0.40357	3076	0.02
Na	23	100	3/2	2.2161	1126.2	0,1
Cl	35	75.4	3/2	0.82089	4172	-0.0797
Cl	37	24.6	3/2	0.68329	3472	-0.0621
Cu	63	69.1	3/2	2.2206	1128.5	-015
Cu	65	30.9	3/2	2.3790	1209	-014
Ga	69	60.2	3/2	2.0108	1021.8	0.19
Ga	71	39.8	3/2	2.5549	1298.4	0.12
In	113	41.6	9/2	5.4960	9310	1.144
In	115	95.84	9/2	5.5072	9329	1.161

The charges in the atomic nucleus precess around the axis coinciding with the direction of the nuclear spin, and, during the averaging period, the charges outside the nucleus almost do not change their position. Thus, the charge distribution in the nucleus can be considered axially symmetric. In the coordinate system, whose z axis is directed along the nucleus symmetry axis, the off-diagonal terms of the quadrupole moment tensor Q_{jk} go to zero, and the diagonal terms are related by:

$$eQ_{xx} = eQ_{yy} = -eQ_{zz} / 2 .$$

As a result, the quadrupole moment tensor is determined through one component, which is called the nuclear quadrupole moment:

$$eQ_{zz} = \int \rho(3z^2 - r^2) d\tau , \qquad (1.1)$$

where ρ is the density of charges in the nucleus; $d\tau$ is the volume element in the x, y, z coordinate system tightly coupled to the nucleus. In the case of a sphere – the right-hand side of Eq.(1.1) is zero, so the quadrupole moment characterizes the deviation of charges in the nucleus from the spherical symmetry.

The electronic environment of a quadrupole nucleus in a molecule that does not have spherical symmetry creates an inhomogeneous electric field, which is characterized by its intensity gradient eq in the nucleus (Fig. 1.1) [16]. The interaction of the nucleus, which has an electric quadrupole moment eQ, with the field gradient eq takes place. The energy of this interaction depends on the orientation of the ellipsoidal quadrupole nucleus relative to the system of principal axes of the electric field gradient tensor, and its measure is the quadrupole interaction constant e^2qQ.

When calculating the levels of quadrupole energy, it is customary to distinguish two cases. The simplest of these is the case of axial symmetry of the electric field

gradient [17, 18]. The interaction energy of nuclear and electron charges can be written in the classical form:

$$W_Q = \int \rho V d\tau ,$$

where ρ is charge density in the nucleus; V is potential created by electron shell at the nuclear point; $d\tau$ is element of nuclear volume.

Expanding the potential in Taylor's series, after transformations we get

$$W_Q = \frac{eQq_{zz}}{4I(2I-1)}[3m^2 - I(I+1)], \tag{1.2}$$

where eQq_{zz} is the value of quadrupole coupling; I is nuclear spin; m is magnetic quantum number. Expression (1.2) is valid only for the case of $q_{xx} = q_{yy}$, where q_{xx}, q_{yy}, q_{zz} are components of the gradient of crystal electrical field.

In crystals, the average field gradient is constant in time and approximately the same for all the nuclei of the sample. Therefore, one can observe the spectrum corresponding to transitions of a given type of nuclei between levels of quadrupole energy. Eq.(1.2) allows estimating the quadrupole resonance frequency, given that the selection rule has the form $\Delta m = \pm 1$. Fig. 1.2 shows the level of quadrupole energy for spins 3/2, 5/2, 7/2, and 9/2, as well as the respective transitions. In the case of a 9/2 spin, there are four transition frequencies.

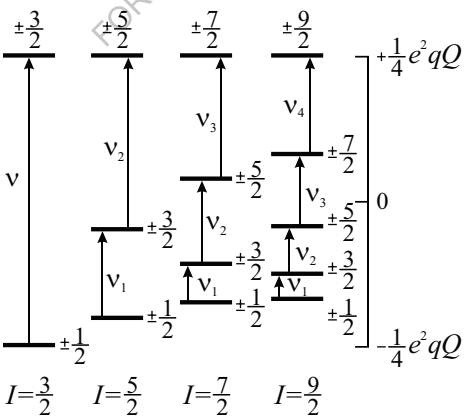

Fig. 1.2 Levels of nuclear quadrupole energy for four spin values in the case of axial symmetry of the electric field gradient

In [16, 19], considered is the case when the assumption of axial symmetry of the electric field gradient does not hold. Usually, to characterize the degree of deviation of the gradient from axial symmetry, an asymmetry parameter is introduced:

$$\eta = \left| \frac{q_{xx} - q_{yy}}{q_{zz}} \right|.$$

In this case:

$$\left.\begin{aligned} q_{xx} &= \left(-\frac{1}{2} + \frac{\eta}{2} \right) q_{zz}, \\ q_{yy} &= \left(-\frac{1}{2} - \frac{\eta}{2} \right) q_{zz}. \end{aligned}\right\}$$

The magnitude of the electric field gradient in the immediate vicinity of the resonating nucleus depends on the type of wave function or, in other words, on the distribution of charges near the nucleus. The gradient of the electric field with a spherically symmetric distribution of charges is zero. Therefore, closed electron shells of ions and valence *s*-electrons do not affect the NQR spectrum (of course, if polarization effects that distort their spherical symmetry are not taken into account). Electrons of non-spherical *d*- and *f*-shells with a low density in the nucleus, affect significantly less than electrons of *p*-shells (the contribution to the field gradient is less than 10% of the contribution of *p*-electrons with the same principal quantum number). It can be assumed that the main contribution in quadrupole interactions is made by valence *p*-electrons [18]. So, the quadrupole interaction constants and NQR frequencies can be interpreted in terms of *p*-electron density near the nucleus under study and, especially simply, used to determine relative p-electron densities in a number of homogeneous molecules.

1.2 Continuous wave and pulse methods for observing NQR

Experimental methods for observing resonant NQR frequencies are divided into continuous wave and pulse. In the continuous wave method, the test substance is irradiated with a variable radio frequency field. When passing through resonant frequencies, the absorption of the energy of this field by quadrupole nuclei is measured. Fig. 1.3 shows the operating principle of a continuous radio spectrometer for the study of solids.

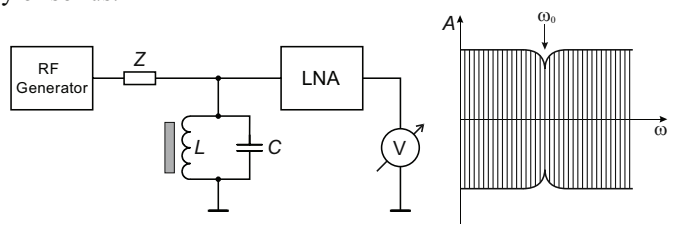

Fig. 1.3 The scheme of the continuous wave NQR experiment

In this case, the sensitive NQR sensor is the oscillatory circuit with the sample connected to the radiofrequency (RF) generator via communication impedance Z_{com}. The resonance is detected by the absorption of high-frequency energy in the LC-circuit, observed in the form of modulation of the oscillation level of the generator at the frequency ω_0. The detected resonance signal is amplified by an amplifier with a low inherent noise level and is fed to the registration device (V). At weak signal levels, as a rule, low frequency (LF) modulation of the NQR effect or periodic change of the external magnetic field is used. In order to improve the signal/noise ratio, further processing of the signal lies in narrowband amplification and demodulation using a synchronous detector. For particularly weak signal-to-noise ratios, digital accumulation and averaging of resonance spectra can be used.

Traditional stationary methods of observing NMR and NQR are now almost completely superseded by pulsed Fourier-spectroscopy. Pulsed NQR observation methods are widely used to solve various problems of solid state physics.

In the pulsed NMR method, besides spectral characteristics, additional information is obtained from the results of measuring the relaxation times T_2 and T_1, which are the result of the interaction inside the spin system (this process is characterized by the transverse relaxation time T_2) and other degrees of freedom in the lattice (this is the spin-lattice relaxation time T_1). These parameters characterize the dynamics of the lattice and spins. Using stationary methods, it is hardly ever possible to determine the actual time of T_2.

The impulse NQR method consists in observing the response of a nuclear spin system (induction or echo signals) to a short and powerful radiofrequency pulse or a series of pulses [6, 20, 21]. The radiofrequency pulse causes the precession of the nuclear magnetization vector, which disappears after a period of $T_2^* = 1/\delta$ (δ – the width of the absorption line). This makes possible the reduction of the multicomponent spectrum observation time comparing with the stationary method, the resonance spectrum of which is recorded by continuous transit of frequency at low power of the excitation generator.

By irradiating a sample with a radiofrequency field at a resonant frequency $\omega = \omega_0$ in a rotating coordinate system, the magnetic moment vector $\vec{M}$ is influenced bt an effective field $\vec{H}_{eff} = \vec{H}_1$, directed along the axis x' (Fig. 1.4). Therefore, in this system $\vec{M}$ will rotate around an axis x' in a plane $Z'OY'$ with an angular frequency $\omega_1 = \gamma H_1$. When the field $\vec{H}_1$ is turned on for a short time t_p, the moment vector will turn at an angle

$$\theta = \omega_1 t_i = \gamma H_1 t_i .$$

The pulse duration must be chosen according to the condition $\theta = \omega_1 t_p = \pi / 2$, i.e.

$$t_p = \frac{\pi}{2\gamma H_1}.$$

Under this condition, after the completion of pulse impact, the moment will be oriented along the axis y'. Such a pulse is called a 90-degree, or π/2-pulse. After $\vec{H}_1$ is turned off, the magnetic moment will be fixed in the moving system. In the laboratory coordinate system, it will precess at an angular frequency $\omega = \gamma H_0$, keeping its orientation perpendicular to $\vec{H}_0$.

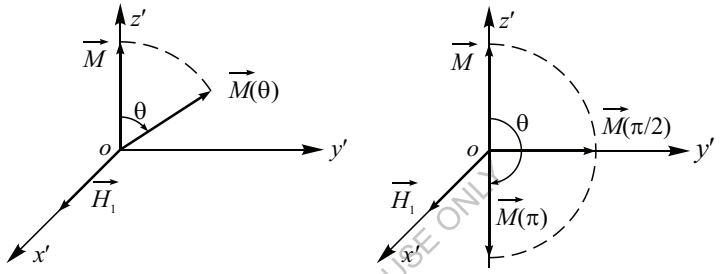

Fig. 1.4 Influence on a sample of a radiofrequency field at frequency $\omega = \omega_0$

If the sample is in a coil, the axis of which lies in the XOY plane, an electromotive force (e.m.f.) resulting from the spin precession, will be induced in it, which can be observed in free induction decrease. If all spins were independent and precessed at the same frequency, e.m.f. would remain constant. However, due to interaction with the environment, frequencies of the spins differ. The distribution of the spins by frequency is in the form of a resonant line. Therefore, phase unbalance of spins in the plane XOY occurs and the signal drops to zero. The mathematical model of the signal free induction decay (FID) can be represented by the exponential dependence

$$M_1 = M_0 e^{-t/T_2}.$$

If one writes down FID and applies the Fourier-transformation of the decay function:

$$J(\omega) = \int_{-\infty}^{\infty} G(t) e^{-i\omega t} dt,$$

the spectral line is obtained.

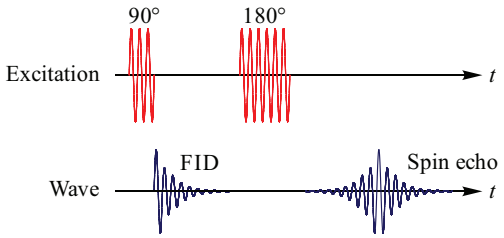

Fig. 1.5 NQR signal in the form of FID and spin echo

To observe the spin echo Hahn and the authors used imitative expansion of the resonance line by creating a significant inhomogeneity of the magnetic field in the sample ΔH_0, which corresponds to the frequency interval $\Delta\omega = \gamma\Delta H_0$. If $1/\gamma\Delta H_0 = T_2' << T_2$, the signal decay will occur much faster according to the expression $\exp\left(-t/T_2^*\right)$, since it will be determined by the effective relaxation time $T_2' << T_2$:

$$\frac{1}{T_2^*} = \frac{1}{T_2} + \frac{1}{T_2'} = \frac{1}{T_2} + \gamma\Delta H_0.$$

Let's discuss the formation of a spin echo. After the action of π/2-pulse for better understanding we will consider the total vector $\vec{M}$, as one consisting of three spins and directed along the axis y' of the moving coordinate system (Fig. 1.6).

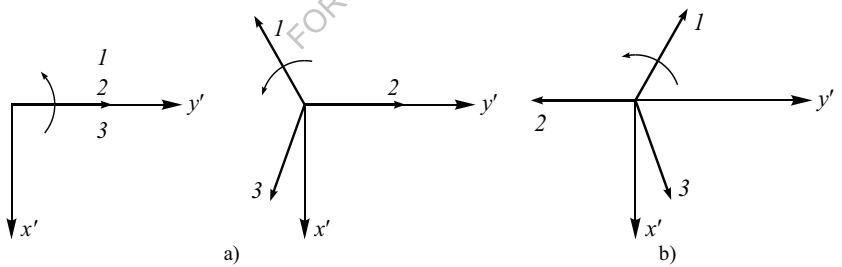

Fig. 1.6 Change in the magnetic moments of the spin system: after the action of the π/2-pulse (a); after the action of the π-pulse (b)

For a time interval equal to several T_2, the phase will be unbalanced in a plane of XOY. We assume that the spin «2» precesses at a Larmor frequency $\omega_0 = \gamma H_0$, while the frequencies of the spins «1» and «3» are $\omega_1 > \omega_0 > \omega_3$. The application of a π-impulse after a time τ will cause the rotation of each of the vectors by 180° around the axis x'. As a result, the vector orientation will change to the opposite – the «slow» vector will be ahead, and the «fastest» vector will be behind. In such a situation, the vectors will come in-phase after the time of 2τ from the beginning of the cy-

cle, and we will get the echo signal (Fig. 1.7).

Carr and Parcel suggested to apply π-pulses through intervals of $\tau, 3\tau, 5\tau, ..., (2n-1)\tau$, to call forth the occurrence of echo pulses at $t = 2\tau, 4\tau, ..., 2n\tau$. Their amplitude will decrease exponentially with the time of transverse relaxation T_2, which can be determined (Fig. 1.7).

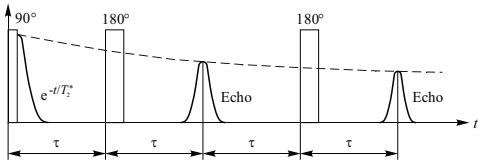

Fig. 1.7 Spin echo formation process

Carr and Parcel suggested to apply π-pulses through intervals of $\tau, 3\tau, 5\tau, ..., (2n-1)\tau$, to call forth the occurrence of echo pulses at $t = 2\tau, 4\tau, ..., 2n\tau$. Their amplitude will decrease exponentially with the time of transverse relaxation T_2, which can be determined.

When observing quadrupole spin echo in polycrystalline samples, a 90°-pulse commonly refers to the shortest pulse at a given voltage of a high-voltage source, when the maximum induction drop is observed. Similarly, the 180°-th pulse gives a minimal induction decay. The observation of the NQR signals in the intervals between pulses of the radiofrequency field allows us to avoid many of the difficulties associated with the presence of the radiofrequency field. However, if frequency of pulse repetition in pulsed methods is sufficiently high, the spin system does not have time to absorb energy between pulses. The intensity of the echo signal drops. This effect is called saturation.

A mathematical model of a cyclic spin-echo sequence can be described by the dependence [20]:

$$S = k\rho\left(1 - e^{-T_R/T_2}\right)e^{-T_E/T_2},$$

where S – the amplitude of the signal after Fourier transformation; k – proportionality factor; ρ – spin density in the research sample; T_R – sequence repeat time; T_E – spin echo duration.

The principles of constructing installations for observing spin echo in magnetic and quadrupole resonances differ little. Since the NQR lines are wider than the NMR lines in liquids, the installation for observing quadrupole spin echo should provide more powerful radio-frequency pulses. In addition, in order to search for weak quadrupole echo signals, it is necessary to have a receiver tunable over a wide frequency range. The principle of pulse NQR observation is shown in Fig. 1.8.

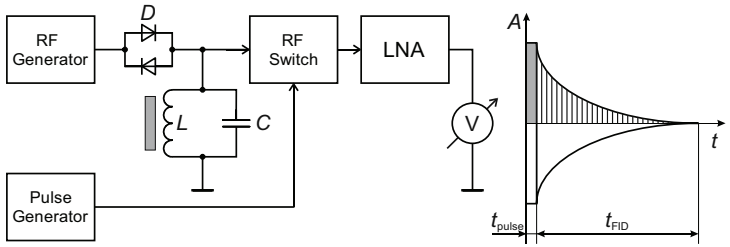

Fig. 1.8 The scheme of the pulse experiment

To observe the spin echo in solids, the condition $t_{pulse} < T_2$ must be met. Otherwise, the induction signal after the action of the 1st pulse does not have time to extinguish before the formation of the echo signal. When observing the latter from various nuclei, it is necessary to change the pulse duration, since the condition of the 90° pulse is of the form (for $\eta = 0$):

$$\alpha\gamma H_1 t_{pulse} = \pi/2,$$

where $\alpha = \sqrt{I(I+1) - m(m+1)}$; I is nuclear spin; m is magnetic quantum number for the lower energy level; t_{pulse} is pulse duration. If $I = 3/2$, then $a = \sqrt{3}$; if $I = 5/2$, then $a = 2\sqrt{2}$. Usually, when a spin echo is observed in solids, one takes $t_{pulse} \sim$ 1-4 μs, with the pulse amplitude reaching several kilovolts. The "dead" time of the receiver on exposure to a powerful pulse at its input should not exceed 3–5 μs. The theoretical foundations of pulse radiospectroscopy methods are given in [19, 22–24].

Usually, in order to clarify the picture of a phenomenon, it is considered that the axis of the coil with a radio frequency field is oriented parallel to the x axis of the electric field gradient tensor. In real conditions, the axis of the coil is oriented arbitrarily relative to the principal axes of the electric field gradient tensor. Then the effective RF field along the x axis will be:

$$H_x = H_1 \sin\theta\cos\varphi,$$

where θ is the angle between the direction H_1 and the z axis; φ is the azimuth angle.

Accordingly, the radiofrequency field component along the y axis is:

$$H_y = H_1 \sin\theta\sin\varphi.$$

These two components excite transitions between NQR levels. Therefore, in the general case, the angles θ and φ will enter the formula for the conditions of 90° pulses. If the sample is taken in powder form, these factors should be averaged over a sphere of unit radius.

Comparison of the sensitivity of the Fourier experiment and slow propagation experiment, obtained from the analysis of the continuous wave and pulse methods, is of the form [25]:

$$\frac{(S/N)_{FTT}}{(S/N)_{ST}} = \left[\frac{3\sqrt{3}}{2\pi}\right]^{1/2} \left[1-\exp(-2t^{\max}/T_2)\right]^{1/2} \left[\frac{\Omega_{\text{total}}}{\Delta\omega}\right]^{1/2} G(T/T_1),$$

where $\Delta\omega = 2/T_2$ is the full width at half-height of the resonance line under study. When deriving this expression, it was assumed that in the slow propagation experiment, in the modulation scheme, detection on sidebands is used, and in the Fourier experiment – quadrature detection. In both cases, matched filtering is employed.

1.3 Promising directions in the development of pulsed radiospectroscopy of materials with quadrupole nuclei of atoms

Fig. 1.9 shows a block diagram of the NQR detection system proposed by Smith in [11]. The generator 1 generates a low-power RF signal with the frequency required for excitation of the resonance. Unit 2 is an amplitude-phase modulator. Unit 3 serving to generate radio pulses works on the principle of a high-speed switch controlled by a sequence of video pulses coming from modulator 2. Centralized control of units 2 and 3 is carried out from a personal computer 4. The RF power amplifier 5 is implemented on the basis of AB class circuitry. The blocking device D1 functions as a single-position switch providing low impedance for the excitation signal and high impedance to the noise generated by the power amplifier. Unit 6 is an NQR probe, which can be reconfigured for matching with the amplifier 5. Unit 7 is used to indicate the settings. Key D2 provides protection of the receiving channel when exposed to high power excitation pulses. The receiver and detector (unit 8) consists of a pre-amplifier and a demodulator for converting the signal into the low-frequency band. From output 8, the signal enters the personal computer (PC) for further processing. Unit 9 is used to notify about the course of the experiment and the occurrence of abnormal situations.

From the considered example it is possible to detect some limitations of traditional solutions of pulsed NQR spectroscopy:

The circuit design of the RF power amplifier makes it impossible to use it in portable applications, since it is active during the entire experiment period and has low energy efficiency. In addition, it introduces additional noise into the NQR probe section.

The signal multiplexing system, built on D1 and D2, makes calibration difficult

during readjustment. For different NQR frequencies, the length of the D2 transmission line must be different to meet the condition $\lambda/4$.

Using a PC can surely provide powerful computing capability and reprogramming versatility. However, energy consumption and considerable size also impede the mobility of the spectrometer.

More modern NQR spectrometers have a coherent device, that is, the phases of high-frequency pulses are strictly fixed in accordance with the objectives of the experiment [26]. So, in the spectrometers of this type, one can apply synchronous signal detection. In the pulsed equipment designed to search for unknown NQR signals, it is necessary to maintain constant phase relationships between the signals of the spin system and the reference signal at any frequency of the operating range of the spectrometer. The reference signal can be fed directly to the input of the receiving device, which mutually compensates for phase shifts occurring in it. Therefore, the main source of phase distortions is the transmit path. To minimize them, it is necessary to reduce the number of cascades in this path and make them broadband. To reduce the leakage of oscillations into the circuit with the sample in the intervals between pulses, it is advantageous to use a generator operating on the harmonics of the fundamental frequency, with a small nonlinear distortion factor. The only high-quality circuit in the transmitting circuit is the output circuit with the sample, since a decrease in its figure of merit leads to a sharp decrease in the signal intensity. Therefore, it is more convenient to use phase distortion compensation. If the voltage signal is applied through the oscillating circuit of the output stage, its phase distortions will be the same as the phase distortions of the signal.

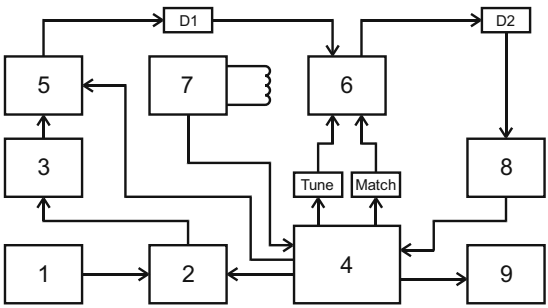

Fig. 1.9 The simplified structure of the NQR pulsed spectrometer: 1 – RF generator; 2 – modulator; 3 – switch; 4 – PC; 5 – transmitter; 6 – NQR probe; 7 – tuning indicator; 8 – receiver; 9 – alert unit [11]

A block diagram of a pulsed coherent spectrometer is shown in Fig. 1.10 [26]. Frequency generator 1 operates in continuous mode. The voltage from its output goes to the gated amplifier 2 and to the frequency multiplier of the reference voltage 3. The sequence of video pulses fed to the input of the gated amplifier is converted into the corresponding sequence of radio pulses, which are fed to a pulse frequency

multiplier. Then the radio pulses are amplified in the output stage, the load of which is an oscillating circuit with sample 4. The reference voltage signal required for a synchronous detector, from the output of the frequency multiplier through a divider and a buffer amplifier 5 is fed to an oscillating circuit. The feedback signals of the spin system and the reference voltage are amplified in broadband receivers 6 and fed to a synchronous detector 7. A low-pass filter 8 with adjustable bandwidth is connected to the detector output. The echo or induction signals from the output of the low-pass filter are fed to an oscilloscope or a storage device 9.

The described scheme is universal and can also be used for relaxation studies. In this case, it is necessary to experimentally measure the law of restoration of energy levels, which requires accurate amplitude measurements at low signal values (signal/noise < 1) and large periods of repetition of probing pulses. Conventional capacitive storages have nonlinear characteristics and are unsuitable for amplitude measurements. Therefore, in the relaxation research, linear multichannel storages are used. In addition, in this case it is desirable to replace the internal generator with an external frequency synthesizer.

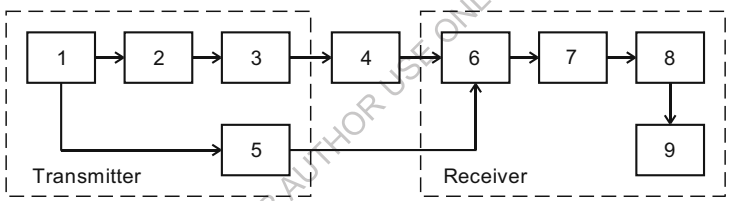

Fig. 1.10 Simplified structure of the coherent NQR spectrometer: 1 – frequency generator; 2 – gated amplifier; 3 – frequency multiplier; 4 – transmitter output stage; 5 – buffer amplifier; 6 – broadband receiver; 7 – synchronous detector; 8 – low-pass filter; 9 – signal registration scheme [26]

In the study of organic matter, including nitrogen content, the intensity of the resonance signals is too weak and direct pulse detection is practically impossible. This is especially true when conducting research in the area of room temperature [12]. The problem is further complicated by the low frequencies of NQR, which are often hundreds of kilohertz. This leads to a very low energy of quantum transitions between the corresponding quadrupole levels $E_Q = \hbar\nu$.

Although direct pulsed methods [6, 23] allow increasing the signal-to-noise ratio at the output of the spectrometer, which depends mainly on the quality of the input device, this is not enough for a reliable identification of impurities introduced or uncontrolled. Increasing the power of radio frequency pulses up to 1 kW or more for coils with a small volume (d = 20 mm) becomes dangerous due to the possibility of electrical breakdowns in an oscillating circuit and sample heating. Another problem is the difficulty in neutralizing the receive path during the action of a powerful RF pulse [6].

The use of combined radiospectroscopy methods can significantly increase the sensitivity of the experiment for a reliable detection of resonance in small volumes of the studied substances. For example, using double resonance NQR-NMR can identify hazardous materials, in particular the resonance signals of the ^{14}N isotope in solids (narcotic and explosive substances in non-metallic containers) [13].

The method of double nuclear quadrupole resonance (DNQR) is used if the sensitivity of direct NQR methods is insufficient due to the location of resonance absorption lines in the low frequency region (<1 MHz) or the small concentration of quadrupole nuclei in the compound [10]. The best way to test the DNQR method is to detect nitrogen. This is due to the fact that the low frequency of nitrogen resonance requires small magnetic fields that do not "collapse" quadrupole transitions. All types of double resonance suggest the presence in the sample of two different spin subsystems interconnected by dipole-dipole interactions: the spin subsystem *A* (with a strong signal of nuclear resonance, more often it is the proton signal from ^{1}H) and the subsystem *B* (investigated quadrupole nuclei). The weak signal of nuclei *B* is observed indirectly by a change in the resonance signal of spins A. Different DNQR methods differ mainly by the conditions in which the energy exchange between subsystems *A* and *B* takes place. On this basis, there are:

- DNQR in a strong magnetic field (rotational coordinate system);
- DNQR in a zero magnetic field (laboratory coordinate system);
- DNQR in a weak magnetic field.

A DNQR in a weak magnetic field is a universal method, since it allows to study both half-integer and integer spins in polycrystalline samples with high efficiency [12, 26].

To increase the sensitivity of detecting NQR signals from NO_2 - groups of explosives, the method of cross-relaxation spectroscopy has been successfully applied [12, 19]. This method, however, leads to the expansion of the NQR line of nitrogen due to the presence of Hahn, Carr-Purcell-Meiboom-Hill magnetic field, as well as to an increase in the harmonics of the fundamental frequency. However, to solve the problem of detecting substances containing NO_2-groups, the latter does not create serious obstacles. The advantage of the double resonance method with cross-relaxation is the possibility of operation at room temperature and without using radiofrequency irradiation of the quadrupole system. The cross-relaxation line of the NQR spectrum is recorded by a slow change in the weak magnetic field.

The structure of the experimental setup for the implementation of a DNQR with cross-relaxation (Fig. 1.11) contains a pulsed NMR spectrometer on protons with an operating frequency of 2.5 MHz. The numerical values of the operating frequency and magnetic field intensity can be set discretely to fit the NMR and NQR resonance conditions. A magnetic field of up to 800 Gs is created by an electromagnetic system.

The considered spectrometer can be used to control the bookmarks of substances in mail (parcels, packages) and in baggage. It is believed that studies on the presence of intercalating impurities can be recorded in samples with a volume of from 1 to 10 g.

When using DNQR methods, reducing the “dead time” of a pulsed spectrometer is of particular importance. Since in this case a nuclear induction response is detected by proton NMR signals, the loss of time to receive also leads to the loss of useful information on the NQR of the nitrogen nuclei. Such a loss is especially noticeable with the cross-relaxation method.

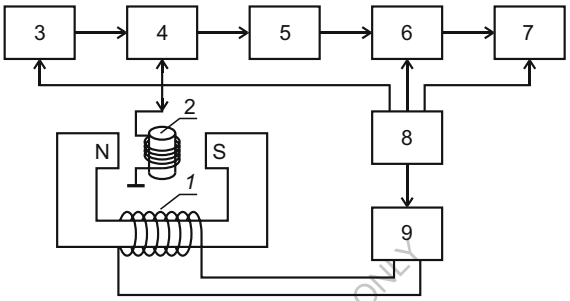

Fig. 1.11 Simplified structure of DNQR spectrometer: 1 – modulation coil; 2 – receiving coil with a sample; 3 – transmitter; 4 – switching circuit; 5 – receiver; 6 – phase detector; 7 – indicator; 8 – pulse sequence programmer; 9 – magnetic field control unit [12]

In [9], it was first noted that two-frequency methods (2M-NQR) based on NQR are equivalent to a two-dimensional frequency experiment of NMR. In this case, the off-diagonal signals of the two-dimensional spectrum, indicating the presence of magnetization transfer between different states, are equivalent to additional signals of the two-frequency quadrupole echo. The sensitivity of 2M experiments cannot exceed the sensitivity of 1M experiments, but the information content of a two-dimensional experiment is much higher (Fig. 1.12).

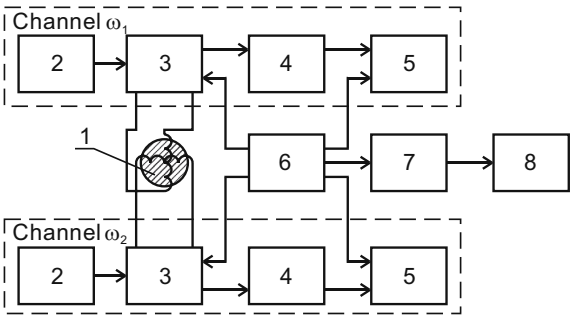

Fig. 1.12 The structure of a two-dimensional two-frequency NQR-spectrometer: 1 – receiving coils with a sample; 2 – RF generator; 3 – transmit and receive path; 4 – synchronous detector; 5 – ADC; 6 – pulse sequence programmer; 7 – interface; 8 – PC [10]

In recent years, a new important step has been made, which has led to the expansion of the scope of pulsed resonance research in the field of medicine [27]. It is about the possibility of visualizing the distribution of NMR parameters in the sample. In modern literature, this method is called magnetic resonance imaging [26, 28].

The modern stage of development of integrated circuit technology and the emergence of a new component base made it possible to develop compact radioelectronic devices, including portable spectrometers [29–31]. In [29], the development of a single board NMR spectrometer based on a digital receive path is presented. An embodiment of a sensitive NQR signal detector is described in [30]. In [31], the authors present a block diagram and experimental tests of an NQR spectrometer with small weight and size parameters. The use of field-programmable gate arrays (FPGA) allows one to implement algorithms for processing information transformations (generation of reference frequencies, accumulation and averaging of microwave signals, Fourier transform with a view to visualize NQR spectra) in a single-chip version [32, 33]. The introduction of special multipulse techniques into radiospectroscopic studies [34] deserves no less attention.

The development of experimental means of relaxation and pulse-resonance spectroscopy on the basis of modified Hahn, Carr-Purcell-Meyboom-Hill sequences and the modern component basis will bring the NQR experiments to a new higher level. The latter will provide the creation and updating of methods: increasing the accuracy of temperature measurement using NQR in layered semiconductors; measurement of weak magnetic fields using the Zeeman effect in layered crystals; the establishment of the quality of materials after growth and annealing.

1.4 The methods of computer parameteric identification of the NMR and NQR spectra

The analysis of literature data enabled us to identify several available programs that can be used to simulate the shapes of the NQR lines associated with quadrupole interactions of nuclei in powder solids. Typically, they are divided into two classes.

The modeling programs of the first class use in their analysis a density matrix. Examples of such programs include GAMMA, SIMPSON and SPINEVOLUTION, which are mainly used to calculate data in the time interval and to simulate sequences of excitation pulses. The simulation time of a specific experiment or spectrum using these programs may take from a few minutes to several days. These software products can also be used to simulate a magnetic spin angle (MSA) NMR, to test different sequences of excitation pulses, or to simulate multidimensional experiments with NMR.

The second class of modeling programs uses simple mathematical expressions to

directly calculate the resonant frequencies, which significantly reduces the simulation time. Examples of such programs are WSOLIDS, DMFit and QuadFit. The latter specializes in modeling the NMR spectra with distributed parameters, which is useful when analyzing amorphous solids. To efficiently generate simulation spectrums, all these programs use formulas derived from second-order perturbation theory to calculate the effect of quadrupole interaction on Zeemanian energy levels.

Currently, with the rapid growth of computer processing power, the calculations of the NMR spectra for small spin systems can be performed using diagonalization methods (i.e. "precise" methods). Thus, second-order perturbation theory is no longer the only convenient analysis instrument.

With the ever increasing complexity of NMR methods and software, numerous simulations have become an integral part of modern research. Usually, they are necessary for obtaining structural parameters from data, the development of new experiments and theoretical studies. This particularly refers to continuous NMR, where most programs use the magic-angle spinning (MAS) and ^{1}H-splitting to obtain high-resolution spectrums, while various methods of chemical shift anisotropy (CSA) are used to reconstruct the averaged interactions of dipole and chemical anisotropy [35]. These methods usually generate a homogeneous Hamiltonian, which depends on time and requires the use of numerical methods every time, when experiments need to be accurately simulated [36]. As a rule, such experiments have been developed and interpreted from the point of view of the first several orders of the average Hamiltonian theory (AHT), which can often be used to obtain approximate solutions [35].

However, although AHT is a fairly powerful analytical apparatus, it is not always possible to apply it because of its insufficient accuracy. In continuous NMR, analytical descriptions of experiments occur more frequently. However, numerical simulation in many cases does not lose its importance, for example, when studying non-ideal pulses, various effects generated by a strong coupling and relaxation, as well as in single-scan 2D-experiments [35].

Guided by the requirements of experimental NMR, in the past four decades, many computer programs for modeling NMR experiments have been developed [35]. Most of this software can be easily attributed to one of the following categories: NMR analytical tools (usually implemented in Mathematica), specialized applications (for example, NOESY spectrum simulator), application programming interfaces (APIs), generic NMR modeling programs. The last ones are called generic, since they can be used to simulate experiments with a wide spectrum of pulse sequences and spin systems, and therefore have the function of a virtual NMR-spectrometer. In addition, unlike the API, the modeling program must have a convenient high-level interface.

Despite all the advantages, only a few types of software available so far are suit-

able for modeling general experiments with NMR. As a result, several years ago, the development of new methods, in particular in solid state NMR, was often combined with the development of new problem-oriented software.

The analysis of the literature shows that ANTIOPE was the first common software for simulating NMR. The program is still supported and distributed by its author (J.S. Waugh). It has recently acquired a particularly user-friendly interface and experienced other significant changes since the release of the first version. The API-type package GAMMA, which appeared shortly after ANTIOPE, developed as a library of C ++ classes and methods, intended for the development of simulation applications [36]. Despite the fact, that GAMMA greatly facilitates the development of software for modeling, a significant number of tools are often required. The package has been widely used for many years to simulate NMR and EPR experiments. A similar API (BlochLib) has been developed recently, which uses efficient numerical libraries for its basic computations and is superior to GAMMA in terms of efficiency [35]. Currently the most popular in the solid-state NMR simulation package is SIMPSON [35]. It is designed as a high-level API, where modeling is guided by an input file written in a scripting language. SIMPSON does not require compilation and cumbersome software codes to perform simulations. The main application of this tool is the simulation of MAS experiments. Overall, this provides a trade-off between efficiency, convenience and versatility.

The above-mentioned three qualities are the most important characteristics, which are required by the general NMR / NQR simulation program. Versatility is achieved by using the approaches of GAMMA, BlochLib and, to a lesser extent, SIMPSON.

However, an interface that requires writing C ++ code for a complex API platform is unlikely to be convenient in most cases. In addition, for the effective propagation of the density matrix using the complex MAS experiment with multiple pulse sequences, it is necessary to calculate and process a complex collection of propagators. GAMMA, BlochLib and SIMPSON have limitations in such features. Moreover, the effectiveness of any simulation depends on the efficiency of computational methods and algorithms on which the modeling package relies, and is independent of the user. If these methods include only enough basic set of algorithms, creating a simple interface for such a package is relatively easy. However, if these methods include a large library of highly efficient and often specific algorithms, then their integration into a unified general NMR simulation program with a user-friendly interface presents a significant problem, which is added to the problem of developing methods themselves and creating libraries.

In an attempt to solve this problem, the SPINEVOLUTION tool was developed – a general NMR modeling program that implements a number of new calculation

methods and methodological approaches to it. Despite the fact that SPINEVOLUTION was developed specifically for modeling solid-state MAS experiments, it can also be used in the context of NMR-spectroscopy, in particular, for solving various optimization problems. The program has a convenient interface based on text files, where the pulse sequences are determined in the natural non-algorithmic form of the description of NMR experiments.

Computational methods and algorithms, which are largely responsible for the high performance of multi-spin calculations in SPINEVOLUTION, are based on Chebyshev decomposition to calculate propagators, thus, are able to use Hamiltonian diagonalizations. Another g-COMPUTE method, which generalizes the previously known COMPUTE and c-COMPUTE algorithms, combines efficient expansion of spectral lines with powder averaging. This makes it possible to use the c-COMPUTE algorithm for multivariate experiments of unlimited spectrum width. SPINEVOLUTION version 4.3 is compatible with most operating systems (Windows, Mac OS, Linux) [37].

In an NMR experiment, each data point is obtained by observing the magnetization of the sample after it undergoes a certain sequence of RF excitation pulses. In real experiments, a pulse program is used to set up the spectrometer to generate such sequences. In modeling, usually write a program which algorithmically describes which propagators should be calculated, and how they should be manipulated in order to specify the necessary sequence of pulses (as for example in GAMMA and SIMPSON).

SPINEVOLUTION is designed as an application and not as an API, so the user does not need to program. This is partially achieved using the classical approach to represent a sequence of pulses. Such a methodology provides a sufficiently simple interface and almost unlimited internal flexibility for analyzing the problem, organizing data and choosing calculation algorithms in the most efficient way. The user can choose the most convenient description of the sequence of pulses, can indicate the need to calculate powder averaging and relaxation processes. These parameters affect the efficiency and accuracy of the simulation. The interface provides the ability to perform a thorough check of the obtained data for compliance, facilitates the detection of configuration errors and significantly increases the convenience and reliability of the program [35].

The program enters the main input text file, which is edited by the user according to a template. It can be either autonomous or refer to other files describing the details of the simulation. Thus, the same pulse sequences and parameter files can be used to create new models. The interface is also well suited for use with an external system shell (Pearl, MATLAB, etc.).

Spectral modeling is an effective means to optimize data collection sequences.

The VeSPA package (Versatile Simulation, Pulses and Analysis Package) is an integrated set of open source applications in Python, which allows users to perform the following manipulations: synthesize RF pulses, study scenarios collection MRS data using multiparameter spectral modeling and rising the efficiency of analyzing MRS data from GE and Siemens scanners [38].

Programs in VeSPA are integrated using a SQLite database (standard in the Python distributive), which allows you to exchange objects and results of MR-data. Programs are built on the basis of adaptation and expansion of three programs: MatPulse, GAVA and SITools, respectively [35, 36]. The modeling is based on the GAMMA modeling library (Fig. 1.13) [36]. VeSPA integrated this resource using SWIG to make it possible to obtain the necessary data directly in Python, without the need to attract external resources [35]. Examples of the VeSPA package interface are shown in Fig. 1.14 – Fig. 1.16.

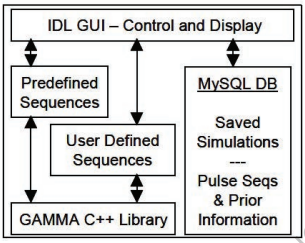

Fig. 1.13 Functional diagram of the GAVA environment, implemented on the basis of the SQLite database and the GAMMA library

The interactive graphical interface of VeSPA enables simultaneously working with data in several separate windows. The most important parameters of the configuration of the excitation pulses and the setting of important functions for the synthesis and analysis of resonance spectrums are combined into the following groups:

RFPulse – pulse concatenation, scaling, inversion of poles and export to graphic and special formats of the manufacturer;

Simulation – a graphical interface for simulating the excitation by a sequence of pulses, full dialog boxes for managing the database, outputting to the manufacturer's graphic and data formats (LC Model, Siemens Metabolite Report);

Analysis – HLSVD signal analysis, control deconvolution.

The fit of the least-squares baseline of the metabolite is repeated with an estimate of the wavelet baseline.

In all applications, the results can be shared between VeSPA users through XML import and export. The pulses specified in RFPulse can be used to form excitation sequences in Simulation, and the simulation results can be used to analyze spectral lines or selection of metabolites. The results obtained in VeSPA applications are accessed through browsers of MR results objects from the SQLite database. The databases also include integrated, predefined spectral modeling algorithms, designing RF excitation pulses and determining the optimal pulse sequences.

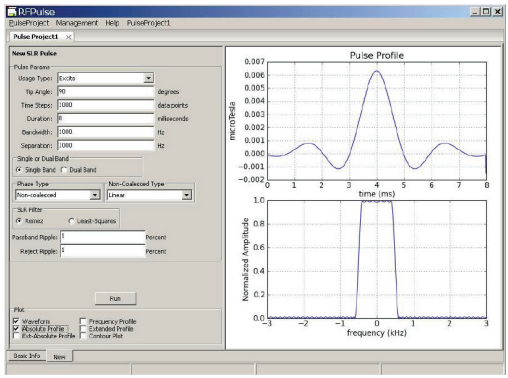

Fig. 1.14 Setting the parameters of the RF excitation pulse in the application RFPulse (VeSPA)

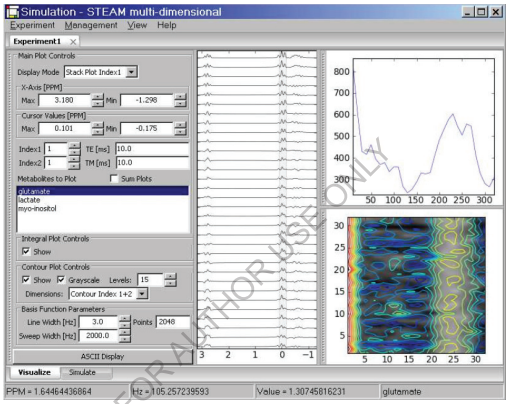

Fig. 1.15 Stack diagrams, integral diagrams of peaks and contour diagrams of peak areas with with a matrix of values 32 × 32 and three metabolites in the appendix Simulation – STEAM multi-dimensional (VeSPA)

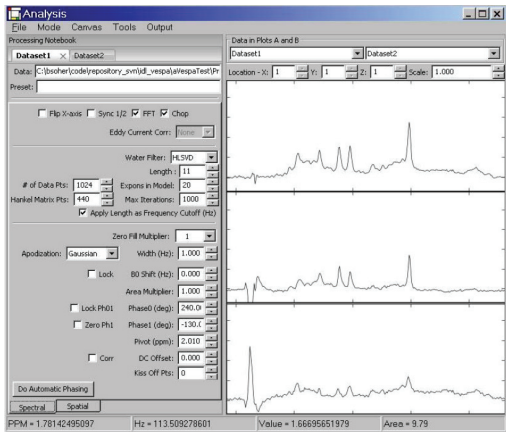

Fig. 1.16 The data set on one voxel PRESS – short TE, long TE and their difference (upper, middle, lower) in the application Analysis (VeSPA)

Unfortunately, it is difficult to find fast and at the same time convenient software for modeling with satisfactory accuracy of NMR / NQR spectra in open access [39]. From the review, it was found that one of the most accurate is the program for modeling quadrupole cores of powder samples under static conditions – Quadrupolar Exact SofTware (QUEST).

In particular, QUEST is designed to simulate accurate NMR / NQR spectra using the fast diagonalization procedure in the GNU Scientific Library, as well as an effective Aderman, Solum, and Grant (OSG) powder averaging scheme. Thus, diagonalization and NMR calculations are performed for a large number of crystal orientations, after which linear interpolation is performed in accordance with the ASG procedure to complete averaging of the powder. The GUI contains a central graph of the resonance spectrum with the ability to configure the above-indicated parameters.

As a rule, for quadrupole nucleus, the main interactions that affect the resonance spectrum are quadrupole interaction and magnetic shielding. These interactions include quantities that can be represented as second-rank tensors ("tensors"), which are especially convenient for representing NQR interactions in three-dimensional space [39].

The quadrupole interaction occurs due to the interaction of the electric quadrupole moment of the nucleus (Q) with the electric field gradient (EFG) on the nucleus. The tensor EFG is symmetric and has three components: $|V_{33}| \geq |V_{22}| \geq |V_{11}|$.

Since the EFG satisfies the Laplace equation (i.e. $V_{11} + V_{22} + V_{33} = 0$), the value of the quadrupole interaction can be represented by two parameters: the quadrupole coupling constants (C_Q) and the quadrupole asymmetry parameter (η). In QUEST, these parameters are defined as follows:

$$C_Q = \frac{eV_{33}Q}{\eta},$$

$$\eta = \frac{V_{11} - V_{22}}{V_{33}},$$

where C_Q – measure of quadrupole interaction, and η – the asymmetry parameter of the EFG tensor (within from 0 to 1), what determines the asymmetry of the EFG tensor (for $\eta = 0$, a symmetric tensor).

In QUEST, the C_Q and η values are indicated above the spectrum, which can be simulated by changing the mentioned data (Fig. 1.17a). In QUEST, the chemical shift tensor can be used as the EFG tensor, which is represented using the three main components (δ_{ii}) in the sequence: $\delta_{11} \geq \delta_{22} \geq \delta_{33}$. For setting the chemical shift tensor, three corresponding parameters are used – isotropic chemical shift δ_{iso}, interval Ω and offset K (Fig. 1.17b), determined by the formulas [39]:

$$\delta_{iso} = \frac{\delta_{11} + \delta_{22} + \delta_{33}}{3},$$

$$\Omega \cong \delta_{11} - \delta_{33},$$

$$K = \frac{3(\delta_{22} - \delta_{iso})}{\Omega}.$$

The relative orientation of the systems of the main axis of two tensor values mentioned above also affects the resonance frequency [39]. A common way to determine the relative orientation between different coordinate systems is to use Euler angles. In QUEST, the "ZYZ" system is adopted, where the chemical shift tensor is positioned in the direction of the EFG tensor (δ_{ii} along V_{ii}), and then turned off this EFG reference system. First, the chemical shift tensor rotates around δ_{11} at the Euler angle α, the next turn occurs around new orientation δ_{22} at the Euler angle β and, finally, the new orientation δ_{33} according to the Euler angle γ takes place. The location of these parameters in the QUEST interface is shown in Fig. 1.17. This process can be represented by rotating the magnetic field at a distance from the chemical shift tensor along the rotation matrix. The orientation of the constant magnetic field to calculate the EFG in this case is preserved:

$$R(\alpha,\beta,\gamma) = \begin{bmatrix} \cos\alpha\cos\beta\cos\gamma - \sin\alpha\sin\gamma & \sin\alpha\cos\beta\cos\gamma + \cos\alpha\sin\gamma & -\sin\beta\cos\gamma \\ -\cos\alpha\cos\beta\sin\gamma - \sin\alpha\cos\gamma & -\sin\alpha\cos\beta\sin\gamma + \cos\alpha\cos\gamma & \sin\beta\sin\gamma \\ \cos\alpha\sin\beta & \sin\alpha\sin\beta & \cos\beta \end{bmatrix}.$$

The relative orientation of two systems of the main axis is shown in Fig. 1.18.

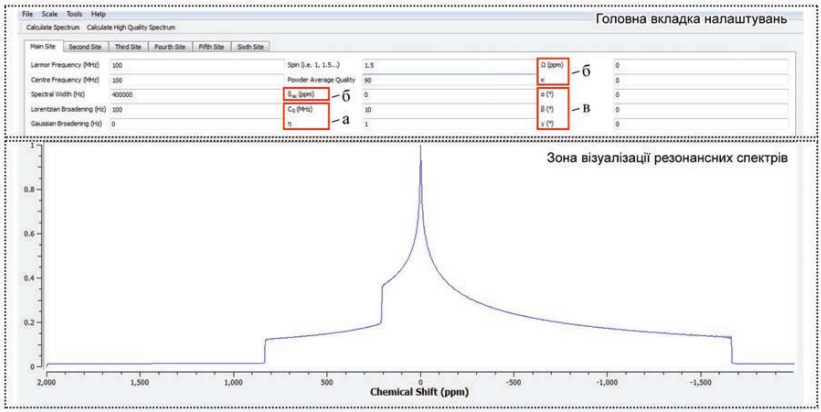

Fig. 1.17 Graphic interface of the QUEST software environment: C_Q and η (a) parameters, δ_{iso}, Ω and K (b) parameters; parameters α, β and γ (c) [39]

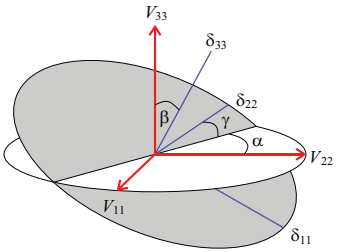

Fig. 1.18 Representation of the Euler angles defined in QUEST [39]

A special feature of QUEST is the way of quadrangular interaction processing. QUEST uses the complete quadrupole Hamiltonian, which can be expressed [39]:

$$\hat{H}_Q = \frac{C_Q}{4I(2I-1)}\left[\begin{array}{c}\frac{1}{3}\sqrt{6}(3\hat{I}_z^2 - I(I+1))V_0 + (\hat{I}_z\hat{I}_+ + \hat{I}_+\hat{I}_z)V_{-1} \\ -(\hat{I}_z\hat{I}_- + \hat{I}_-\hat{I}_z)V_{+1} + \hat{I}_+^2 V_{-2} + \hat{I}_-^2 V_{+2}\end{array}\right],$$

where the spherical tensor components are expressed as [39]:

$$V_0 = 3\sqrt{1/6}V_{zz}$$
$$V_{+1} = -V_{xz} - iV_{yz}$$
$$V_{-1} = V_{xz} - iV_{yz}$$
$$V_2 = \frac{1}{2}\left(V_{xx} - V_{yy}\right) + iV_{xy}$$
$$V_{-2} = \frac{1}{2}\left(V_{xx} - V_{yy}\right) - iV_{xy},$$

and the orientation dependence of the quadrupole Hamiltonian is calculated using the expressions [39]:

$$V_{xx} = \frac{1}{2}\left(3\sin^2\theta - 1 - \eta\cos^2\theta\cos 2\phi\right)$$
$$V_{yy} = \frac{1}{2}\left(-1 + \eta\cos 2\phi\right)$$
$$V_{zz} = \frac{1}{2}\left(3\cos^2\theta - 1 - \sin^2\theta\cos 2\phi\right)$$
$$V_{xy} = V_{yx} = \frac{1}{2}\eta\cos\theta\sin 2\phi$$
$$V_{xz} = V_{zx} = -\frac{1}{2}\sin\theta\cos\theta\left(3 + \eta\cos 2\phi\right)$$
$$V_{yz} = V_{zy} = \frac{1}{2}\eta\sin\theta\sin 2\phi.$$

It is much more convenient to represent the Hamiltonian in the matrix form, where all the matrix elements can be calculated analytically using the expectation values of various operators in the quadrupole Hamiltonian. The expressions given below include the influence of a magnetic field and chemical shift [39]

$$\left\langle m\left|\hat{H}_{ZQ}\right|m\right\rangle = -\nu_0\left(1+\delta_{ZZ}\right)+\frac{\sqrt{6}C_Q}{12I\left(2I-1\right)}\left(3m^2-I\left(I+1\right)\right)V_0$$

$$\left\langle m\pm1\left|\hat{H}_{ZQ}\right|m\right\rangle = \frac{\pm C_Q}{4I\left(2I-1\right)}\left(\left(2m\pm1\right)\sqrt{I\left(I+1\right)-m\left(m\pm1\right)}\right)V_{\mp1}$$

$$\left\langle m\pm2\left|\hat{H}_{ZQ}\right|m\right\rangle =$$

$$=\frac{C_Q}{4I\left(2I-1\right)}\left(\sqrt{I\left(I+1\right)-m\left(m\pm2\right)}\sqrt{I\left(I+1\right)-m\left(m\pm1\right)}\right)V_{\mp2}$$

$$\left\langle m\pm3\left|\hat{H}_{ZQ}\right|m\right\rangle = 0.$$

The above expressions show, that the Zeeman states (m = 3/2, 1/2 ...) are not real eigenstates of this Hamiltonian, since there are non-zero behind-diagonal elements. For this reason, the approximation of a high field, under certain circumstances, appeared to fiail. The Hamiltonian matrix should not contain off-diagonal elements, therefore QUEST diagonalizes this matrix, and its eigenvalues (which are energy levels) are used directly to calculate the resonance frequencies of all transitions with non-zero transition probability (this model also well describes overtones and NQR transitions). To calculate the intensities eigenvectors are used, and real nuclear eigenfunctions are expressed as [39]:

$$\left|n\right\rangle = \sum_{m=-I}^{I} a_{mn}\left|m\right\rangle ,$$

where the coefficient a_{mn} corresponds to the m-th component of the n-th eigenvector.

Proceeding from this, one can easily calculate the intensity of the lines of the NQR spectrum (the square of the magnitude of the expected value of the operator I_x in the case of a coil located perpendicular to the direction of the magnetic field).

The maximum intensity value will correspond to the case of the coil oriented perpendicularly to the direction of the external field. However, when using the MAS probe slight deviations are possible, since in this case the spectrometer coil is oriented at an angle of 54,74 °, and not at 90 °. Therefore, when studying nuclei with spin -1 on the Tools tab an additional parameter was added to change the angle of inclination. Potentially, this can be very useful in modeling the NMR spectra of over-

tones. The effect of changing the angle of the coil is carried out by adding a certain fraction of the operator IZ.

A secular approximation was used to calculate the effect of the chemical shift tensor (provided, that change of the eigenstates is only facilitated by the chemical shift tensor component, aligned with the applied field) [39]:

$$\delta_{zz} = \delta_{11}\sin^2\vartheta\cos^2\varphi + \delta_{22}\sin^2\vartheta\sin^2\varphi + \delta_{33}\cos^2\vartheta.$$

The increase in the processing speed of spectrum in QUEST is achieved due to the optimized implementation of the Alderman, Solum, and Grant spatial mosaic algorithm [39]. According to this algorithm powder averaging is performed for an ensemble of points above the pyramid instead of a hemisphere. This pyramid is divided into many triangles (each of which is a crystalline orientation), where the resonance frequency is calculated at each vertex of the triangle. The resonance frequency for the remain of the space can be interpolated based on these three frequencies. Such an approach provides two advantages: cosines and sines do not need to be calculated, since they can be approximated using simple expressions, and secondly, fewer crystal orientations can be used, since the remain of the space can be interpolated.

Calculations of powder averaging in QUEST are performed at the vertices of each triangle, and the space between them is interpolated. For example, Fig. 1.19 corresponds to the average quality of the powder 6 [39].

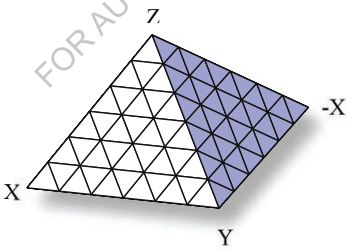

Fig. 1.19 Schematic representation of space in QUEST

Unless the CSA is taken into account, it is only necessary to perform averaging over one edge of this pyramid, which significantly reduces the calculation time. If we take into account the CSA and, if the tensors do not coincide, it will be necessary to perform powder averaging over all four edges of the pyramid. The factor limiting the time of performing the calculation in QUEST, appears to be the calculation of not only one resonance frequency, but all frequencies that determine the resonance spectrum. At the beginning of the calculations two indicators of these actions will appear: the first shows the actual NMR calculation, while the second shows the binnig of all frequencies (data addition from the next N pixels of the matrix takes place,

while increasing the sensitivity in N times, the spatial resolution experiences the N time drop).

Algorithm spreading lines of the spectrum in QUEST is based on Lorentz and Gauss convolutions. They are calculated by distributing the signal intensity of a single histogram cell into all cells [39]:

$$I_L = \frac{I}{1 + \frac{4\left(v - v_0\right)^2}{L_B^2}},$$

$$I_G = I \exp\left[\frac{-4\ln(2)\left(v - v_0\right)^2}{G_B^2}\right],$$

where I_L – Lorenz line intensity at a given frequency v; I_G – Gauss line intensity at a given frequency v; v_0 – resonance frequency for peak intensity I; L_B – the magnitude of the expansion of the line Lorenz; G_B – the magnitude of the expansion of the line Gauss.

QUEST is able to read spectral files of the standard Bruker format (i.e. TOPSPIN) [39]. To be more specific, QUEST reads only * .1r and * .procs files. In order to open the spectrum, it's necessary to open the folder containing the spectrum and select the *.1r file; the *.procs file automatically finds the QUEST software if it is in the same directory. The *.1r file contains a series of binary integer numbers representing the signal intensity, whereas the * .procs file contains all other necessary information (transmitter frequency, width of the spectrum, number of data points, etc.).

The QUEST software enables calculating all resonance transitions, and therefore the spectral window is set manually when necessary. This can be done by adjusting the parameters of central frequency and spectral width. The size of the spectral width also affects the calculation time.

For nucleus with significant quadrupole interactions and possessing several NMR-active isotopes with similar gyromagnetic ratios, such as bromo-79/81 or rhenium-185/187, different layers of powder for different isotopes can overlap. This entangles the modeling of spectrum, because chemical shifts are related to only one isotope. To eliminate this effect, one can change the reference frequency, which is used to calculate the chemical shifts. This function should be used while maintaining the NMR spectrum of one isotope that was experimentally associated with another isotope. Alternatively, if the experimental spectrum is loaded, there is also an additional option to set the reference frequency.

By default, the experimental and calculated spectrums are normalized to an intensity equal to unity. If there are obvious differences in the experimental spectrum,

this can greatly reduce the intensity of the wider spectrum elements, which have a practical interest in the experimental spectrum. Thus, it is necessary to increase the scale of the experimental spectrum. In addition, it is possible to save or read the parameters used to create the QUEST simulation spectrum with the "Save" or "Read" option of the QUEST parameter files on the File menu tab. The parameter files in QUEST are the text files containing information about the Larmor frequency, center frequency, L_B, G_B, δ_{iso}, average powder quality, sample rotation angle, spectrum width, C_Q, α, β, γ, η, Ω and κ in sequential order.

Examples of simulation of resonance spectrums with the use of the QUEST software environment are shown in Fig. 1.20 – Fig. 1.22. QUEST allows one to simulate up to six objects. To configure the parameters of other objects it is necessary to select the new tabs. Additional settings (chemical shift and parameters of the EFG tensor, rotation angle, Larmor frequency and relative intensity) are available for the first object. If the relative intensity is set to "0", then no other calculations are performed. By default, the main position has a relative intensity of 100 %. An example of modifying several positions using the QUEST software is shown in Fig. 1.20.

The tab "Tools" menu contains options that facilitate the operation with several objects, in particular for some elements, such as bromine or rhenium, there are various isotopes with similar NMR parameters. In these cases, if the quadrupole interaction is noticeable, both isotopes can be observed in the same window. For this reason, it is possible to combine several objects thus, the selected parameters for the second object are automatically calculated based on the corresponding parameters of the first one. Chlorine, titanium, copper, bromine, indium and rhenium are added to the spin pairs. On the tab "Tools" of the menu there is a possibility to "disconnect" objects that were connected to each other, or remove the experimental spectrum.

During modeling of the NQR spectrums, it is necessary to use a small Larmor frequency (~ 0,0001 MHz), but not equal to 0. This is due to the fact that the pure NQR peaks are infinitely sharp and, therefore, difficult to add if they appear between the bins on the histogram. Since the calculations in QUEST are performed in terms of the absolute frequency, while using a very narrow spectral window, there may be a lack of the necessary accuracy in the frequency values of each bin in the histogram. In addition, when the spectrum is stored in the Bruker TOPSPIN format, information on the chemical shift, not on the resonance frequency is used. Thus, the spectrums can be saved only if they are calculated in the chemical shift mode, and not in the resonance frequency mode. QUEST uses several C/C++ libraries for research. The function "gsl_eigen_hermv" from the GNU Scientific Library was used to diagonalize the effective Zeemani-quadrupole Hamiltonian matrix [41]. This is a free C library developed for scientists that provides an optimized diagonalization procedure and hundreds of other procedures.

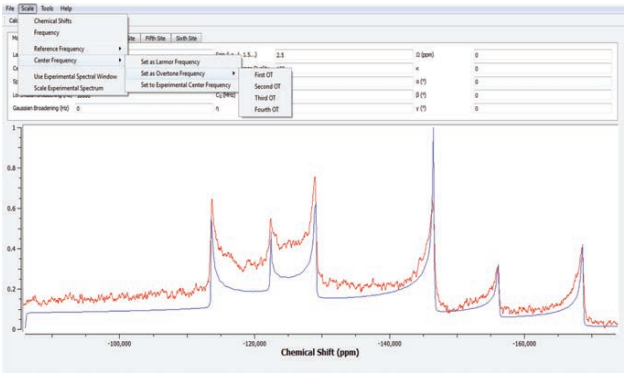

Fig. 1.20 QUEST graphical user interface, which demonstrates the $^{185/187}$Re NMR spectrum simulation and its comparison with the experimental spectrum obtained at 11,7 T [40]

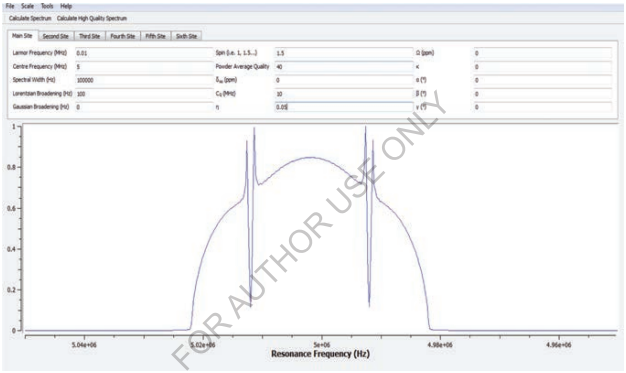

Fig. 1.21 Simulation of the Zeeman effect in the NQR for a nucleus with spin 3/2. The asymmetry parameter can be determined from the positions of the dips [41, 42]

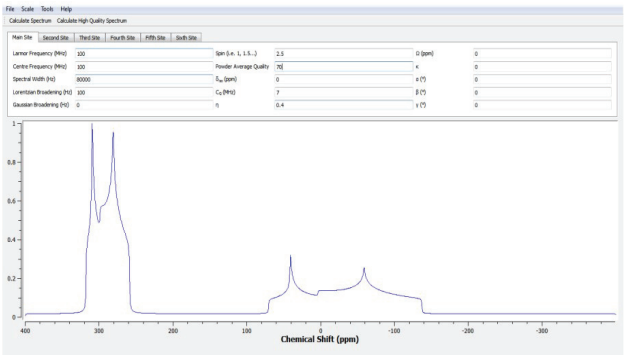

Fig. 1.22 QUEST graphical user interface that shows a simulation of several positions for a spin pair $^{47/49}$Ti [39, 41]

It is also possible to change the coil angle for all spins, for example, this enables simulating the Zeeman NQR perturbation spectrum of spin 3/2 nucleus, where the coil angle is usually parallel to the magnetic field (Fig. 1.21) [41, 42].

As it is already mentioned, the QUEST spectral modeling is based on summation in the complete quadrupole Hamiltonian. This theory is valid and holds for all transitions and with an arbitrary position of the magnetic field. Fig. 1.23 shows the particular case of a nucleus with spin 3/2 with a C_Q of 10 MHz and an axially symmetric gap ($\eta = 0$) when the Larmor frequency is changed.

Below in Fig. 1.23 ($\nu_0 = 100$ MHz) a typical NMR spectrum is observed for a nucleus with spin 3/2 with an intense central transition (from 1/2 to -1/2) in the center, which is not affected by the first-order quadrupole interaction. The interval between two adjacent transitions (from 3/2 to 1/2 and from -1/2 to -3/2), which are much wider and largely invariant depending on the magnetic field, shrinks in NMR mode. On the other hand, the width of the central transition increases sharply with decreasing magnetic field. When the value of ν_Q is equivalent to the value of ν_0 (5 MHz) the spectrum starts losing features, typical of quadrupole-perturbed NMR spectrums (for example, there is no "step" observed in the central transition). When $\nu_0 = 2$ MHz, three overtone transitions (from 3/2 to -1/2, from 1/2 to -3/2 and from 3/2 to -3/2) appear in the spectrum and overlap with "allowed" NMR-transitions. Further, when $\nu_0 = 0$ MHz, they are combined with NMR transitions to form the "allowed" NQR transition (from ±1/2 to ±3/2). This type of analysis together with the analysis of magnetic resonance frequencies, carried out by Bane and Hasavna [39] is crucial for understanding both NQR and NMR.

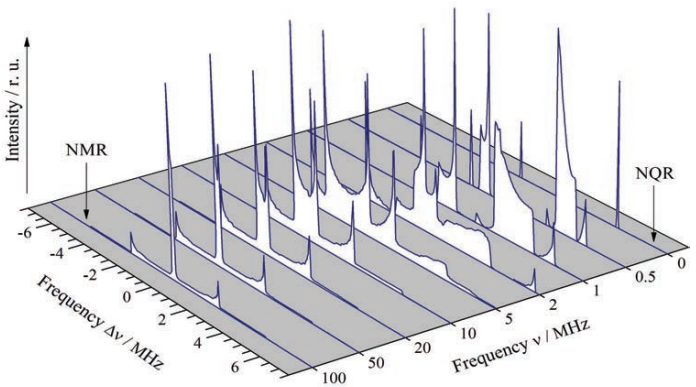

Fig. 1.23 Spectral modeling in QUEST nucleus with a spin of 3/2 with an axially symmetric EFG tensor and $C_Q = 10$ MHz with increasing Larmor frequency from 0 to 100 MHz. There is a progression from NQR in high field NMR. Simulation with ν_0 from 5 MHz corresponds to $\nu_0 = \nu_Q$.

1.5 Conclusions

In pulsed equipment designed to search for quadrupole resonance signals, it is necessary to maintain constant phase relationships between the signals of the spin system and the reference signal at any frequency of the spectrometer operating range. In coherent type spectrometers, synchronous signal detection can be used, and the reference signal is fed directly to the input of the receiving device. In this case, the main source of phase distortion is the transmit path. To minimize phase distortions, it is necessary to reduce the number of cascades in this path and make them broadband.

The method of double nuclear quadrupole resonance in a weak magnetic field is used if the sensitivity of direct methods is insufficient. Due to the fact that in the double resonance method with cross-relaxation, expansion of the resonance lines due to the presence of a magnetic field is observed, its application to the study of multiplet broadband spectra is practically impossible.

Dual-frequency methods of nuclear quadrupole resonance provide a significant increase in the information content of the resonance spectra and a good resolution, but the sensitivity of 2M experiments cannot exceed the sensitivity of 1M experiments under the same initial conditions.

A good resolution of the broadband spectrum can be obtained by using the method of direct pulse detection, so this method is of greatest interest in many practical applications. The absence of magnetic modulation coils and the use of a modern component base will reduce the cost and mass-dimensional performance of equipment.

As a result of the performed analysis it can be stated that there is no publicly available and user-friendly software that accurately describes the mathematical models of the Zeemanian quadrupole Hamiltonian and the chemical shift anisotropy. In NQR, the quadrupole interaction is dominant, and when conducting experiments on real samples with quadrupole nucleus, the intermediate region is uncertain, hence common practice using perturbation theory to analyze spectrums under certain circumstances may be unacceptable.

It is established that the Quadrupolar Exact SofTware is the most suitable for computer parametric identification of NMR and NQR spectrums. Such a choice is also justified when it is required to identify complex multiplet spectrums, thin structure of which is associated with a complex crystal structure, in particular, the presence of EFG $\eta \neq 0$. The latter confirms the possibility of effectively using QUEST to study all possible quadrupole Zeemanian interactions.

References

1. O. Z. Hotra, A. P. Samila, G. M. Rozorinov, O. V. Gres, Current status and development prospects of nuclear quadrupole resonance pulsed spectroscopy methods: A review, Telecommunications and Radio Engineering. 78 (2019) 1483–1496.
2. A. P. Samila, G. I. Lastivka, Yu. V. Tanasyuk, Actual problems of computer parametric identification of the NMR and NQR spectra: A review, J. Nano- Electron. Phys. 11 (2019) 05036-1–10.
3. Job, Constantin, Pearson, Robert M., Brown, Michael F., (1994) A personal computer-based nuclear magnetic resonance spectrometer, *Rev. Sci. Instrum*., 65(11), pp. 3354-3362.
4. Rudakov, T.N., Belyakov, A.V., Mikhaltsevich, V.T., (1997) A low-frequency instrument for remote nuclear quadrupole resonance experiments, *Meas. Sci. Technol*., 8, pp. 444-448.
5. Hiblot, Nicolas, Cordier, Benoit, Ferrari, Maude, Retournard, Alain, Grandclaude, Denis, Bedet, Jerome, Leclecrc, Sebastien, Canet, Daniel, (2008) A fully homemade 14N quadrupole resonance spectrometer, *C.R. Chimie*, 11, pp. 568-579.
6. Samila, A., Khandozhko, V., Politansky, L., (2017) Energy efficiency increase of NQR spectrometer transmitter at pulse resonance excitation with noise signals, *Solid State Nuclear Magnetic Resonance*, 87, pp. 10-17.
7. Gabidullin, D.D., Gafiyatullin, N.M., Krylatykh, N.A., Fattakhov, Ya.V., (2012) A precision frequency synthesizer with direct digital synthesis for a low field magnetic resonance imager, *Instruments and Experimental Techniques*, 55(4), pp. 462-464.
8. Fang, Yi-Yuan, Xue-Jun, Chen, (2012) Design of equal precision frequency meter based on FPGA, *Engineering*, 4, pp. 696-700.
9. Anferov, V.P., Grechiskin, V.S., Siniavsky, N.Ya., (1990) *Nuclear spin resonance. New methods*, Leningrad: State University Publ., p. 164 [in Russian].
10. Grechishkin, V.S., Siniavsky, N.Ya., (1993) Localnyi YKR v tverdykh telakh [Local NQR in solids], *Uspekhi Fizicheskikh Nauk - Physics Uspekhi*, 163(10), pp. 95-119 [in Russian].
11. Smith, J.A.S., (1995) Nitrogen-14 quadrupole resonance detection of RDX and HMX based explosives, *Proceedings of European Convention on Security and Detection*, pp. 288-292.
12. Grechiskin, V.S., Siniavsky, N.Ya., (1997) Novyie fizicheskiie tekhnologii: obnaruzheniie vzryvchatykh i narkoticheskikh veshchestv metodom yadernogo kvadrupolnogo resonansa [New physical technologies: detection of explosive

and narcotic substances by nuclear quadrupole resonance method], *Uspekhi Fizicheskikh Nauk - Physics Uspekhi*, 167(4), pp. 413-427 [in Russian].
13. Apih T., Rameev B., Mozzhukhin G., Barras J. (2014) Magnetic resonance detection of explosives and illicit materials, *NATO Science for Peace and Security Series B: Physics and Biophysics*, Springer, p. 168.
14. Leche, A., (1963) *Yadernaia induktsiia [Nuclear induction]*, Moscow: Inostrannaya literatura, p. 684 [Russian transl].
15. Vlasova, M.V., Kakazei, N.G., (1979) *Elektronnyi paramagnitnyi resonans v mekhanicheski razrushennykh tverdykh telakh [Electronic paramagnetic resonance in mechanically destroyed solids]*, Kyiv: Naukova dumka, p. 200 [in Russian].
16. Vilkov, P.V., Pentin, Yu.A., (1989) *Fizicheskiie metody issledovaniia v khimii. Resonansnyie i elektroopticheskiie metody [Physical research methods in chemistry]*, Moscow: Vysshaya shkola, p. 288 [in Russian].
17. Grechishkin, V.S., (1959) Yadernyi kvadrupolnyi resonans [Nuclear quadruple resonance], *Uspekhi Fizicheskikh Nauk - Physics Uspekhi*, 14(2), pp. 189-216 [in Russian].
18. Skripov, F.I., (1964) *Kurs lektsii po radiospektroskopii [A course of lectures on radio spectroscopy]*, Leningrad: Leningrad State University Publ., p. 212 [in Russian].
19. Grechishkin, V.S., (1973) *Yadernyie kvadrupolnyie vzaimodeistviia v tverdykh telakh [Nuclear quadrupole interactions in solids]*, Moscow: Nauka, p. 263 [in Russian].
20. A. Samila, *Measurement* 106, 109 (2017).
21. A.P. Samila, V.O. Khandozhko, Z.D. Kovalyuk, *J. Nano- Electron. Phys*. 7 No3, 03024 (2015).
22. Farrar, T., Becker, E., (1973) *Impulsnaia i Fourier-spetroskopiia YMR [Pulsed and Fourier spectroscopy of NMR]*, Moscow: Mir, p. 164 [Russian transl.].
23. Harding, J.C., Wade, D.A., Marino, R.A., Sauer, E.G., Klainer, S.M., (1979) A pulsed NQR-FFT spectrometer for nitrogen-14, *Journal of Magnetic Resonance*, 36, pp. 21-33.
24. *Yadernyi magnitnyi resonans [Nuclear magnetic resonance]*, P.M., Borodin (Ed.), (1982) Leningrad: Leningrad State University Publ., p. 344 [in Russian].
25. Khandozhko, V.O., Politanskyi, L.F., Samila, A.P., (2013) Porivniannia rezultativ detektuvannia YKR metodamy neperervnoho ta impulsnoho sposterezhennia [Comparison of the results of detection of NQR by continuous and pulsed monitoring methods], *Visnyk Natsionalnoho Universytetu "Lvivska Polytechnika". Radioelektronika ta telekomunikatsii – Bulletin of National University "Lvivska Polytechnika"*, 766, pp. 35-40 [in Ukrainian].

26. Moskalev, A.K., (2007) *Radiospektroskopiia: kurs lektsii [Radiospectroscopy: a course of lectures]*, Krasnoyarsk: Siberian Federal University Publ., p. 127 [in Russian].
27. Vladimirov, Yu.A., Osipov, A.N., (2004) Nobelevskaia premiia v oblasti fiziologii i meditsyny za 2003 prisuzhdena P.Lauterburu i P.Mensfildu [The 2003 Nobel Prize in Physiology and Medicine was awarded to P.Lautebur and P.Mansfield], *Priroda – Nature*, 1, pp. 6-8 [in Russian].
28. Blumich, Bernhard, (2011) *Osnovy YMR [Fundamentals of NMR]*, Moscow: Technosphere, p. 256 [Russian transl].
29. Tang, Weinan and Wang, Weimin, (2011) A single-board NMR spectrometer based on a software defined radio architecture, *Measurement Science and Technology*, 22, pp. 015902/1-8.
30. Chytil, J. and Kubasek, R., (2014) Detector for nuclear quadrupole resonance spectroscopy, *Progress In Electromagnetics Research Symposium Proceedings*, 1, pp. 1907-1910.
31. Beguš, Samo, Jazbinšek, Vojko, Pirnat, Janez, Trontelj, Zvonko, (2014) A miniaturized NQR spectrometer for a multi-channel NQR-based detection device, *Journal of Magnetic Resonance*, 247, pp. 22-30.
32. Hotra, O., Samila, A., Politansky, L. (2018) Synthesis of the configuration structure of digital receiver of NQR radiospectrometer, *Przegląd Elektrotechniczny*, 94(7), pp. 58-61.
33. Samila, A.P., Rozorinov, G.M., Gres, O.V., (2018) Rozroblennia impulsnykh metodiv radiospektroskopii yadernoho kvadrupolnoho resonansu na osnovi prohramovanoi logichnoi intehralnoi skhemy [Development of pulsed methods of radiospectroscopy of nuclear quadrupole resonance based on programmable logic integral circuit], *Vcheni zapysky TNU imeni V.I.Vernadskoho. Seriia: tekhnichni nauky - Transactions of V.I.Vernadskyi National Technical University. Series: Engineering sciences*, 29(68), pp. 66-73 [in Ukrainian].
34. Bobalo, Yu., Hotra, Z., Hotra, O., Politans'kyy, L., Samila, A., (2015) Implementation of pulsed radiospectroscopy methods of NQR based on FPGA, *Metrol. Meas. Syst*., 22(3), pp. 363-370.
35. Mikhail Veshtort, Robert G. Griffin, *J. Magn. Reson.* 178, 248 (2006).
36. Z. Aygula, B.J. Soher, K. Young, A.A. Maudsley, *Proc. Intl. Soc. Mag. Reson. Med.* 11, 852 (2003).
37. Mikhail Veshtort, http://spinevolution.com/wp-content/uploads/SpinEvolution-Reference-Manual.pdf.
38. B.J. Soher, P. Semanchuk, D. Todd, J. Steinberg and K. Young, *Proc. Intl. Soc. Mag. Reson. Med.* 19, 1410 (2011).
39. Frederic A. Perras, Cory M. Widdifield, David L. Bryce, *Solid State Nucl.*

Magn. Reson. 45-46, 36 (2012).
40. C.M. Widdifield, A.D. Bain, and D.L. Bryce, *Phys. Chem. Chem. Phys.* 13, 12413 (2011).
41. Patrick M.J. Szell, David L. Bryce, https://onlinelibrary.wiley.com/doi/epdf/10.1002/cmr.a.21412.
42. A.P. Samila, G.I. Lastivka, V.O. Khandozhko, *J. Nano- Electron. Phys.* 8 No4, 04081 (2016).

Chapter 2
Models of the pulsed NQR method based on parametric transformations of free induction decay

2.1 NQR signal model theory

For computer simulation of signal transformations in pulsed NQR-spectrometer it is necessary to represent the expected response of nuclear system to a short δ-like excitation pulse. The majority of the existing models of NQR signals possess considerable analytical awkwardness which complicates their use in real-time simulation systems. The interaction between NQR-spectrometer coil and the sample within close to resonance frequencies is sometimes represented as an equivalent electric circuit which is not practical in the simulation of multiplet spectra in a broad frequency band [1, 2].

It is more efficient to represent resonance system response to RF excitation pulse as a pulse transient response which is a FID signal. NQR signal in the form of FID after the effect of a radio-frequency 90º-pulse for the resonance frequency ω is of the form [3]:

$$y(t) = Ae^{-[\beta+i\omega(T)]t} + n(t), \tag{2.1}$$

where A is general magnitude whose value is determined by the power of excitation signal; β is decay coefficient of signal that depends on the duration of relaxation processes inside spin system; $\omega(T)$ is NQR resonance frequency that depends on temperature T; $n(t)$ is noise component of FID signal.

The NQR spectrum is obtained after the Fourier conversion of FID signal represented by function (2.1).

With a pulsed method of investigation of NQR spectral characteristics, information on the dynamics of lattice and spins can be obtained from measuring relaxation times that result from interaction inside the spin system (this process is characterized by transverse relaxation time T_2) and with other degrees of freedom in the lattice (it is spin-lattice relaxation time T_1). After the effect of a 180º pulse nuclear spin rotation phases will reverse. As a result, after some time t_g from the beginning of the experiment, an echo-signal arises which decreases with time by the law $\exp(-t/T_2)$ [3]:

$$y^m(t) = A\sum_{k=1}^{d} K_k e^{-\eta_k(T)(t+m\cdot 2t_g)} e^{-\beta_k\left|t-m\cdot 2t_g+t_g\right|+i\omega_k(T)t} + n(t), \tag{2.2}$$

where K_k is scale factor for the amplitude of k-th component; $\eta_k(T)$ is decay coeffi-

cient of echo-signal which depends on the sample T_2; t_g is time interval between the first and second pulses; $2t_g$ is time interval after the second pulse. Formula (2.2) represents echo unit segment which is recorded at excitation of the sample by the m-th 180º-pulse.

Fig. 2.1 represents the result of simulation as a combination of FID and spin-echo signals with excitation of NQR by the pulse sequence of CPMG type [4].

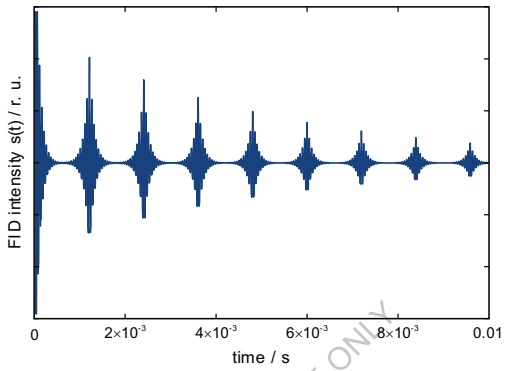

Fig. 2.1 Model of NQR signal that corresponds to sample excitation by the pulse sequence of CPMG type

To observe spin-echo in solids, it is necessary for $t_{pulse} < T_2$ condition to hold. Otherwise, the induction signal after the 1-st pulse will have no time to decay by the moment of echo signal appearance. When the latter is observed from different nuclei one has to change pulse durations, since the condition of a 90°-pulse is of the form (for $\eta = 0$)

$$\frac{\pi}{2} = \gamma H_1 t_{pulse} \sqrt{I(I+1) - m(m+1)}\,, \tag{2.3}$$

where I is nucleus spin, m is magnetic quantum number for the low energy level, t_{pulse} is duration of excitation pulse.

Selection of excitation pulse duration is caused by the properties of resonating nucleus. On switching field H_1 for a short period of time t_{pulse}, the quadrupole moment vector will turn by an angle of 90°. The NQR frequencies for the majority of isotopes of nuclei of solids with nonzero quadrupole moment (Cl, Cu, Ga, In and others) are in the range of 1 – 30 MHz. If $\gamma H_1 = \omega$, then proceeding from (2.3) for the observation of spin-echo in solids it is necessary to select $t_{pulse} \sim 1 - 4$ μsec, the amplitude of radio-frequency pulse H_1 reaching several kilovolts. The "dead" time of the receiver after the effect of high-power pulse on its input should not exceed 3–5 μs.

The concepts of construction of installations for spin echo observation in mag-

netic and quadrupole resonances are little different. As long as the NQR lines are broader than the NMR lines in liquids, to obtain nuclear system response and quadrupole spin echo with a satisfactory signal/noise ratio, it is necessary to form more high-power radio frequency pulses (1 kW and more). Resonance search is similar to the continuous wave method and is based on nucleus excitation by pulses filled with variable frequency [5, 6]. Moreover, to detect weak quadrupole echo-signals, one must have a receiver adjustable in a broad frequency band.

For simulation of signal transformations in a pulsed NQR spectrometer its simulation model was developed in MATLAB Simulink software (Fig. 2.2) [7]. The model comprising high-frequency transmitter, receive path and measuring unit is based on the concept of implementation of a single-coil coherent NQR radio spectrometer without carrier frequency conversion.

The source of carrier frequency ω_0 is a synthesizer (***1***) that generates sine vibrations in the range of 1 – 50 MHz. The latter are needed to fill probing pulses in the range of NQR resonance frequencies and to form reference voltage for the receiver's quadrature detector. A signal from the synthesizer arrives at high-speed switch (***3***) which forms probing pulses $\boldsymbol{\tau}_{exc}$ whose leading edges are coherent with carrier oscillation phase. Programmer (***2***) controls electronic switch assuring formation of pulse sequences with time ratios of formed video pulses according to prescribed algorithm [8].

Output amplifier (***6***) with amplification factor 50 dB is loaded on a coil with sample under study [9]. The latter form NQR-subsystem (***8***) of proposed simulation model.

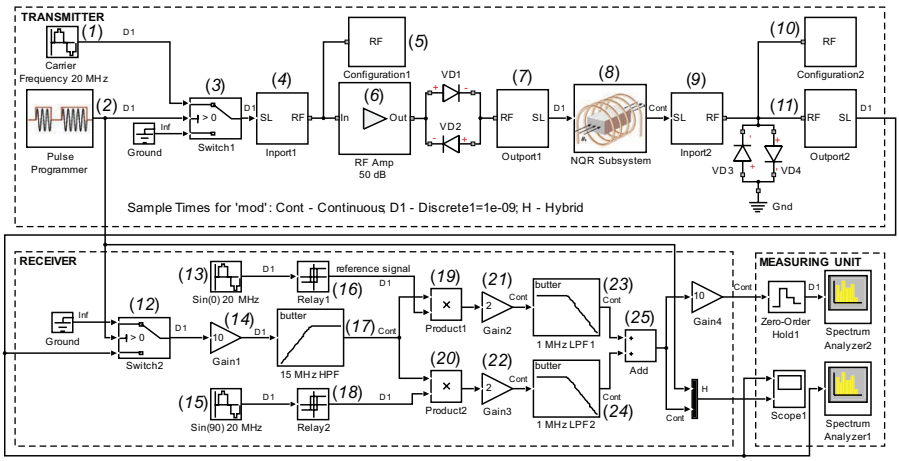

Fig. 2.2 Simulation model of pulsed NQR observation method implemented in MATLAB Simulink software

It is known that in a real device the level of noise grows with increase in the number of units. When constructing schemes with a large number of units, the largest contribution to total noise ratio is made by the first stage. This dependence is described by the Friis law. In the structure of pulsed spectrometer the first stage is considered to be the input circuit of the spectrometer, namely an oscillatory circuit with a sample under study. As long as we deal with virtual Simulink simulation, for the reduction of computational loads on computer a simplification was taken which consists in the fact that the source of noise is only unit (***8***) which simulates the input circuit of the spectrometer. There are no units for matching data types (***4***, ***7***, ***9***, ***11***) and configuration of RF parameters (***5***, ***10***) in a real experiment. However, simulation in Simulink without them is impossible.

In case of resonance excitation by a short single δ-pulse the response signal is a pulse transient function

$$s(t) = Ae^{-[\beta+i\omega(T)]t} + A\sum_{k=1}^{d} K_k e^{-\eta_k(T)(t+m\cdot 2t_g)} e^{-\beta_k\left|t-m\cdot 2t_g+t_g\right|+i\omega_k(T)t} + 2n(t) \qquad (2.4)$$

and NQR-subsystem (***8***) in the proposed simulation model can be represented by a generalized transmitting characteristic

$$H(p) = \frac{Y(p)}{X(p)}, \qquad (2.5)$$

where $X(p) = L\{x(t)\}$ and $Y(p) = L\{s(t)\}$ are the Laplace images of original NQR excitation signal and NQR response signal.

The NQR method is also often employed for investigation of samples characterized by complex multiplet spectra (for instance, indium or gallium monoselenides). In this case the model of NQR-subsystem must take into account the complexity of spectra representing response signal image as

$$Y(p) = Y_1(p) + Y_2(p) + ... + Y_n(p), \qquad (2.6)$$

then a transfer function of NQR -subsystem

$$W(p) = \sum_{i=1}^{n} H_i(p) = \frac{Y_1(p) + Y_2(p) + ... + Y_n(p)}{X(p)}. \qquad (2.7)$$

The simulation model of the NQR subsystem of the pulsed spectrometer corresponding to this mathematical model is depicted in Fig. 2.3. This figure depicts the *s*-model of the NQR subsystem of radio spectrometer in which the “Transfer Fcn0” unit simulates the response of the LC oscillating circuit, and the "Transfer Fcn1 - Transfer

Fcn12" units simulate the response of spin oscillating systems of the NQR multiplet spectrum (FID signal). The “Band-Limited White Noise” unit serves as a model of the source of noise signals.

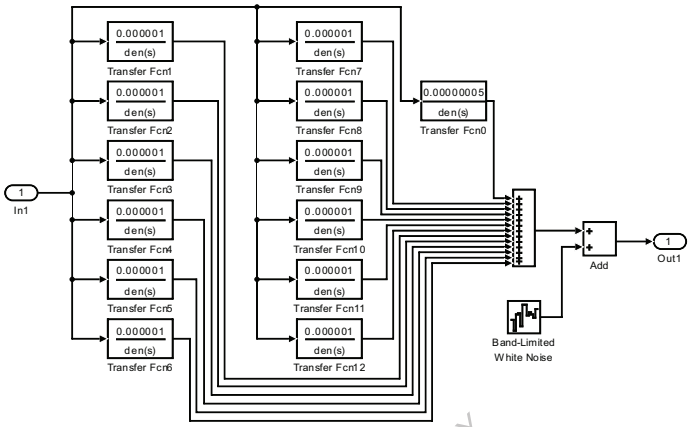

Fig. 2.3 The simulation model of the NQR subsystem of the pulsed spectrometer implemented in MATLAB Simulink software

Table 2.1 The parameters of the transfer functions of the oscillating links

Link	Gain k	Time constant T, s	Damping factor ξ
Transfer Fcn0	5e-8	7.9577e-9	3.1416e-5
Transfer Fcn1	1e-6	7.7758e-9	3.2151e-5
Transfer Fcn2	1e-6	7.7676e-9	3.2185e-5
Transfer Fcn3	1e-6	7.7492e-9	3.2261e-5
Transfer Fcn4	1e-6	7.7451e-9	3.2278e-5
Transfer Fcn5	1e-6	7.7411e-9	3.2295e-5
Transfer Fcn6	1e-6	7.7377e-9	3.2309e-5
Transfer Fcn7	1e-6	7.7337e-9	3.2326e-5
Transfer Fcn8	1e-6	7.7165e-9	3.2398e-5
Transfer Fcn9	1e-6	7.7125e-9	3.2415e-5
Transfer Fcn10	1e-6	7.7079e-9	3.2434e-5
Transfer Fcn11	1e-6	7.7034e-9	3.2453e-5
Transfer Fcn12	1e-6	7.6994e-9	3.2470e-5

NQR registration by pulsed methods brings about a problem of elimination of radio spectrometer receive path overloading in the process of probing pulse action and suppression of free oscillations on its termination.[16] The latter is due to excessive “ringing” of oscillating circuit and can essentially increase the “dead” area of

induction signal reception or even completely eliminate it reception and amplification. In this case we lose helpful information which is important at Fourier transform of spin induction signal to NQR resonance spectrum. Observation of NQR signals in the intervals between the pulses of radio frequency field allows avoiding many problems related to the presence of radio-frequency field. To eliminate overloading of receiver stages, limiting diodes with high switching speed are installed at the input thereof. The signal of nuclear spin induction arising in receiving coil arrives at electronic switch (***12***) which is practically realized as a gating amplifier. The latter shunts the receiver input for some time $\tau_{str.} = \tau_{exc.} + \tau_{trans.}$, where τ_{trans} is additional time. The excess $\tau_{str.} > \tau_{exc}$ is determined by the duration of transient process in receiving coil with the sample after the effect of τ_{exc} and is established experimentally.

A low-noise amplifier (***14***) with amplification factor control range 0 – 50 dB is of vital importance in the formation of signal/noise ratio at spectrometer output. The excess noise and parasitic harmonics are attenuated by means of high-pass filter (***17***) whose cutoff frequency is set lower than NQR resonance frequencies (0.2 – 1 MHz). The choice of filter passband is mainly caused by resonance signal bandwidth.

To extract complex envelope of received radio signal, one must get rid of carrier ω_0, that is, perform spectrum transfer to low-frequency area. A quadrature detector is based on two balanced mixers (***19***, ***20***) with the identical and phase shifted by 90º reference frequencies (***13***, ***15***). The former is adjusted for recording the sine component of NQR signal, and the latter – the cosine component. In a real experiment, both detectors record a mixture of both orthogonal components. The obtained signals are real and imaginary parts of complex NQR spectrum. One of fundamental advantages of quadrature detection is increase of signal/noise ratio by a factor of $\sqrt{2}$, so the majority of modern spectrometers employ precisely this method of signal extraction from noise. Moreover, this detection method is widely used in two-dimensional NQR spectroscopy. For the operation of quadrature detector in key mode use was made of comparator units (***16***, ***18***) converting sine-shaped reference signal into rectangular pulses. As a result of multiplication of received signal $s(t)$ generally having a continuous spectrum $s(\omega)$, there is transfer of spectrum to reference signal with frequency ω_0 along the frequency axis by the value equal to reference signal frequency ω_0. Signals from quadrature detector through matching amplifiers (***21***, ***22***) arrive at the 6-th order low-pass Butterworth filters (***23***, ***24***) assuring filtration of useful signal from the double-frequency components. As long as detector passband is determined by low-pass filter (LPF) cutoff frequency, the effective value of frequency range of the latter is determined by the width of spectra under study and can vary in the range of 0–500 kHz.

The NQR response signals (echo or FID) from the outputs of low-frequency

filters through adder (***25***) arrive at the oscillograph and spectrum analyzer. In a real experiment, it is necessary to assure separate analog to digital conversion (ADC) of signals from the outputs of each filter (***23***, ***24***) for the purpose of further mathematical processing of quadrature and in-phase components of resonance spectra in a specialized software.

As is known, the NQR response signals are rather weak, and in case studying substances with a low concentration of resonating nuclei make microvolt units. This results in masking useful signal by the noises of radio spectrometer receive-transfer path and by the external destabilizing effects. To approach as nearly as possible the conditions of physical experiment and take into account the above factors, the simulation model shown in Fig. 2.2 includes the sources of noise signals with a uniform distribution and a restricted frequency band.

2.2 Simulation model of RF transmitter of pulsed NQR spectrometer

The specific feature of NQR is considerable expansion of lines caused by dipole-dipole interaction of nuclei on substance solid phase. In addition, local field inhomogeneity caused by defects and tension in the crystal matrix also makes a significant contribution to the line width. To study by pulsed NQR method the objects with a low content of quadruple nuclei, it is desirable to form high-power excitation pulses ($P_{out} \approx 1000$ W) which, in turn, requires coefficient of amplification of radio-frequency transmitter of NQR spectrometer 50 dB. Consider the structure of transmitter for a pulsed NQR spectrometer by the example of its simulation model [10, 11] shown in Fig. 2.4. The transmitter model comprises a pulse shaper [8] and a linear power amplifier whose output is loaded by LC oscillating circuit – the sensor of NQR spectrometer.

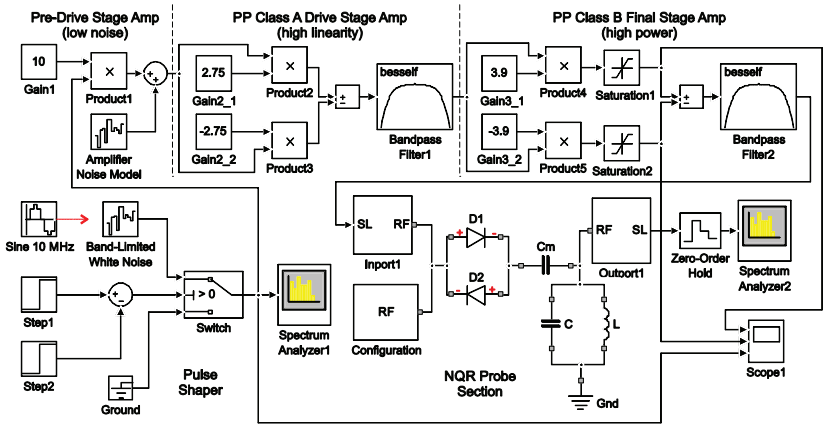

Fig. 2.4 Simulation model of RF transmitter of pulsed NQR spectrometer

As is evident from the proposed model, the RF transmitter comprises three stages with total amplification ~ 46.6 dB. To improve energy efficiency, the second and third stages of the transmitter are most important, since they work in linear amplification modes and, hence, the largest amount of thermal energy is dissipated on their active elements. Based on the proposed model, parametric computer identification (simulation) was performed with maximum possible account of real experimental parameters for the cases of amplification of excitation pulses with a sinusoidal and a noise carrier. The source of noise signals is a "Band-Limited White Noise" unit. The profiles of instantaneous values in the output circuits of active elements of RF transmitter output stage are shown in Fig. 2.5. It is seen that with a relatively simple circuit design the transmitter simulates equally well the shape of sine and noise-like signals.

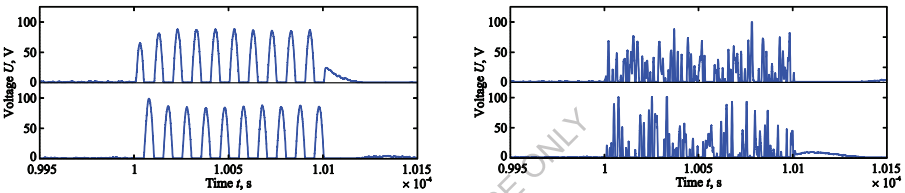

Fig. 2.5 Voltage profiles in the output circuits of push-pull output stage of RF transmitter obtained at amplification of sine – (a) and noise – (b) signals

Operating frequency band is an important characteristic of pulsed spectrometer RF transmitter. Power spectral density of white Gaussian noise is constant in the infinitely broad frequency range. To reproduce the real experimental conditions, the transmitter pass band was set at the level of $\Delta F_{TX} = 0.5 – 50$ MHz due to the use of "Bandpass Filter" units. Signal bandwidth Δf at transmitter output was studied as a function of pulse duration $\Delta\tau = 1 – 100$ μs with sine (Fig. 2.6.1) and noise (Fig. 2.6.2) filling. In modeling the maximum spectral width was limited by the radio spectrometer receiving channel bandwidth ($\Delta F_{RX} = 1$ MHz) with central frequencies of 20 MHz and 50 MHz.

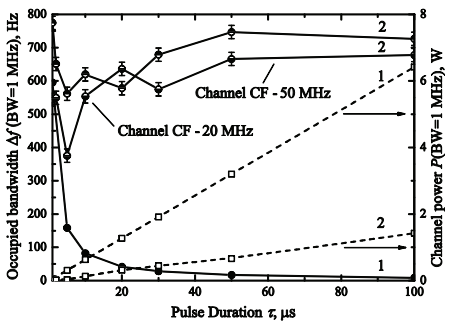

Fig. 2.6 Dependence of signal Δf at transmitter output on τ at excitation with radio pulses – (1) and noise pulses – (2)

In the case of amplification of radio pulses, efficiently and independently of the receiving channel center frequency, the following condition is relevant – the shorter pulse duration, the broader its spectrum. For noise signals two steps can be singled out. For a short duration of probe pulse ($\tau_1 \sim 1$ μs) occupied by noise with the band ΔF_{TX}, its energy spectrum (Fig. 2.7a) is an averaged characteristic of frequency properties of the number of random signal implementations restricted in the interval τ_1. As long as the latter in the case of short pulses is low, in the receiving channel with the band ΔF_{RX} one can observe a dependence $\Delta f(\tau_1)$ inherent in the pulses with sine occupation. With increasing duration of probe pulse ($\tau_2 \to 100$ μs) occupied by noise with a band restricted to ΔF_{TX}, the energy spectrum becomes more uniform (Fig. 2.7b) due to increased number of implementations. In this case the dependence $\Delta f(\tau_2)$ (Fig. 2.6) increases to 600 – 700 kHz and is actually restricted to radio spectrometer receiver's pass band ΔF_{RX}.

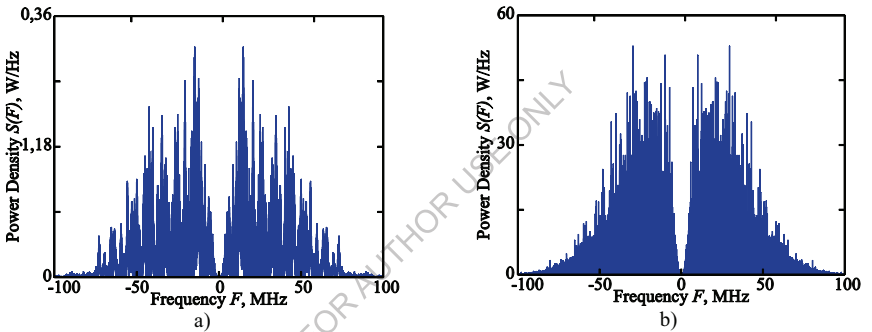

Fig. 2.7 Energy spectra of signal at the output of radio spectrometer transmitter in the case of excitation with noise pulsed signals at $\tau_1 = 1$ μs – (a) and $\tau_2 = 100$ μs – (b)

The stages of proposed broadband RF transmitter operate in A and B classes characterized by considerable power consumption and increased power dissipation. If drain voltage utilization factor is close to unity, the efficiency of transistor stage for A class ($\Theta = \pi$; $\alpha_0 = 0.5$; $\alpha_1 = 0.5$) and B class ($\Theta = \pi/2$; $\alpha_0 = 0.318$; $\alpha_1 = 0.5$) is $\eta_A \approx 0.5$ and $\eta_B \approx 0.79$, respectively [12]. In a real case the efficiency value is considerably lower.

An output push-pull stage of spectrometer transmitter is based on a circuit with a common source. When using the transmitter in amplification mode, in the output circuit of each branch there is direct current flowing from supply source I_{D0} and the first harmonic of alternating drain current I_{D1} caused by the effect of harmonic exciter voltage in the input circuit. Taking into account that instantaneous drain voltage $e_D = E_D - U_{mD}\cos\omega t$, we obtain power dissipated by the transistor

$$P_{dp} = \frac{1}{2\pi}\int_0^{2\pi}\left(E_D - U_{mD}\cos\omega t\right)\cdot\left(I_{D0} + I_{D1}\cos\omega t\right)d\omega t = P_0 - P_{out}, \qquad (2.8)$$

where E_D is supply voltage, U_{mD} is first harmonic amplitude of variable component of RF excitation, $P_0 = E_D I_{D0}$ is consumed power and P_{out} is net power given to the load (oscillating circuit). In the case of pulse signal amplifier the average value of power P_d which is dissipated on active components is a duty-cycle parameter D

$$D = \frac{\tau}{T}, \qquad (2.9)$$

where τ is radio pulse duration, T is radio pulse repetition period.

Boundary operating mode is optimal for transmitter, since in this case the net power and efficiency are maximum and pulse shape of RF excitation is minimum distorted. Based on the energy balance equation (2.8) and parameters of transistors used, factors determining the energy efficiency of transmitter at given T and τ were calculated. With regard to powers dissipated in the pulse by transistors of both stages and (2.9), the average power dissipated on transistors during a long period of time

$$P_d = D\left(P'_{dp} + P''_{dp}\right) + P_{Dq}.$$

The results of calculations performed for both transmitter stages at $T = 2$ ms and $\tau = 200$ μs are summarized in Table 2.2.

Table 2.2 Results of calculation of transmitter energy parameters

Transmitter stages	P_{out}, W	P_{dp}, W	P_d, W	P_{Dq}, W
Drive	29.37	41.39	28.14	24
Output	499.98	266.25	34.63	8
Both	-	307.64	62.77	32

From the results presented in Table 2.2 it is seen that essential contribution to the value of total average power P_d dissipated by transmitter active components is made by power dissipated in quiescent mode P_{Dq}:

$$P_{Dq} = P'_{Dq} + P''_{Dq},$$

where P'_{Dq} and P''_{Dq} are dissipated powers in quiescent mode for the intermediate and output stages.

For the reduction of P_{Dq}, pulsed bias control of transistor operating points was realized. Transistors enter the operating mode within a short time interval $\tau_{add} = 0.5 - 1$ μs, which leads the moment of excitation pulse start. With a pulsed bias the average power dissipated on transistors for a long period of time can be found by the equation

$$P_{d\_pulse} = D\left(P'_{dp} + P''_{dp}\right) + \frac{\tau + \tau_{add}}{T}\left(P'_{Dq} + P''_{Dq}\right). \qquad (2.10)$$

Such a solution allows considerable reduction of P_{d_pulse} (2.10) in operation of a linear amplifier in pulsed bias modes with duty-cycle $D < 0.1$. Fig. 2.8 gives the results of simulation of $P_d(D)$ and $P_{d\_pulse}(D)$ dependences for each stage and amplifier as a whole. From the plots it is evident that in pulsed bias mode at $\tau_{add} = 1$ μs the dissipated power reduced by 98.39 – 45.8 % for radio pulses of ratio $0.001 \le D \le 0.1$.

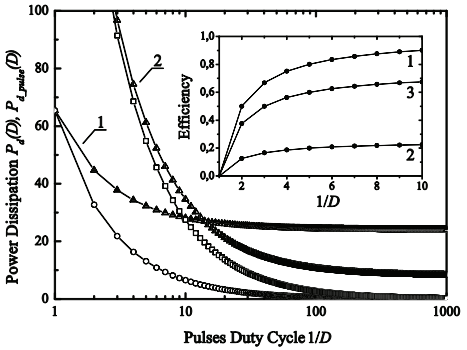

Fig. 2.8 Results of simulation of power characteristics of RF transmitter with a continuous (▲) and pulsed (□) bias for drive – 1, output – 2 stages, and total – 3

2.3 Synthesis of the configuration structure of digital receiver of NQR radiospectrometer

It is known that in the pulsed NQR, the FID signals are detected by transferring the resonance spectrum of width Ω to the LF range by subtracting the reference frequency ω_0, which is close to the frequency of the resonating nucleus. The method for detecting FID signals which is partially considered in [1, 13] requires a more thorough analysis, since its implementation governs the accuracy of visualization of complex resonance spectra, especially when it comes to multi-pulse experiments. The features of the Fourier transform create additional problems when selecting the reference frequency for the synchronous detector ω_0. At first glance, it is logical to set ω_0 in the center of the spectral range Ω (Fig. 2.9a) and to use only one component of the signal $\omega_0 \pm \Omega/2$ for the Fourier transform. However, in this case, the positive and negative frequencies of the resulting spectrum will be inseparable [14].

Often, for detection of FID signals another method is used which lies in arrangement of frequency ω_0 at one of the edges of spectral range Ω (Fig. 2.9b) [6]. Although in this case all detected signals will have the same sign (for example, choose the band $\omega_0 + \Omega$), but the effect of resonance conditions derangement will result in nonuniform excitation and a decrease in the signal-to-noise ratio. Moreover, additional noise from the opposite with respect to ω_0 spectral band $\omega_0 - \Omega$ during syn-

chronous detection will be added to the noise in the operating band $\omega_0 + \Omega$. One of the solutions to this problem is the formation of separate frequencies for excitation and detection of resonance, which is often a technically challenging task [15]. Another option is to apply a quadrature detection of FID which allows an increase in the signal-to-noise ratio by a factor of $\sqrt{2}$ [16].

Apart from increasing sensitivity, the use of quadrature detection imposes some restrictions. The main problem is that the suppression of unnecessary peaks when adding two signals will occur only under the condition of exact equality of their amplitudes and phase difference of 90°. In reality, the implementation of these conditions is practically impossible, therefore, in the spectra there are small residual signals - quadrature reflections [14]. The amplitude of the latter does not exceed 1% of the main signal, so they are harmful only when measuring weak peaks on the background of relatively intense.

In [8], the authors considered the development of a frequency synthesizer and a pulse train driver for a nuclear quadruple resonance spectrometer. Structure configuration of the direct frequency synthesizer (DDS) and the pulse train driver was carried out using the technology of optimizing the resources of the programmable crystal. As a result, about 50% of hardware resources in FPGA are not yet involved. The principle of building a configuration structure, which ensures the implementation of software-defined radio (SDR) with direct digitization of the signal and its integration on the basis of the remaining free hardware resources of FPGA is considered below.

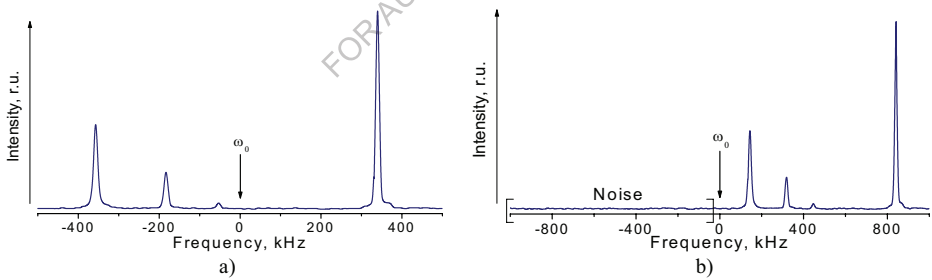

Fig. 2.9 Selection of reference frequency ω_0 of synchronous detector during pulsed excitation of NQR: a – in the centre of range Ω, b – at the edge of range Ω

Fig. 2.10 shows a model of RF receiver of pulsed NQR spectrometer in which the SDR technology is chosen for the implementation of a quadrature detector with a system of filtration and suppression of quadrature reflections. The receiver is based on the principle of digital down-converter (DDC), which significantly reduced the length of its analogue path, and therefore reduced the noise of the FID signal and the asymmetry of detected signal parameters. The experimental model of the receiver involves a high-speed 12-bit ADC (170 MSPS) which is used to digitize the response signal in the range of resonance frequencies 1 – 50 MHz [17, 18].

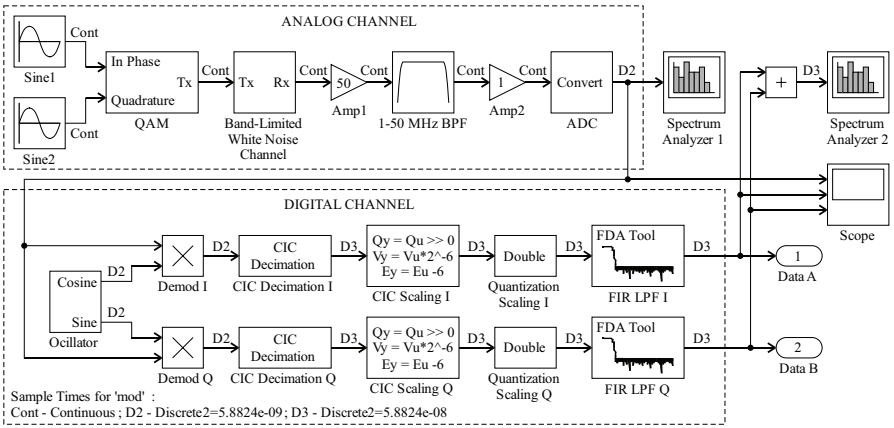

Fig. 2.10 Simulation model of the proposed receiver of NQR spectrometer

To simulate the receive path of the spectrometer, in MATLAB Simulink a test radio signal was synthesized, representing a carrier oscillation at 30 MHz with an envelope in the form of a sum of two harmonics – 400 kHz and 800 kHz In this case, the band radio signal

$$s(t) = a(t)\cos\big(\Phi(t)\big) = a(t)\cos\big(\omega_0 t + \varphi(t)\big)$$

is a real part of a complex signal $z(t)$ [19]:

$$z(t) = a(t)\cos\big(\omega_0 t + \varphi(t)\big) + j \cdot a(t)\sin\big(\omega_0 t + \varphi(t)\big) = z_m(t)\exp(j\omega_0 t),$$

where a complex envelope equals:

$$z_m(t) = a(t)\exp\big(j \cdot \varphi(t)\big) = a(t)\cos\big(\varphi(t)\big) + j \cdot a(t)\sin\big(\varphi(t)\big) = I(t) + jQ(t).$$

The concept of quadrature modulation lies in multiplication of complex envelope $z_m(t)$ by complex frequency $\exp(j\omega_0 t)$. The finite equation for the synthesis of radio signal [19] is the following:

$$s(t) = \mathrm{Re}\big[z(t)\big] = I(t)\cos(\omega_0 t) - Q(t)\sin(\omega_0 t). \qquad (2.11)$$

As can be seen from Fig. 2.10, the receiving channel of the spectrometer consists of analog and digital paths. The functional elements of the analog channel are amplification modules “Amp1”, interface modules “Amp2” and a bandpass filter “BPF”. The latter serves to suppress parasitic signals outside the band of spectrometer operating frequencies. A link with a digital path is an ADC block which simulates the work of a 12-bit ADC at a sampling frequency of 170 MHz.

The digital path of the receiver ensures complex envelope extraction of radio signal $z_m(t)$ by multiplying radio signal (2.11) by $\exp(-j\omega_0 t)$, which provides transfer of the spectrum to the region of zero frequencies. The detection process will generate a following signal:

$$z_d(t) = s(t)\exp(-j\omega_0 t) = A(t) + jB(t),$$

with complex components:

$$\begin{aligned} A(t) &= \frac{1}{2}I(t) + \frac{1}{2}I(t)\cos(2\omega_0 t) - \frac{1}{2}Q(t)\sin(2\omega_0 t), \\ B(t) &= \frac{1}{2}Q(t) - \frac{1}{2}Q(t)\cos(2\omega_0 t) - \frac{1}{2}I(t)\sin(2\omega_0 t). \end{aligned} \tag{2.12}$$

The process of digital processing of the demodulated components (2.12) of the FID signal lies in reducing their sampling rate (decimation) and filtering from the components of double frequency $2\omega_0$. Signals received from the outputs of "demod" multipliers still have a high sampling rate (170 MHz). To construct the resonance spectra of NQR with a maximum width of the spectral band Ω equal to 1 MHz, it is sufficient to have a value which is an order of magnitude lower, so in the digital path of the SDR receiver, 5-cascade integral comb filters with an infinite impulse response (cascaded integrator–comb (CIC) decimation modules in Fig. 2.10) are used, which provide a reduction of the sampling rate to 17 MHz. However, as a result of operation of CIC filters, the bit capacity of the output signals increases due to the reduction of their bandwidth, therefore, in the simulation model of the receiver, quantization scaling modules are introduced for artificial limitation of the bit capacity to 16 bits [18].

Fig. 2.11 shows frequency responses obtained in MATLAB for CIC and compensating finite impulse response (FIR) filters.

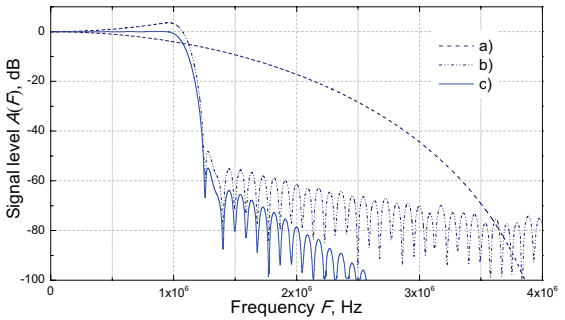

Fig. 2.11 Simulation results of digital filters frequency responses: a – CIC, b – compensating FIR, c – total characteristic

Unfortunately, CIC filters have a rather steep amplitude-frequency response, which goes down to 0 when approaching the sampling frequency. The curvature of frequency response is compensated by "FIR low pass filter" modules that are nonrecursive filters with a finite impulse response.

The output signal and transmission characteristic of compensating filter are represented by the dependencies:

$$y(n) = \sum_{k=0}^{N-1} h(k)x(n-k),$$

$$H(z) = \sum_{k=0}^{N-1} h(k)z^{-k},$$

where $x(n)$ is input influence, $h(k)$ are impulse response coefficients, N is the number of filter coefficients.

As a result of computer parametric identification of information transformations in analogue-digital paths of the proposed SDR for the NQR pulse spectrometer, the voltage oscillograms (Fig. 2.12) and spectral characteristics (Fig. 2.13) of the quadrature components of the demodulated FID signal were obtained.

The high efficiency of digital quadrature detection with the use of direct signal digitization technology is also confirmed by the low content of the dual frequency components in the spectrum of the receiver output signal. In particular, with a sampling frequency of 17 MHz and a cutoff frequency of the compensating LPF of 1 MHz, the level of side and out-of-band emissions in the effective bandwidth of the SDR is not more than -100 dB.

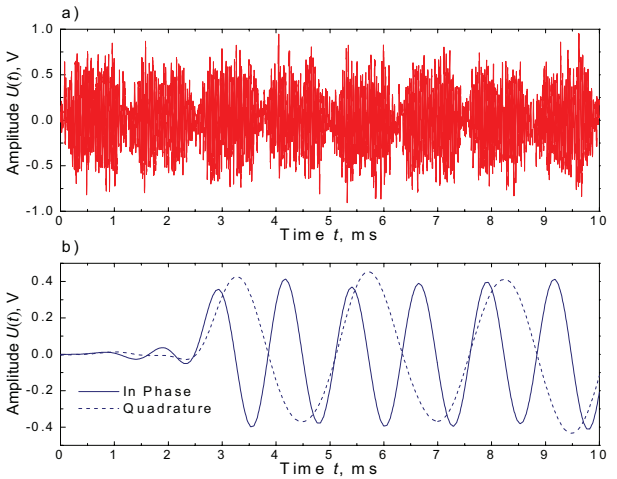

Fig. 2.12 Voltage oscillograms in the paths of proposed receiver: a – modulated oscillation, b – demodulated components of the quadrature amplitude modulation (QAM) signal

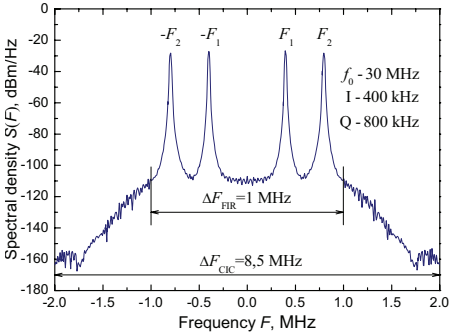

Fig. 2.13 Energy spectrum of demodulated signal. The peaks F_1 ($-F_1$) and F_2 ($-F_2$) reflect the information components of the QAM signal

2.4 Simulation of ^{115}In NQR spectra

Computer simulation of signal transformations in the receive-transfer path of pulsed spectrometer was performed on the basis of the above simulation model with integrated NQR-subsystem. The requirement for correct conduction of experiment that determines the accuracy of numerical calculation and the criteria for representation of continuous signals by the combination of their discrete readings is correct selection of the basic data for the virtual experiment. Simulation was performed in MATLAB Simulink programming environment on the workstation comprising Intel Core i7 microprocessor with clock frequency 3.7 GHz and 32 GB RAM of the type DDR4. To perform the formulated research task, simulation was performed under the following conditions:

- test signal – sine, white noise;
- operating frequency range – 1 – 50 MHz;
- sampling frequency – 1 GSa/s.

To reduce computation load on Simulink and computer, the structure of spectrometer was somewhat simplified (with elimination of automatic gain control and ADC units), which in general did not reduce the informativeness of the results obtained.

To verify the results of simulation of signal transformations in pulsed NQR-spectrometer, indium selenide single crystal was selected wherein complex broadband ^{115}In NQR spectra are observed that are well studied experimentally [1, 20–23]. Indium selenide belongs to layered semiconductor materials whose crystalline structure is formed in such a way that chemical bonds within the basic layer are mainly covalent, and between the layers they are of Van der Waals nature. Owing to this, in InSe monoatomic Se-In-In-Se layers are formed with axial-symmetric electric field gradient in the direction of In-In [23, 24]. As long as ^{115}In has spin $I = 9/2$, in conformity with selection rules there are four resonance transitions: $\pm1/2 \leftrightarrow \pm3/2$; $\pm3/2 \leftrightarrow \pm5/2$; $\pm5/2 \leftrightarrow \pm7/2$; $\pm7/2 \leftrightarrow \pm9/2$. Simulation was performed for one spin

transition $\pm 3/2 \leftrightarrow \pm 5/2$, and NQR frequency corresponding to it can be found from equation [25]:

$$\nu = \frac{2}{24} eQq_{zz}(1 + 1{,}338\eta^2 - 11{,}724\eta^4), \tag{2.13}$$

where e is electron charge, Q is nuclear quadrupole moment, q is electric field gradient in the direction of axis c and η is asymmetry parameter of the electric field gradient.

NQR excitation was done by probing pulse of duration $\tau_{exc.} = 10$ μs and power P = 1000 W. The basic frequency of probing pulse was set to be 20 MHz. Simulation time was about 2 min. Fig. 2.14 shows NQR response signal that was recorded at the input to receive path. Signal/noise ratio for FID input signal was less than 20 dB. Digital processing of signal in this form will result in nonoptimal use of the digits and speed characteristics of ADC data acquisition system of NQR.

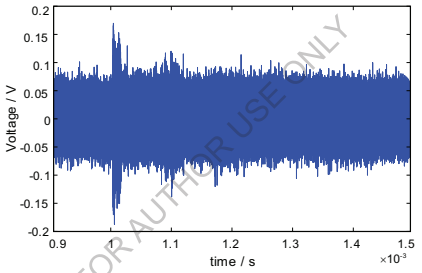

Fig. 2.14 The ^{115}In FID in InSe at the input to pulsed radio spectrometer receiver

Fig. 2.15a shows FID signal after quadrature detection and filtration, and Fig. 2.15b – amplitude spectrum obtained as a result of FFT of FID signal. NQR multiplicity leads to a complicated shape of beating in nuclear induction decay. Transfer of spectrum to low-frequency area allowed more efficient processing of resonance signals. Comparison of oscillograms in Fig. 2.14 and Fig. 2.15a has shown that signal/noise ratio has increased considerably.

As long as NQR signal frequency depends on the electric field gradient, its precise value, hence the required filling frequency of probing pulse is often unknown.

It is proposed here to use probing pulses with noise filling for preliminary identifying the expected range of resonance frequencies. It is known that noise signals are characterized by random time function. In the case when spectral density of noise voltage $e(\omega)$ or current $i(\omega)$ is frequency independent, the distribution of power spectral density is uniform in the frequency range and signals with uniform distribution can be efficiently used for resonance search on "unknown" frequencies.

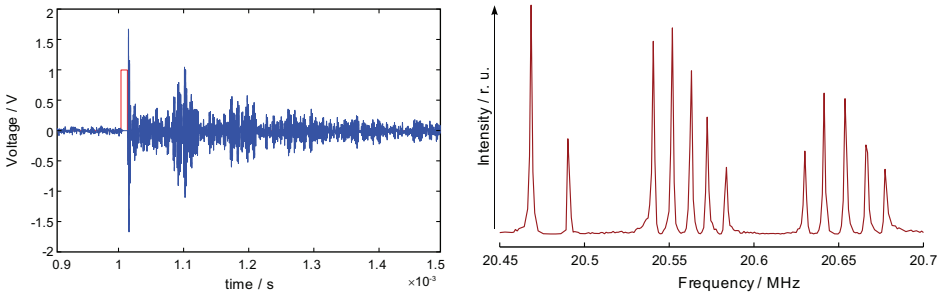

Fig. 2.15 The ^{115}In NQR signal in InSe at the output of pulsed radio spectrometer receive path: A – FID selected from noise after quadrature detection and filtration; B – NQR spectrum obtained with the use of fast Fourier transform (FFT) of FID signal

With excitation of resonance system by noise signal one cannot anticipate which implementation will be obtained in this particular experiment, hence it is impossible to record response signal with a certain probability of its existence. Hence, to perform this research it is necessary to retain statistical characteristics typical of random process with a uniform distribution and conduct an infinitely large number of experiments.

To confirm the efficiency of NQR noise excitation, computer simulation of this process was performed in MATLAB Simulink software with the use of methods for digital accumulation and averaging of the obtained results. Experimental conditions are similar to the above, except for the source of reference signal (***I***). As long as noise generator is chosen in the capacity of the latter, problems arise due to formation of reference signal frequency for the receive path detector.

As is seen from Fig. 2.16a, with a noise excitation of NQR in each subsequent experiment we obtain different implementations of FID signal. However, with the use of digital accumulation and data averaging intercorrelation between neighbouring iterations increases (Fig. 2.16b). This is proved by the results of statistical correlation analysis represented in Fig. 2.17. In this case, digital data averaging is used starting from 50-th iteration, and already after almost 10 iterations the coefficient of correlation drastically increases, reaching the values of 0.8 – 0.92.

The algorithm of proposed express method is represented by a sequence of the following operations:

1) excitation of resonating nucleus by the 1-st probing pulse with noise filling;

2) recording FID signal;

3) excitation of resonating nucleus by the N-th probing pulse;

4) averaging the data of N iterations;

5) calculation of the Pearson correlation coefficient r between averaged signals during $N - 1$ and N iterations;

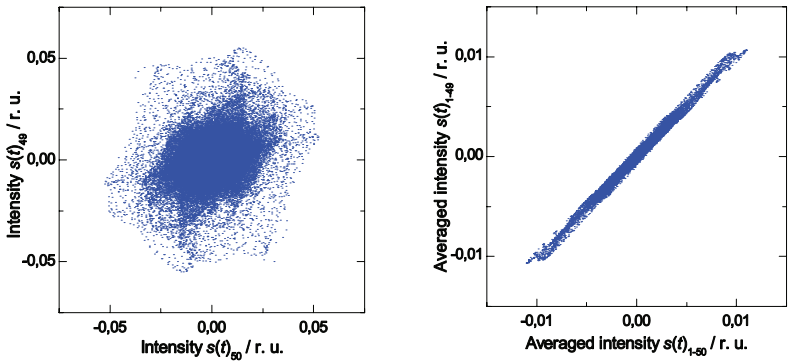

Fig. 2.16 Scattering diagrams for FID signal: A – between the 49-th and 50-th iteration without averaging, B – between averaged signals during 1–49 and 1–50 iterations

6) in the case when $r \geq 0.75$ – termination of excitation pulses effect and use of FFT till the obtained averaging result;

7) mathematical processing of the resulting NQR spectrum with a view to determine its width $2\Delta\omega_s$, central frequency ω_s and other parameters necessary for adjustment of modes of spectrometer functional units;

8) automatic setting by synthesizer of frequency ($\omega_0 = \omega_s$) of reference signal for the detector of spectrometer receiver;

9) excitation of resonating nucleus by probing radio frequency pulse with frequency ω_s;

10) more precise recording NQR signal by means of quadrature detection with spectrum transfer to low-frequency band.

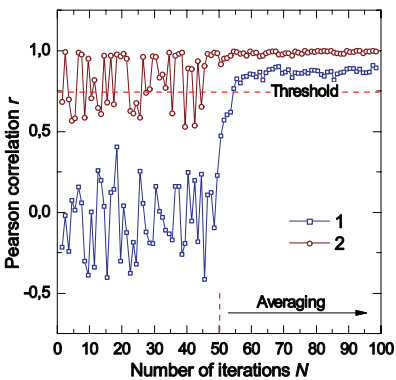

Fig. 2.17 Results of statistical Pearson correlation analysis (signal averaging is used from the 50-th iteration): 1 – for FID signals, 2 – for NQR spectra

Fig. 2.18 shows the results of simulation of resonance excitation by a series of noise pulses in the form of ^{115}In NQR spectrogram and its plane sections. In the time range t_1–t_2 = 6 ms noise excitation was used without averaging the results obtained. Starting from the time moment t_2 digital averaging of the accumulated research results was employed.

Spectrogram section in time plane (Fig. 2.18, line "α" on top) reflects a change in power spectral density of separate "α" line of time variable multiplet NQR spectrum. The discreteness of characteristics is affected by the number of experiments N, in this case $N = 40$. On achievement of certain time $t_3 \approx 9$ ms as a result of averaging the spread in power spectral density corresponding to "α" line is reduced to the necessary level which makes possible preliminary identification of resonance frequency. Similar pattern is observed for other multiplet spectrum lines. Spectrogram section in frequency plane along "L" line (Fig. 2.18, right) visualizes the ^{115}In NQR spectrum whose arrangement corresponds to time moment t_4 = 18 ms. The time of simulation of the experiment on the noise excitation of NQR of total duration 0.02 s was ~ 72 min.

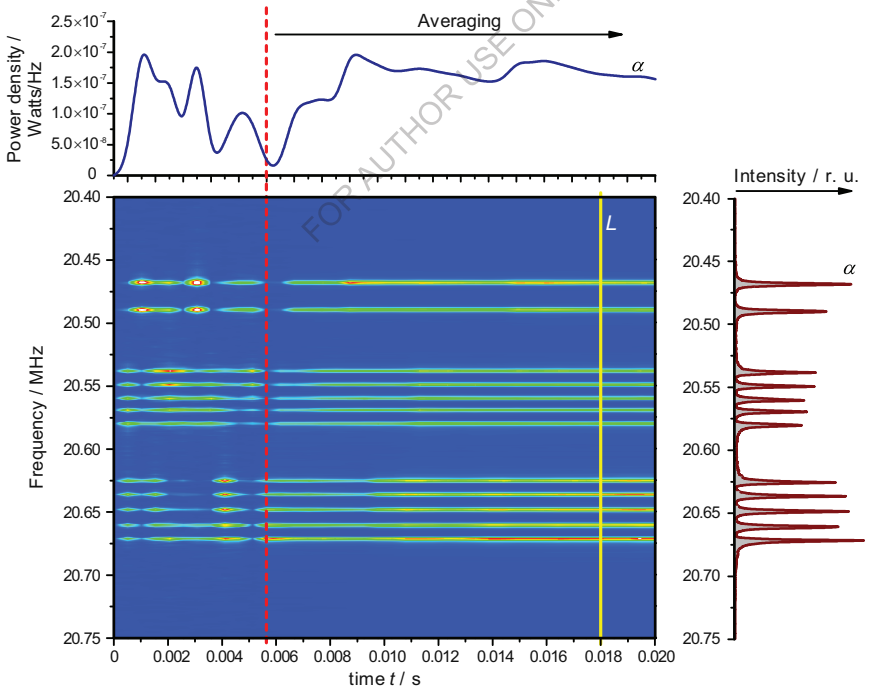

Fig. 2.18 NQR ^{115}In spectrogram obtained at resonance excitation by probing pulses with noise filling

2.5 Simulation of magnetic field topology in a saddle-shaped coil of NQR spectrometer

The signal to noise ratio (SNR) at spectrometer output is determined by the noise ratio of microwave spectrometer input stage and, primarily, by the quality of receiving coil or resonator. For the analytical estimation of SNR ratio of spectrometers working in very high frequency range one can use the following expression [9, 26]:

$$\mathrm{SNR} = \frac{1}{8} \cdot \left(\frac{\omega_0^3 \cdot \eta \cdot Q \cdot V_S}{2 \cdot \mu_0 \cdot k \cdot T \cdot F \cdot b_R} \cdot \frac{T_2}{T_1} \right)^{1/2} \cdot \frac{\chi_0}{\gamma}, \tag{2.14}$$

where η is filling ratio; Q is quality factor of resonance loop; V_S is sample volume; T_1 and T_2 are nuclear spin-lattice and spin-spin relaxation times; μ_0 is magnetic permeability of medium; k is the Boltzmann constant; T is absolute temperature; F is noise ratio of preamplifier; b_R is transmission bandwidth of microwave spectrometer amplification path; χ_0 is magnetic susceptibility of substance under study; γ is gyromagnetic ratio for resonating nuclei.

From expression (2.14) it is seen that under all other conditions with formation of SNR ratio of primary significance is the factor of quality of receiving coil ηQ. The figure of merit of the coil can be improved through optimal combination of structural features, namely the number of coils, wire quality, shape configuration, inductance for given frequency, etc.

Parameter η is a function of coil volume filled with substance. In fact, it also depends on the homogeneity of the field where the sample is placed. That is why some effective value η' is introduced, which depends on the distribution of high-frequency field in the sample filling the coil. This is particularly important with pulse detection of resonance signal where maximum intensity of response signal is largely dependent on the intensity of high-frequency field in the coil ($\boldsymbol{B}_1$) during the pulse of duration t_i and is achieved under condition [27]

$$\gamma B_1 t_i = \pi / 2, \tag{2.15}$$

where $\pi/2$ is rotation angle of nuclear spins. In powder-like samples for NQR such an angle can be $0.66\,\pi$. In the presence of high-frequency field intensity gradient within the sample, in the process of response signal formation there is "blurring" of total vector of spin magnetization, which results in the expansion of resonance signal and the reduction of its intensity amplitude. Increase of high-frequency field uniformity is particularly important for detection of weak signals observable in the study of substances with a low natural abundance of magnetoactive nuclei. With a nonuniform high-frequency field, a complete filling of the coil with a substance under study does

not result in expected signal amplification according to expression (2.14). So, when configuring and manufacturing the coil, the factor of quality ηQ with regard to field uniformity is of decisive importance for optimizing the conditions of resonance signal generation.

The topology of high-frequency field intensity in solenoid coil of microwave spectrometer detector was considered in [28]. To provide for a restricted zone for scanning of sample under study and more efficient interaction of high-frequency field and crystal for excitation and reception of spin induction signal, it is reasonable to use a saddle-shaped spectrometer coil (Fig. 2.19), where the vector of high-frequency field $\boldsymbol{B}_1$ is directed normal to crystal growth direction. The use of a single-turn coil is due to the type of samples under study. The NQR spectra for instrumentally convenient spin transitions of InSe layered semiconductor crystals are in the frequency range of 30 – 40 MHz. Adjustment of NQR spectrometer in this range requires a low-inductance tuned-circuit coil, which is inherent in single-turn saddle-shaped coil. The signal/noise ratio for high-frequency coil can be represented by the expression [29, 30]:

$$SNR \approx \frac{\mathrm{B}_1 V \sqrt{Q} \mathrm{B}_0^{3/2}}{\sqrt{\Delta\omega}}, \tag{2.16}$$

where $\boldsymbol{B}_1$ is magnetic field induction created by receiving coil with a unitary current in it; V is excited volume of the sample; Q is quality factor of high-frequency system; $\boldsymbol{B}_0$ is induction of polarizing magnetic field; $\Delta\omega$ is bandwidth.

The value $\boldsymbol{B}_1$ governs coil sensitivity. So, the relative work volume of the coils should be maximized, for their conductors to be as close as possible to the object under study. The permissible field nonuniformity for recording of NQR with minimum distortions of resonance spectra should make 10 – 15% [30, 31].

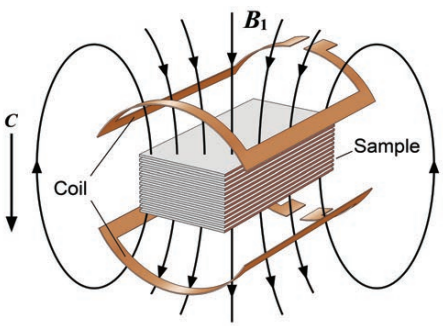

Fig. 2.19 Configuration of a saddle-shaped coil with arrangement of a crystal sample of layered semiconductor therein

To determine a magnetic field map, it is necessary to perform synthesis and create a field model of the coil. One of the first tasks when creating the field model is to determine the model geometry. For a more complete representation with regard to geometric features of a real configuration of saddle-shaped coil, its 3D model was developed (Fig. 2.20).

This model was developed with regard to recommendations as to geometry of saddle-shaped coils given in [30]. The total transverse component of radio-frequency coil field is determined by the field of four linear and four arc conductors:

$$\mathrm{B}_S = 4\left(\mathrm{B}_{YL} + \mathrm{B}_{YA}\right). \tag{2.17}$$

The transverse component of the field of 1D conductor of infinite length arranged in coordinates y_0, z_0, at point y, z is given by the expression

$$\mathrm{B}_{YL} = \frac{\mu_0 \mathrm{I}(z - z_0)}{2\pi\left[(y - y_0)^2 + (z - z_0)^2\right]}. \tag{2.18}$$

The field induction component of work conductor with start coordinates $x_1\, y_0\, z_0$ and end coordinates $x_2\, y_0\, z_0$ is defined by the expression

$$\mathrm{B}_{YL} = \frac{\mu_0 \mathrm{I}(z - z_0)}{4\pi r^2}\left(\frac{x_1 - x}{\sqrt{r^2 + (x_1 - x)^2}} - \frac{x_2 - x}{\sqrt{r^2 + (x_2 - x)^2}}\right). \tag{2.19}$$

The transverse component of magnetic field induction of the coil arc conductor is:

$$\mathrm{B}_{YA} = \frac{\mu_0 \mathrm{I}}{4\pi}\int_0^{\varphi} \frac{r_0(x_1 - x)\cos\varphi_0}{\left[r^2 + r_0^2 - 2rr_0\cos(\varphi_0 - \varphi) + (x_1 - x)^2\right]^{3/2}} d\varphi_0. \tag{2.20}$$

To improve field uniformity $\boldsymbol{B}_Y$, the optimal value of Δx and angular dimensions of coil arcs can be found by compensation of other derivatives of expressions for magnetic field induction of linear conductors (2.19) and arcs (2.20) with a view to remove the respective terms of power series expansion of these expressions [30].

The value of the angular dimension of arc areas is:

$$\varphi = 2arctg\left(\frac{y_0}{z_0}\right) = 120^{\circ}. \tag{2.21}$$

On the assumption of maximum inhomogeneity of component $\boldsymbol{B}_{YA}$ of the field of 1D conductors, their length is:

$$\Delta x = 2(1{,}26 r_0). \tag{2.22}$$

For the calculation of 3D fields, wide application has been gained by computer programs based on finite element method, such as ANSYS, ABAQUS, COMSOL, ELCUT. Extensive use of 3D simulation is constrained by the absence of clear theoretical substantiation of the formulation of electromagnetic field numerical calculation problems which in some cases are beyond the scope of classical theory of electromagnetic field. First of all, this concerns the formulation of problems of electromagnetic field calculation with respect to vector magnetic and scalar electric potentials [32]. Magnetic field topology of a saddle-shaped coil was analyzed in COMSOL Multiphysics V 4.4, which offers vast opportunities in the field of simulation of electromagnetic, thermal, mechanical, acoustic and other fields [33]. The problem of magnetic field calculation was formulated with respect to vector magnetic potential $\boldsymbol{A}$ [34]. Taking into account the original dimensions of samples under study and the relations (2.21) and (2.22), a computational domain was created which is a model of physical structure of a saddle-shaped coil for which the numerical simulation is done. The model describes a system of coil with the following parameters: radius $r_0 = 10$ mm, length $\Delta x = 25.2$ mm, opening angle of arc areas $\varphi = 120^{\circ}$ (Fig. 2.20). Copper with the electric conductivity $\sigma = 5.998 \cdot 10^{-7}$ S/m and relative magnetic permeability $\mu_r = 0.99999$ was selected as material for coil conductors.

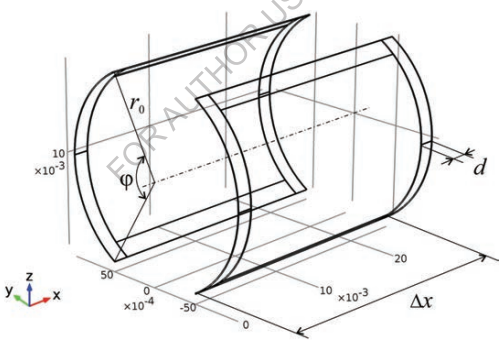

Fig. 2.20 3D image of a geometrical model of a saddle-shaped coil in COMSOL Multiphysics

In the development of this model the following initial conditions were assumed. This model was developed under the following assumptions. As long as the coil is to be made according to planar technology, by etching flat copper turns on the surface of thin printed circuit board (PCB) laminate material, the winding is considered to be single-turn, realized by a conductor of cross-section $1 \cdot 10^{-4} \times 1.6 \cdot 10^{-3}$ m. To simplify the analysis, coil turns are represented as closed perimeters with direct current flowing along them, and the influence of attached conductors is excluded. Current flow direction I_{coil} is simulated along the reference edges established for each coil turn. The area of magnetic field simulation is restricted by air sphere of electric conductivity $\sigma = 0$ S/m and relative magnetic permeability $\mu_r = 1$. Sphere radius is $R = 3 \cdot 10^{-2}$ m, air

temperature and pressure are assumed to be $T = 293.15$ K and $P = 1$ atm, respectively. On the external boundary of the computational region the boundary conditions were specified by the Dirichlet condition represented in the differential form. This allowed ignoring scattering fluxes that are closed through the air gap on the external boundary of the computational region by specifying magnetic isolation condition which by default in COMSOL Multiphysics is of the form $\boldsymbol{n} \times \boldsymbol{A} = 0$.

Calculation of magnetic field topology was done in *Magnetic Fields (mf)* module. As a result of triangulation of computation domain, finite element mesh was created with multiplexing in the area of field with maximum gradients (Fig. 2.21). Mesh size was chosen optimal with regard to the fact that its increase reduces the accuracy of simulation, and its decrease causes errors due to rounding of numbers in computer. Moreover, setting of minimum mesh size calls for essential expenditures of hardware computing power.

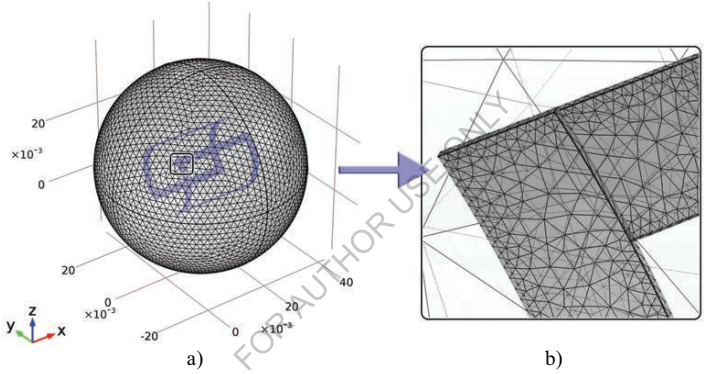

Fig. 2.21 Finite element mesh was obtained due to triangulation of computational domain: (a) – general view, (b) – detailed representation of coil fragment

In COMSOL Multiphysics a map of static magnetic fields can be calculated by solving a magnetostatic equation obtained from Ampere's law for static cases.

$$\nabla \times \mathrm{H} = \mathrm{J}, \tag{2.23}$$

where ∇ is differential Hamiltonian operator, $\boldsymbol{H}$ is magnetic field intensity, $\boldsymbol{J}$ is the amplitude of total electric-current density. The relations between magnetic field intensity $\boldsymbol{H}$ and magnetic flux density (induction) $\boldsymbol{B}$ are given by the dependences:

$$\mathrm{B} = \nabla \times \mathrm{A}; \tag{2.24}$$

$$\mathrm{H} = \mu_0^{-1} \mu_r^{-1} \mathrm{B}. \tag{2.25}$$

Taking into account the value of relative magnetic permeability for copper and the definition of vector potential of magnetic field $\boldsymbol{A}$, we can write the resulting differential magnetostatic equation as a modified Ampere's law:

$$\nabla \times \left(\mu_0^{-1}\mu_r^{-1}\nabla \times \mathrm{A}\right) - \sigma v \times \left(\nabla \times \mathrm{A}\right) = \mathrm{J}_e, \tag{2.26}$$

where μ_0 is magnetic permeability of vacuum, μ_r is relative magnetic permeability of copper, σ is electric conductivity, v is motion velocity, $\boldsymbol{J}_e$ is the amplitude of external current density.

The values of external current density are determined only in the model zones that represent a saddle-shaped inductance coil and are determined through current flowing along its perimeter:

$$\mathrm{J}_e = \frac{\mathrm{I}_{coil}}{S}, \tag{2.27}$$

where $\boldsymbol{I}_{coil}$ is given current and S is cross-sectional area of coil perimeter.

Processing of numerical simulation results was done by embedded COMSOL tools with the aid of the objects and options of "Results" item. This item automatically creates the objects necessary for graphical representation of results on completion of calculation, "Graphics" window shows graphical representation of numerical simulation results. Representation parameters were assigned depending on the representation of graphical results. The result of field topology simulation in a saddle-shaped coil with direct current flow $\boldsymbol{I}_{coil}$ = 10 A is shown in Fig. 2.22 as magnetic field lines (lines of equal magnetic potential). The simulation was done with regard to the boundary conditions describing magnetic field distribution at the boundaries of computational domain. 3D topology of magnetic field intensity in *XY* plane is represented in Fig. 2.23. From this figure it is seen that in the work area of coil under study there is a zone with a uniform distribution of the field, and for a more detailed study of its geometry it is necessary to process the results for individual sections of computational domain.

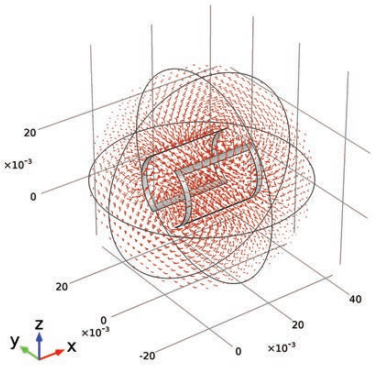

Fig. 2.22 Magnetic field lines in the computational domain of a saddle-shaped coil

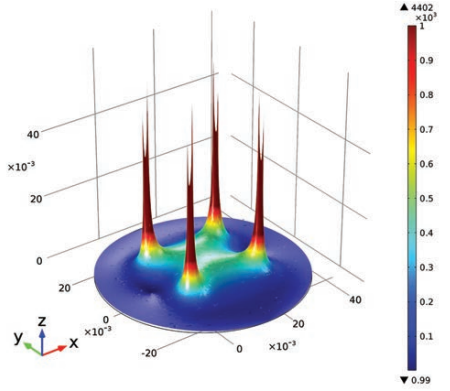

Fig. 2.23 3D topology of magnetic field intensity in *XY* plane of a saddle-shaped coil

Detailed simulation results are represented by 2D field maps in sectional areas *ZX, XY*, *YX* (Fig. 2.24 – Fig. 2.26). The dependences of magnetic field intensity distribution represented in these figures show that the zones of permissible field nonuniformity (not more than 15%) on either side of the geometrical centre of a saddle-shaped coil are: 12.3 mm along the *x* axis, 18.1 mm along the *y* axis, and 10 mm along the *z* axis.

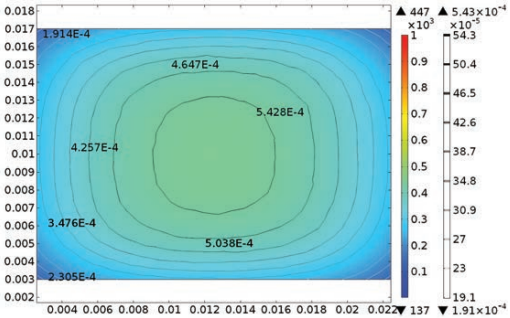

Fig. 2.24 Magnetic field topology in the work area of *ZX* plane of a saddle-shaped coil. Distribution of magnetic field intensity (gradient field) and induction (contour lines) in *ZX* plane

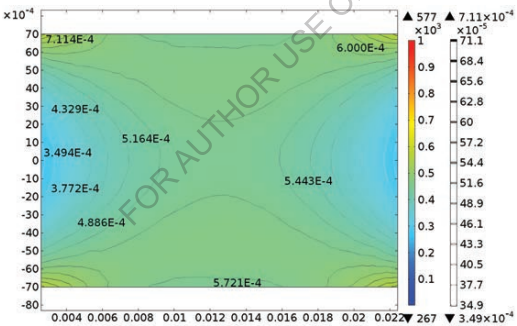

Fig. 2.25 Magnetic field topology in the work area of *XY* plane of a saddle-shaped coil. Distribution of magnetic field intensity (gradient field) and induction (contour lines) in *XY* plane

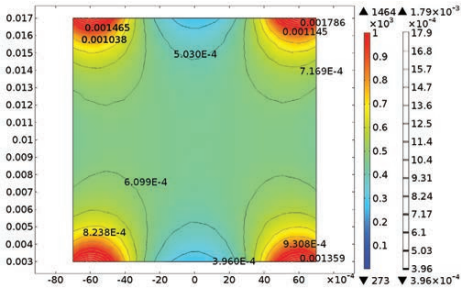

Fig. 2.26 Magnetic field topology in the work area of *YZ* plane of a saddle-shaped coil: distribution of magnetic field intensity (gradient field) and induction (contour lines) in *YZ* plane

According to the results of calculations performed and the field maps obtained, the relative volume of coil work area was determined which makes 28.12% of its full volume. For such a volume the recommended size of samples under study is $12 \times 18 \times 10$ mm^3.

2.6 Conclusions

Peculiarities of using *s*-simulation for parametric computer identification of broadband multiplet NQR spectra with the sine and noise excitation are considered.

A simulation model of a single-coil coherent NQR Fourier spectrometer without carrier frequency conversion is proposed, and the main steps of information transformation of FID signal are investigated. The simulated NQR ^{115}In NQR resonance spectra are obtained in a layered InSe crystal for spin transition $\pm 3/2 \leftrightarrow \pm 5/2$.

The method and algorithm for express-identification of NQR spectra are represented, which lie in resonance excitation in indium monoselenide by short noise pulses and digital processing of the obtained data. As a result of statistical correlation analysis it was established that with the use of digital accumulation and data averaging of FID signal, intercorrelation between the $N-1$-th and N-th iterations increases, and the Pearson correlation coefficient reaching the value sof 0.8 – 0.92, is the indicator of correct identification of resonance signal. The results of simulation of resonance excitation by a series of noise pulses are shown in the form of the ^{115}In NQR spectrogram and its plane sections. The method proposed can be efficiently used for resonance search on "unknown" frequencies the numerical values of which do not go beyond the operating band of spectrometer receiver.

Dependences of signal bandwidth at transmitter output on the duration of sinusoidal and noise excitation pulses were investigated. It is established that with a short duration of noise probe pulse (~ 1 μs) in a 1 MHz bandwidth receiving channel a dependence is observed which is inherent in δ – like radio pulses, and as this duration goes up to 100 μs, the bandwidth increases to 600 – 700 kHz and then is actually restricted to the bandwidth of radio spectrometer receiving channel.

In order to reduce power consumption and, as a consequence, total power dissipation, pulsed bias control of transistor operating points was used. As a result, the dissipated power was reduced by 98.39 – 45.8 % for radio pulses of relative duration $0.001 \le D \le 0.1$.

The structure and MATLAB Simulink model of a digital quadrature receiver of nuclear quadruple resonance signals were developed. The synthesis of compensating filters and computer simulation of signal transformations in the receive path of radiospectrometer were performed.

To provide for a restricted zone for scanning of a layered semiconductor sample

and a more efficient interaction of high-frequency field and crystal, an optimal work volume of a saddle-shaped coil of NQR-spectrometer was studied by calculation of magnetic field topology in the coil work zone using finite element method. Taking into account the original geometrical dimensions of samples under study, a computational domain was created which is a model of physical structure of a saddle-shaped coil of length $\Delta x = 25.2$ mm, radius $r_0 = 10$ mm and opening angle of arc areas $\varphi = 120^{\circ}$. A numerical simulation in COMSOL Multiphysics software was done, and 2D and 3D maps of static magnetic field intensity distribution of a saddle-shaped coil were calculated. It is established that for a one-turn saddle-shaped coil with the above geometric parameters the recommended size of samples studied by NQR method is $12 \times 18 \times 10$ mm^3 which is 28.12% of full coil volume.

References

1. Samila, A. (2017). Peculiarities of using s-simulation for parametric identification of multiplet 115In NQR spectra in InSe. Measurement, 106, 109–115.
2. Michael D Harpen, Analysis of the interaction between an MRI coil and a heterogeneous sample, Phys. Med. Biol. 36 (1991) 133–141.
3. Zhang Xinwang, "A low-power compact nuclear quadrupole resonance (NQR) based explosive detection system," in El. Eng. Theses and Diss., University of Nebraska-Lincoln, 2014.
4. L. E. Kay, L. K. Nicholson, F. Delaglio, A. Bax, D.A. Torchia, Pulse sequences for removal of the effects of cross correlation between dipolar and chemical-shift anisotropy relaxation mechanisms on the measurement of heteronuclear T1 and T2 values in proteins, J. Magn. Reson. 97 (1992) 359–375.
5. Vadim S Grechishkin, Nuclear quadrupole resonance, Phys.-Usp. 2 (1959) 699–718.
6. A. G. Khandozhko, V. A. Khandozhko, A. P. Samila, A pulse coherent NQR spectrometer with effective transient suppression, Eastern- East.-Eur. J. Enterp. Technol. 6 (2013) 21–25.
7. Simulation and Model-Based Design, http://www.mathworks.com/products/simulink/, (accessed Feb 02, 2016).
8. Yu. Bobalo, Z. Hotra, O. Hotra, L. Politans'kyy, A. Samila, Implementation of pulsed radiospectroscopy methods of NQR based on FPGA, Metrol. Meas. Syst. 22 (2015) 363-370.
9. A. Samila, Simulation of magnetic field topology in a saddleshaped coil of nuclear quadrupole resonance spectrometer, Prog. Electromagn. Res. Letters. 56 (2015) 67–73.
10. Samila, A., Khandozhko, V., Politansky, L. (2017). Energy efficiency increase of NQR spectrometer transmitter at pulse resonance excitation with noise sig-

nals. Solid State Nucl. Magn. Reson., 87, 10–17.
11. http://www.mathworks.com/products/simulink/.
12. Andrei Grebennikov, Nathan O. Sokal, Switchmode rf power amplifiers, Elsevier, Burlington, 2007.
13. Hotra, O., Samila, A., Politansky, L. (2018). Synthesis of the configuration structure of digital receiver of NQR radiospectrometer. Przegląd Elektrotechniczny, 94, 58–61.
14. Derome A. E.: Modern NMR Techniques for Chemistry Research. Oxford-Toronto: Pergamon Press., 1992.
15. Samila A.P., Lastivka G.I., Khandozhko V.O., Transference of frequencies of detection and excitation in pulsed spectrometer of nuclear quadrupole resonance, Herald of Khmelnytskyi national university, 5 (2016), No. 241, 231-234.
16. Rannev E., Digital quadrature receiver of time-domain NMR signal, (January-February 2014) https://naukovedenie.ru/PDF/70TVN114.pdf.
17. 12-Bit, 170 MSPS, 1.8 V Analog-to-Digital Converter http://www.analog.com/media/en/technical-documentation/data-sheets/AD9230.pdf (April 2017).
18. Borkowski J. S., Kania D. Ł., Mroczka J., Influence of A/D quantization in an interpolated DFT based system of power control with a small delay, Metrol. Meas. Syst., 21 (2014), No. 3, 423-432.
19. Creating a Digital Synchronous Detector Model. (April 2017). http://electronix.ru/forum/index.php?act=Attach&type=post&id=68838.
20. T. J. Bastow, I. D. Cambell, H. J. Whitfeld, A 69Ga, 115In NQR study of polytypes of GaS, GaSe and InSe, Solid State Commun. 39 (1981) 307–311.
21. V. Khandozhko, N. Raranskii, V. Balazjuk, Z. Kovalyuk and A. Samila, Temperature and baric dependence of nuclear quadruple resonance spectra in indium and gallium monoselenides, Proc. SPIE. 9066 (2013) 90661G-1–7.
22. A. P. Samila, V. O. Khandozhko, Z. D. Kovalyuk, The Nuclear Quadrupole Resonance and Sensory Properties of GaSe and InSe Layered Semiconductors, J. Nano- Electron. Phys. 7 (2015) 03024-1–03024-5.
23. G. I. Lastivka, O. G. Khandozhko, V. O. Khandozhko, Investigation of the multiplicities of nuclear quadrupole resonance spectrums isotopes 113,115In in crystals InSe grown from the melt, East.-Eur. J. Enterp. Technol. 6 (2013) 54–57.
24. K. Z. Rushchanskii, The influence of hydrostatic pressure on the static and dynamic properties of an InSe crystal: A first-principles study, Phys. Solid State. 46 (2004) 179–187.
25. V. S. Grechishkin, Yadernye kvadrupolnye vzaimodeystviya v tverdyh telah [Nuclear quadrupole interactions in solids], Nauka, Moscow, 1973. (in Russian).
26. Schneider, H. and P. Dullenkopf, “Slotted tube resonator: A new NMR probe

head at high observing frequencies," Review of Scientific Instruments, Vol. 48, No. 1, 68–73, 1977.
27. Grechishkin, V. S. and N. Ya. Sinyavskiĭ, "Remote nuclear quadrupole resonance in solids," Physics-Uspekhi (Advances in Physical Sciences), Vol. 36, No. 10, 980–1003, 1993.
28. Brailovskyy, V. V., A. P. Samila, and O. G. Khandozhko, "Topology of high-frequency field strength of microwave spectrometer sensor coil," Visnyk of Lviv Polytechnic National University, No. 646, 46–51, 2009 (in Ukrainian).
29. Hoult, D. I., "The NMR receiver: a description and analysis of design," Progress in NMR Spectroscopy, Vol. 12, No. 1, 41–77, 1978.
30. http://open.ifmo.ru/images/b/b6/144261_book.pdf.
31. Marrocco, B. J. D., D. J. Drost, and F. S. Prato, "An optimized head coil design for MR imaging at 0.15 T," Magnetic Resonance in Medicine, Vol. 5, No. 2, 143–159, 1987.
32. Glukhenkyi, O. I., Yu. M. Goryslavets, and A.V.Tokarevskyi, "Three-dimensional simulation of single-phase electromagnetic stirrer of liquid metal," Technical Electrodynamics, No. 5, 77–84, 2013 (in Russian).
33. http://www.comsol.com/.
34. Glukhenkyi, O. I. and Yu.M. Goryslavets, "Scalar electric and vector magnetic potentials in theory of electromagnetic field," Technical Electrodynamics, No. 2, 7–8, 2012 (in Russian).

Chapter 3
Software modules for configuring programmable logic devices

3.1 Waveform generation for the digital synthesis systems based on embedded hardware

The intensive development of modern technology of information transmission, communication systems of ultrasound frequency range, radio-physical research methods has led to the improvement of existing and the creation of fundamentally new methods and systems for generating and forming signals. Certainly, the fundamental role in this direction development of radio engineering and telecommunication systems has been played by the methods of forming signals based on the algorithms of direct digital synthesis of frequencies. The theoretical foundations of the method have been developing since the 70's of the last century. However, they have only been introduced in practice with the increased level of integration of solid state electronics devices due to the introduction of new technological processes which enabling the manufacture of nanoscale structures. The modern frequency synthesizers, implemented on the basis of digital architecture, provide extremely high non-typical for traditional analog methods of synthesis the speed and accuracy of setting the parameters of generated oscillations, retuning of the frequency of oscillation carrier without rupture of its phase, the possibility of implementing high-speed modulation or manipulation, synthesis of special signals of complex form, the instant numerical control of parameters and others.

The most accurate method of synthesizing a particular signal is to calculate the instantaneous value of its function during a given continuous time interval. It is obvious that in the case of generation of sinusoidal oscillation, it is necessary to calculating the value of the function $\sin(\omega t)$ with maximum accuracy. Since, in real-time systems, computing loads on the central processor are too large, the implementation of such a method is impossible.

In most cases the hardware implementation of digital signal synthesizers has the most commonly used methods non-recursive approximation of sinusoidal oscillation: tabular which based on the recorded in the read only memory (ROM) the discrete samples of sinusoidal function; a hybrid – using of the interpolation methods in finding intermediate values of data read from ROM; method of rotation of coordinates [1–4]. The generalized structure of the DDS is shown in Fig. 3.1 [2]. Modification of this structure, which based on the application of new theoretic-numerical bases and the improved architecture of the summators and phase-amplitudes converters, as well as the improvement of the methods for forming a linear-variable signal of control of the phase of oscillation, are considered in detail in [4–6].

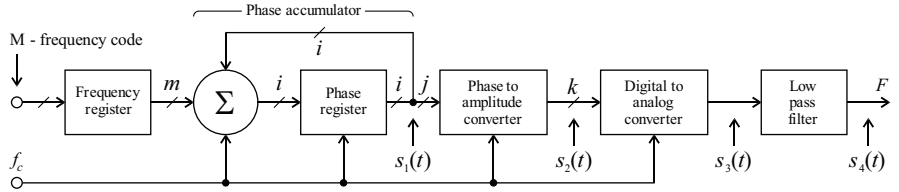

Fig. 3.1 Structure of the Direct Digital Frequency Synthesizer based on the accumulator of phase

One way to avoid computational difficulties in digital signal synthesis is to create a tables N of discrete values of the function $\sin(\omega t)$ describing its behavior in the interval $0 - 2\pi$ or less due to the symmetry properties of the oscillating function. Number of function value samples and the recoding algorithm by themselves does not determine the performance of this method, because, in addition, it will depend on the required accuracy and the stability of the signal formation in the real-time mode and non-linearity of the digital-to-analog conversion process. The efficiency of the table transcoding method is determined by the relationship between the accuracy of the form of the generated signal and the purity of the implementation of its spectrum [7]. The principle of signal transformations is shown in Fig. 3.2.

The frequency of the DDS output signal generated by the numerical method depends on the sampling frequency f_c and increment of phase Δ

$$F = \Delta \frac{f_c}{2^i};\ \Delta \le N/2,$$

where i – bit capacity of transcoding table. Herewith, the minimum sampling step is determined by the dimension of the transcoding table $N = 2^i$ and for one cycle of periodic oscillation is

$$\Delta\varphi = \frac{2\pi}{2^i}.$$

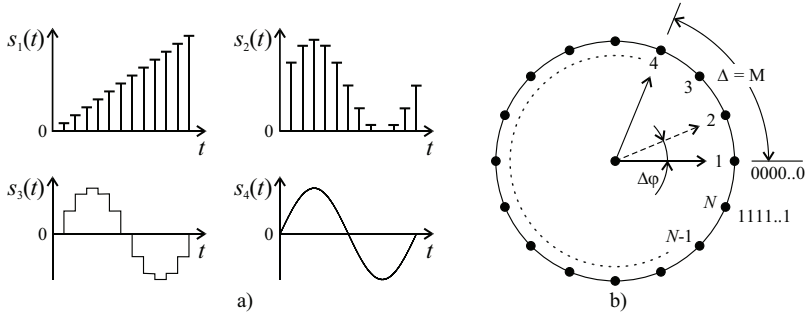

Fig. 3.2 The principle of the direct digital frequency synthesizer: diagrams of signal transformations (a), the phase circle of the digital computing core (b)

If $\Delta = 1$, the value is read in series with the frequency f_c. To generate signals with arbitrary frequencies in the range $f_c/2^i - f_c/2$ (up to the Nyquist frequency), it is necessary that Δ takes not only integer but also fractional values. As a rule, this leads to a significant increase in the total harmonic distortion (THD) of the generated signal, that in addition it depends on the quantization errors, the dimensionality N, and the accuracy of the representation of the recorded in the table samples n [8]. In addition, cutting off the lower order bits of the phase, used to reduce the amount of ROM, leads to irreparable approximation errors.

To implement algorithms for direct digital synthesis and harmonic analysis of the DDS output signal, we compile a table of N samples of the function sinusoidal oscillation. The values of the samples of the vibrational functions sin and CORDIC-sin are calculated in the MATLAB software environment by their mathematical models:

$$s(n) = \begin{cases} \sin\left(\dfrac{2\pi(n-1)}{N}\right); \\ n \in \{1,2,...,N\} \end{cases} s_C(n) = \begin{cases} cordic\sin\left(\left(\dfrac{2\pi(n-1)}{N}\right):(I_C)\right), \\ n \in \{1,2,...,N\} \end{cases}$$

where n – sample number and I_C – the number of iterations of the coordinate rotation digital computer (CORDIC) algorithm, the increase of which increases the accuracy, but leads to an increase in the calculation time.

For the synthesis of a vibration with a lower distortion level, it is necessary to apply the interpolation method to the direct tabular method if fractional Δ [8]. In the case of linear interpolation, the intermediate values of the amplitude of the generated signal were calculated by expression:

$$s(n)_x = mx + \sin\left(\frac{2\pi(n-1)}{N}\right),$$

where $0 < x < 1$ – fractional part of the increment Δ and m – tangent of the angle of inclination of approximation line:

$$m = \frac{s(n) - s(n-1)}{n-(n-1)} = \sin\left(\frac{2\pi n}{N}\right) - \sin\left(\frac{2\pi(n-1)}{N}\right).$$

The analysis of harmonic distortions was carried out according to the method presented in [8], which is based on the determination of the ratio of the energy of harmonics of higher orders to the total energy of all harmonics:

$$K = \sum_{k>1} E_k \Big/ \sum_{k\geq 1} E_k ,$$

where E_k – energy of the spectral component with frequency F_k. Since the oscillations with discrete mapping are approximated, then in its spectrum there are harmonious F_k and combinational $F_{ck} = f_c \pm F_k$ components.

Obtaining accurate and correct results of the calculation of energy relationships is possible when estimating the average value of the THD for the complete cycle of the synthesized oscillation. With a direct tabular method of synthesis, the complete cycle as a function of Δ can consist of several oscillation periods. In the general case, if $\Delta = A/B$, where A and B are prime numbers, then the minimum number of samples of the full cycle $N' = BN$. For example, if $N = 256$ and $\Delta = 2{,}5 = 5/2$, $N' = 2 \cdot 256 = 512$.

The complex Fourier series of discretizated signal represented by a sequence of N samples in the observation interval $T_c = nN$ will look like [9]:

$$s_c(t) = T_\delta \sum_{k=\infty}^{\infty} \dot{C}_k e^{j2\pi k \frac{t}{T_c}},$$

where $k = 0, 1, 2, ..., N\text{-}1$ and complex coefficients of the series are complex amplitudes of the spectral components:

$$\dot{C}_k = \frac{1}{N} \sum_{n=0}^{N-1} s(n) e^{-j2\pi k \frac{n}{N}} .$$

To analyze the amplitude spectrum of a sampled signal, we determine the modules (C_1, C_2, ..., $C_{N/2}$) and the arguments (φ_1, φ_2, ..., $\varphi_{N/2}$) of the complex coefficients of the Fourier series and write the expressions for the instantaneous values of the harmonics [9]:

$$s_1(n) = 2C_1 \cos\left(2\pi \frac{n}{N} + \varphi_1\right);$$

$$s_2(n) = 2C_2 \cos\left(4\pi \frac{n}{N} + \varphi_2\right);$$

.....

$$s_{N/2}(n) = C_{N/2} \cos\left(\kappa 2\pi \frac{n}{N} + \varphi_{N/2}\right).$$

Knowing the total energy of the harmonics of the signal during the cycle BN and the energy oscillation of fundamental frequency, we write the expression for the

calculation of the THD:

$$K = \frac{\sum_{n=0}^{BN-1} s_c(n)^2 - 2BN\left|\dot{C}_1\right|^2}{\sum_{n=0}^{BN-1} s_c(n)^2}.$$

The development of signal form and comparison of algorithms for the synthesis of sequents was carried out by computer parametric identification using the integration of MATLAB and Simulink [10]. The use of the Signal Processing Toolbox ™ and DSP System Toolbox™ modules greatly expand the capabilities of MATLAB Simulink in the field of digital forming of signals, allowed the development and analysis of the generation algorithm and associating by it qualitative signal characteristics even before to implementation on the hardware level (Fig. 3.3).

The study of THD was carried out for signals discretizated by points, linearly interpolated with step Δ and approximated by the CORDIC algorithm (50 iterations). At the same time, $N = 256$ discrete values of the sin function were represented by double precision numbers with a floating point and with samples of 24-bit numbers with a fixed point. With all other conditions being equal, the use of the double-precision table provides a significant reduction in the THD in the case of integer Δ. In the case of fractional Δ the use of linear interpolation provides a reduction in the spread of the absolute values of the THD from 10^{-3} to 10^{-5} (Fig. 3.4).

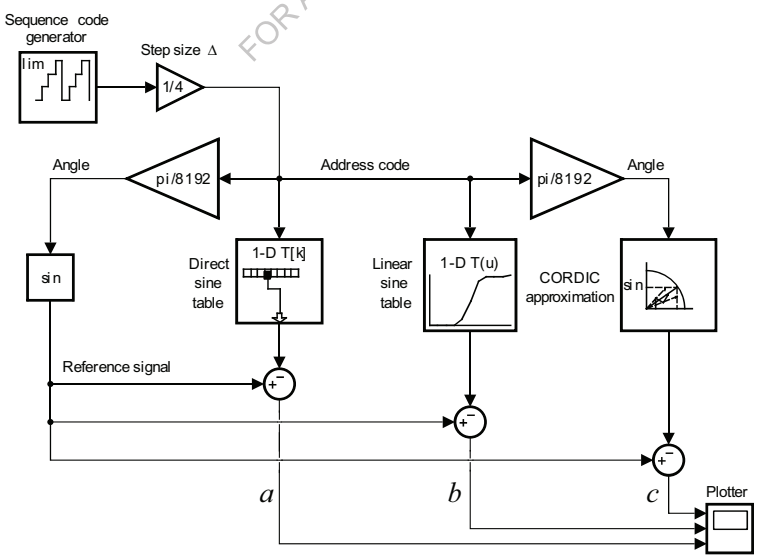

Fig. 3.3 Simulation model for the investigation of harmonic oscillation generation algorithms

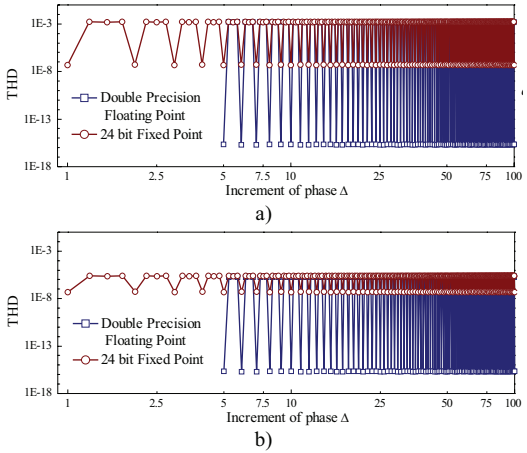

Fig. 3.4 Dependence of the THD on the value of the phase increment: direct synthesis (a), synthesis with linear interpolation (b)

The development of a signal form for DDS with improved spectral purity initiates the selection of the optimal dimension N of the transcoding table. Dependences of the value of the THD on N for a table with a fixed point are shown in Fig. 3.5. When N is changed from 2^5 to 2^{26}, the level of spectral components of higher orders decreases and changes in the interval 2×10^{-2} – 5×10^{-8} (Fig. 3.5a) for fractional Δ and direct sampling by points, and when linear interpolation – in the interval 2×10^{-3} – 5×10^{-8} (Fig. 3.5b). The increase in N improves the spectral purity of the signal, but it causes a significant increase in the volume of the DDS ROM. However, there is an optimal value of $N_{opt.}$, the further growth of which does not significantly affect the change in the value of the THD. As shown by the simulation results, in the simplest version of the implementation of DDS (in case of discretization by points), $N_{opt.} = 2^{25}$, in the synthesis of linear interpolation, $N_{opt.}$ is 2^{13}. The application of interpolation of the values of the sin function represented by discrete readings in the interval 0 – 2π resulted in a decrease in the ROM volume from 768 Mbit up to 192 kbit, and the growth of the THD did not exceed 5 %.

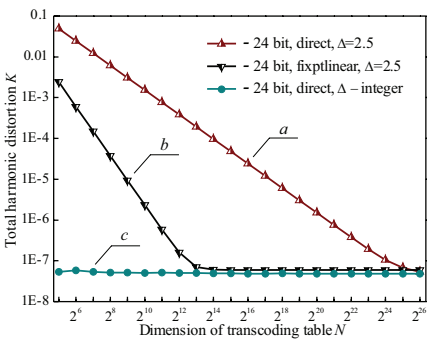

Fig. 3.5 Dependence of THD on the dimension of the transcoding table

The application of modeling also made it possible to visualize the synthesized signal forms and compare them with the reference signal of the sin(x) function by subtracting the synthesized and reference signals. In Fig. 3.6 shows the absolute deviations of the instantaneous values of the signal $s(t)$ synthesized by three different methods at $N_{opt.} = 8192$. As expected from the THD calculation, linear interpolation introduces a smaller error than the discretization by points, but the CORDIC approximation algorithm provides a lower error threshold (Fig. 3.6c) in comparison with linear interpolation. Usually, more accuracy can be achieved by increasing the number of iterations, and hence increasing the computation time.

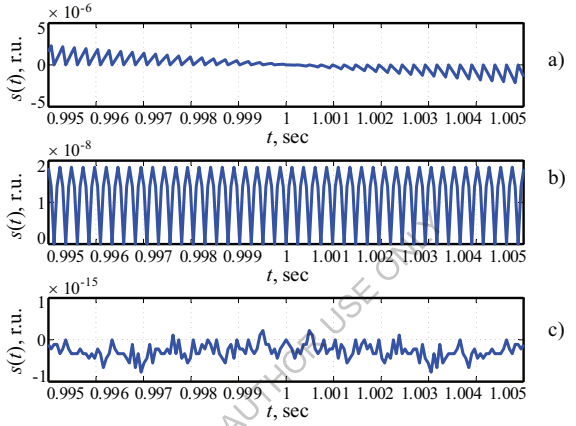

Fig. 3.6 Comparison of the accuracy of the synthesized signals for the: direct method (a), interpolation method (b), CORDIC approximation (c)

3.2 Pulse sequence shaper for radiospectroscopy and relaxation methods in NQR

One of the functional units of NQR Fourier spectrometer is a pulse sequence shaper. It programs the work of pulse keys that assure shaping of NQR excitation pulses. The programmer should form the specified pulse sequences with regulated pulse length and intervals between pulses with preassigned accuracy. If to form a series of pulses and to consecutively rotate a system of nuclear spins by a programmer, it will yield a series of signals that gradually attenuate and in several tens of pulses may not occur. This is caused by the incoherence of spin rotation or “phase memory loss” due to different microsystem interactions [11].

The majority of excitation pulse shapers for nuclear resonance and relaxation studies proposed by developers have a number of disadvantages. In particular, most of them are made as PC expansion cards and require the development of dedicated software which imposes limitations on their mobility [12]. Moreover, by virtue of

their wide functionality and, accordingly, high cost, such devices are not affordable for the majority of research laboratories.

The use of FPGA assured shaping of NQR excitation pulses with preassigned accuracy and possible change in the configuration of sequence parameters [13].

The existing pulsed spectroscopy and relaxometry methods of NQR are conventionally divided into incoherent and coherent systems that are mainly noted for the presence of phase synchronization of excitation pulses with carrier frequency oscillations (Fig. 3.7). The elaborated oscillation packages of carrier frequency (Fig. 3.7d) are probing pulses whose leading edges are defined by trigger pulses (Fig. 3.7b) and are tied to oscillation phase of carrier frequency. In this way the coherence of spectrometer operation is provided.

For performing the relaxation studies both coherence of shaped pulses and the accuracy of determination of 90º-th and 180º-th pulses duration and pauses in the sequence are important [14]. Since NQR signal frequency for a certain compound is a function of electric field gradient value, the exact value of resonance frequency is unknown. That is, basic frequency must be varied and, accordingly, the duration of 90º-th and 180º-th pulses must be selected on a case-by-case basis. It is difficult to be achieved using the methods considered in [15], as phase binding of probing pulses to carrier oscillation causes time error which is accumulated with increasing the number of pulses in the sequence (Fig. 3.7d).

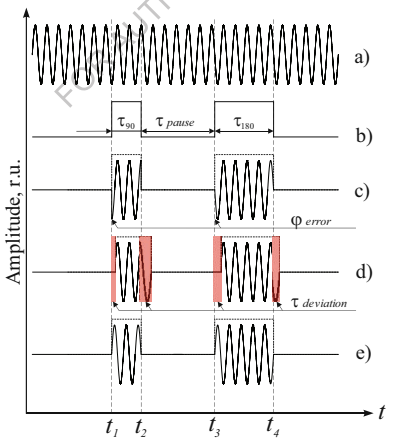

Fig. 3.7 Time diagrams of shaping NQR excitation pulses: carrier frequency oscillations (a); probing pulse envelope (b); probing pulse at – incoherent shaping (c), coherent shaping (d), use of controlled synthesizer (e)

The range of application of NQR methods requires the use of shapers with the possibility of setting and change of many pulse parameters in the sequences, which complicates implementation and increases the cost of NQR equipment. The advent of

reconfigurable FPGA facilitates this task and makes possible implementation of pulsed methods of NQR on their basis, since the use of FPGA allows creation of not only carrier oscillations with unvarying frequency and initial phase, but also a flexible system of shaping coherent excitation pulses of NQR signals.

Pulse sequence shaper is a hardware-software solution. Program algorithm was designed by methods of simulation and development of very large-scale integrated circuits and systems on a chip by Altera Corporation [16]. Pulse sequence shaping diagram on the basis of FPGA is depicted in Fig. 3.8.

The distinguishing feature of this product is its implementation with the use of a multi-functional program controlled frequency synthesizer with the possibility of fast frequency and phase manipulations (Fig. 3.9). Formation of carrier high-frequency oscillations is based on DDS that have widespread application in radio-electronic devices and telecommunication systems [17]. The synthesizer is based on a 48-bit phase accumulator "altaccumulate0" which forms code sequence of signal instantaneous phase that varies linearly. Modules "phase_mux", "phase_adder" and "phase_reg" serve to implement phase manipulation of carrier frequency of DDS output signal.

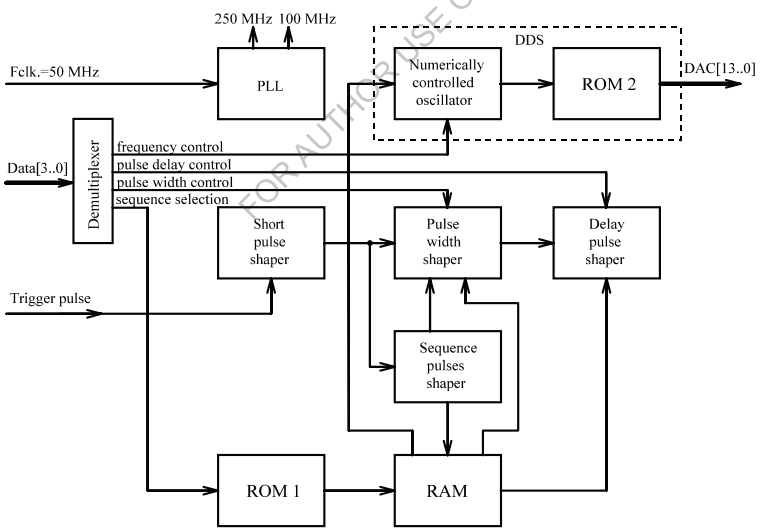

Fig. 3.8 Pulse sequence shaping diagram based on controlled synthesizer

A phase locked loop (PLL) module is a programmable system that generates oscillations with the frequencies $f_{clk1} = 250$ MHz and $f_{clk2} = 100$ MHz with an external clock generator operated at a frequency of 50 MHz. Frequency f_{clk1} is used as a reference frequency for digital frequency synthesizer, and f_{clk2} is used for the operation of pulse former with minimum pulse duration $\tau = 100$ nsec. Readings of

frequency synthesizer output signal are written in the table “DDS_rom”.

Pulse sequence shaping circuit in program editor ALTERA Quartus Web Edition software corresponding to the designed algorithm is presented in Fig. 3.10.

Multiplier “mult 1” enables the introduction of input frequency code immediately in the form of a numerical constant corresponding to anticipated numerical value of generated frequency. It multiplies the input code of frequency K_1 by constant $K_2 = 11258999$ that set the code $K = K_1K_2$ of synthesizer frequency step $\Delta f = 10$ Hz.

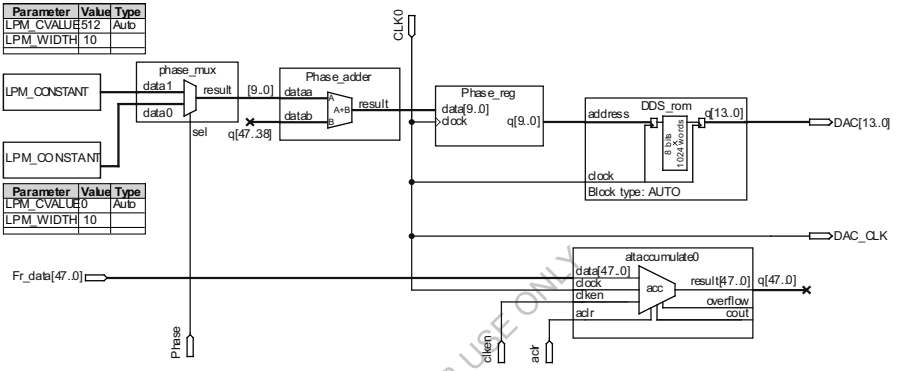

Fig. 3.9 Implementation of Direct Digital Synthesizer in ALTERA Quartus software

Dependence of signal frequency f_{out} at the output of numerically controlled generator on reference clock frequency f_{clk}, capacity of phase accumulator M and frequency code K is determined as follows [18]:

$$f_{out} = \frac{K \times f_{clk}}{2^M}.$$

In so doing, frequency step does not depend on its value and is equal to:

$$\Delta f_{out} = \frac{f_{clk}}{2^M}.$$

In our case the operating frequency of phase accumulator with a capacity $M = 48$ bit is equal to $f_{clk1} = 250$ MHz. Thus, the frequency step will be $\Delta f_{out} \approx 1\times10^{-6}$ Hz. So, to shape a signal with frequency f_{out} to synthesizer input “Fr_data[47..0]” one should feed a 24-bit frequency code determined by the following expression:

$$K_1 = \frac{2^M f_{out}}{f_{clk} K_2} = 25\times10^6 \frac{f_{out}}{f_{clk}}.$$

Sequence generation starts synchronously with input gating pulse. The data on the frequency of carrier oscillation, duration of 90º-th pulse, pulse spacing and sequence type comes from external control unit along the Data bus [3..0] (Fig. 3.8). The duration of 90º-th pulse is set in the range of 0.1 – 20 μsec with a step of 0.1 μsec. Pulse spacing is controlled in the range of 0.1 μsec – 1 sec. All the other time intervals, for instance, in the Carr-Purcell sequence [14], the duration of 180º-th pulses and their spacing are set automatically, according to selected program recorded in ROM 1. The number of pulses in a series is assigned within 1 –30. Information on the parameters of this or other sequence through buffered random access memory (RAM) comes to a series of actuation devices, namely program-controlled generator, pulse and pause duration formers.

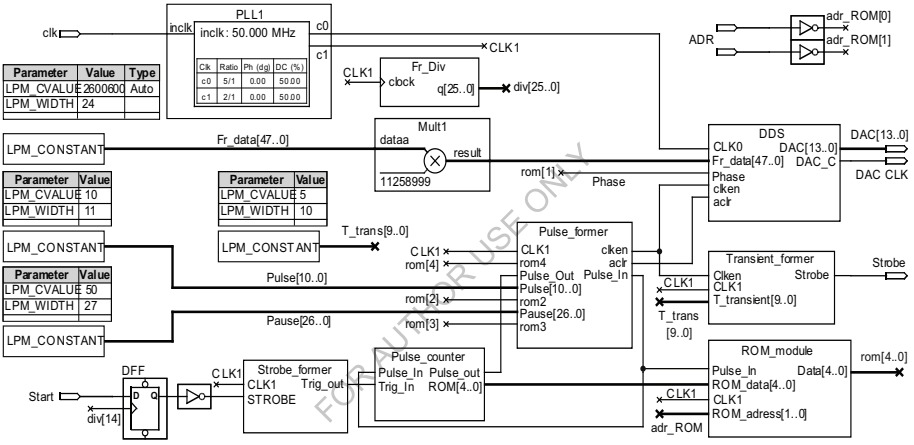

Fig. 3.10 Implementation of pulse sequence shaping circuit in ALTERA Quartus software

The structure of file fragment written in ROM 1 (Fig. 3.11) shows arrangement of information bits in the words. The first bit is responsible for the presence of pulse in the sequence. Next bits control pulse duration, pause duration and enable phase shift. These bits define the rules of the 90º-th and 180º-th pulses. If bits 1 and 2 are set to "0", the duration of the pulses and pauses are set by the external control unit. If bits 1 and 2 are set to "1", the duration of the pulses and pauses is twice longer.

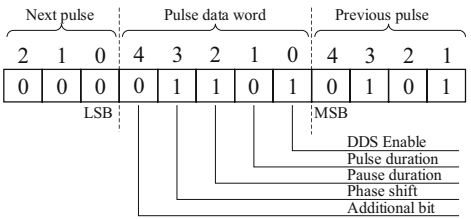

Fig. 3.11 Memory write structure ROM 1

Simulation of designed algorithm operation was done by means of Simulator Tool from ALTERA. Simulation results in Fig. 3.12 show that the values of basic frequency, initial phases, pulse duration and pause duration in a sequence correspond to those prerecorded in ROM 1. The volume of used FPGA EP1C6T144C8N hardware resources was the following: Total logic elements – 1435 (24 %), Total memory bits – 50112 (54 %), Total PLL – 1 (50 %).

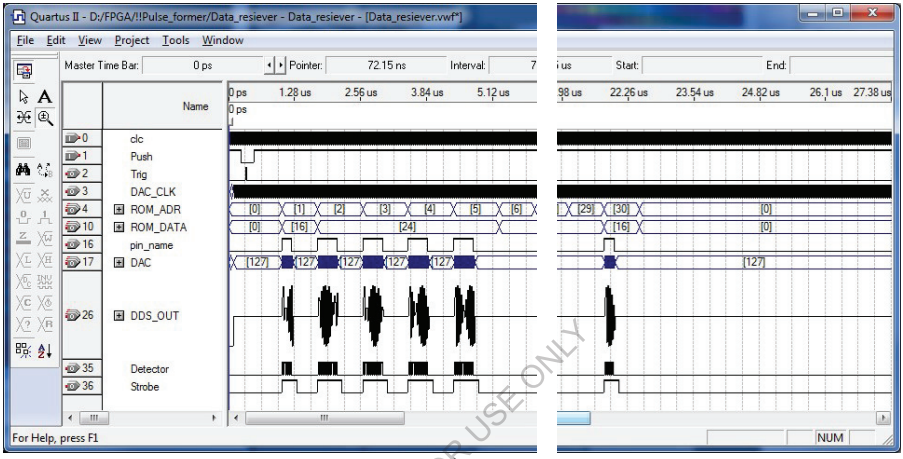

a)

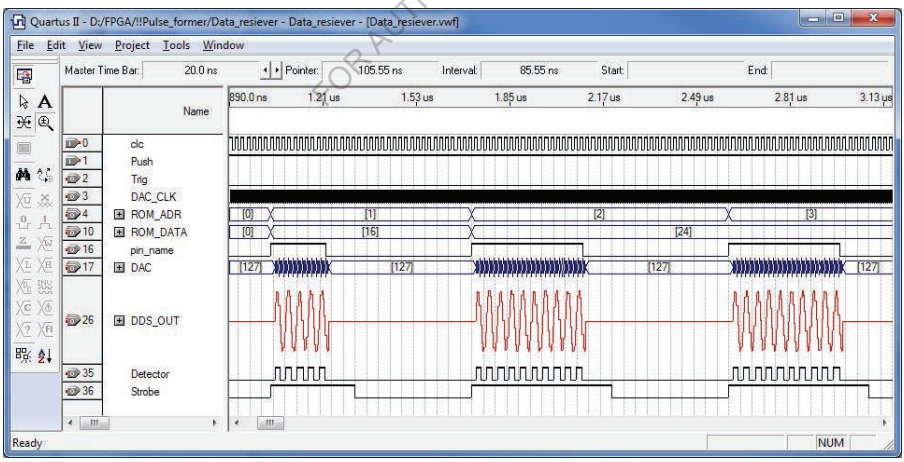

b)

Fig. 3.12 Simulation of the operation of the device of a full cycle of forming a thirty pulse sequence (a): 0-50 MHz clock pulses, 1 - start pulse, 2 - sync pulse, 3 - 250 MHz clock pulses, 4 - memory address bus, 10 - memory address bus, 16 - DDS synthesizer enable pulses, 17 - data bus on digital to analog converter (DAC), 26 - simulated analog signal, 35 - synchronous detector control pulses, 36 - gating pulses. Fragment (b) visualizes 3-pulse diagrams

The designed algorithm also provides for shaping of a reference signal for the operation of external synchronous detector (Fig. 3.12.35) and gating pulses for control of radio spectrometer reception path (Fig. 3.12.36). The work of the shaper allows for the possibility of setting additional time at the end of each shaped probing pulse for the suppression of receiving coil “ringing” after the action of probing excitation pulse [19].

3.3 Synthesis of SDR configuration structure

The concept of proposed model realization on the basis of digital signal processing (DSP) libraries System Toolbox and FDATool makes possible its efficient implementation on the basis of field-programmable gate arrays. In this case, the FPGA of Intel (Altera) or Xilinx are effective, since computer aided design (CAD) systems of their configuration structures are closely integrated with MATLAB [20].

The SDR configuration structure of spectrometer receiver developed in Altera Quartus II Web Edition Software for FPGA EP4CE15E22C8 is shown in Fig. 3.13 [21].

The structure of pulse former proposed in [3] already has a DDS, the output signal of which will be used as the reference for spectrum transfer. In order to implement the digital quadrature detection, another transcoding table is added to the DDS configuration structure for the function $y = \cos(x)$. The reference signals are sent to the inputs of the "mult1", where they are multiplied with the information signal. Since ADC data and DDS reference signals are 12-bit, we obtain a 24-bit number as a result of multiplication. The operation of multiplication will lead to transferring of signal spectrum to LF. In this case, further work with the digital signal, which is sampled by 170 million samples per second, is no longer appropriate and it is necessary to carry out resampling to a lower frequency. Before this operation, LPF is required. In the SDR configuration structure (Fig. 3.13), a CIC filter is used that provides a 10-fold reduction of the sampling rate.

After the CIC filter, there is an FIR filter, which compensates the sloping frequency response. The FIR filter coefficients calculated in MATLAB FDATool (Fig. 3.14).

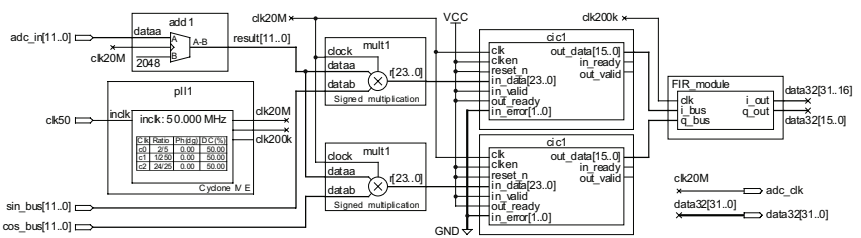

Fig. 3.13 SDR configuration structure in Altera Quartus II Web Edition Software

The numerical values of the coefficients are given in the Table 3.1. The module of the parallel binary adder "add1" serves to shift constant component of the data coming from the ADC output by the value equal to half the maximum amplitude of the information signal. The "pll1" module generates reference frequency signals: 170 MHz – for ADC, multipliers, adder and CIC filters; 17 MHz – for FIR filters operation.

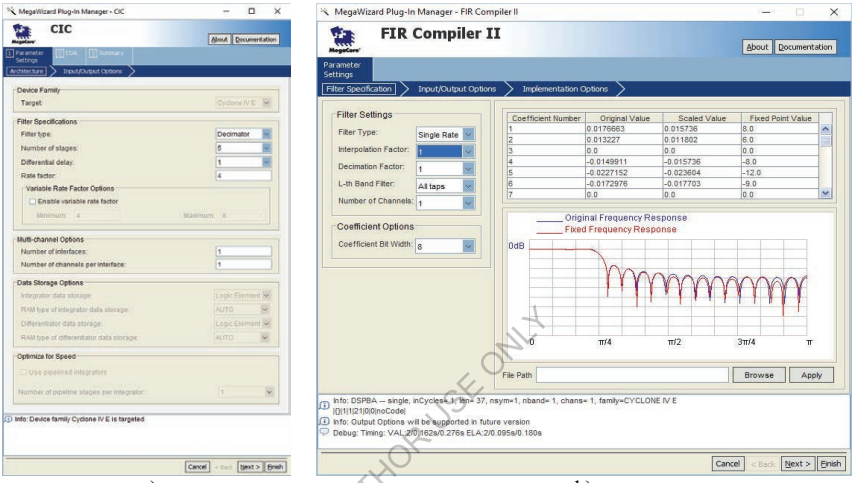

a) b)

Fig. 3.14 Using Altera Quartus II Megafunction Wizard to configure digital filters of CIC (a) and FIR (b) types

Table 3.1 FIR coefficients

No.	Value	No.	Value	No.	Value	No.	Value	No.	Value	No.	Value
1	-53	13	277	25	-1293	37	4770	49	18379	61	-3042
2	-102	14	439	26	-1601	38	5173	50	5700	62	-1083
3	-92	15	333	27	-877	39	2150	51	-4611	63	1127
4	-20	16	-42	28	604	40	-3260	52	-9398	64	2312
5	79	17	-490	29	1989	41	-8232	53	-8232	65	1989
6	150	18	-709	30	2312	42	-9398	54	-3260	66	604
7	133	19	-485	31	1127	43	-4611	55	2150	67	-877
8	17	20	136	32	-1083	44	5700	56	5173	68	-1601
9	-148	21	814	33	-3042	45	18379	57	4770	69	-1293
10	-257	22	1086	34	-3369	46	28765	58	1868	70	-311
11	-214	23	666	35	-1477	47	32767	59	-1477	71	666
12	-2	24	-311	36	1868	48	28765	60	-3369	72	1086

3.4 Application of a statically configured FPGA in the digital control system of the NQR radio spectrometer

In order to provide operative control over the course of the experiment and the choice of its initial conditions, a portable NQR radio spectrometer requires the presence of a flexible control system [22, 23]. Among the main functional tasks of such a system are the following: the presence of a storage device for recording data on the basic settings and operating modes of the spectrometer, the ability to enter data through the user interface, convenient and at the same time informative settings control menu, the presence of a graphical interface to display status information and operating modes of the spectrometer, communication with the execution modules of the spectrometer through the digital data bus [24]. For the development, a low-cost platform Altera NIOS-EVALKIT-1C12 was selected, the important advantage of which is the availability of hardware necessary for implementation of the above functional tasks. The platform comprises EP1C12F324 FPGA of the Cyclone family, a 16 MB synchronous dynamic RAM memory chip, a 8 MB Flash-ROM chip, a 24 MHz clock generator, 48 I/O ports, 3.3 V and 5.0 V power supplies [25].

The algorithm of the program part of the proposed system is depicted in Fig. 3.15. The initial step is initializing I/O devices, polling the temperature sensor, reading the settings from the external flash memory, and subsequent entering the output data into registers. In this case, the device provides display of the main parameters and their output to the interface bus. In general, the algorithm developed allows the setting of a direct digital frequency synthesis synthesizer, the choice of the type of the sequence of NQR excitation signals, the setting of the parameters of the high-frequency spectrometer and its control system [22, 24]. Upon completion of the settings, pressing the menu button repeatedly checks the implementation of the data storage condition. When it is executed, new data is recorded in the nonvolatile memory and transmitted to the interface bus of the spectrometer. The display shows the home screen.

For the implementation of the pre-assigned algorithm a finite state machine has been synthesized, the alphabet of output sequences of which $Y = \{y_1, y_2[4:0], y_3\}$ is determined by a plurality of machine states $S = \{s_0, s_1, s_2, ..., s_{32}\}$, and a plurality of input characters is given by alphabet $X = \{x_1, x_2, ..., x_{5M}\}$ (Table 3.2). The initial state is $s_0 \in S$. When processing input characters, the machine first moves from the state s_0 to $s_1 = f(s_0, x_1)$. The process continues until the state $s_{32} = f(s_2 \vee s_3 \vee s_4 \vee s_5 \vee s_6, x_{10})$ is reached. This sequence of transitions forms the source alphabet. The character $y_1 = g(s_0)$ corresponds to transition from s_0 to s_1. A plurality of characters $y_2[4:0] \in Y$ corresponds to transitions between s_1 and s_{31}. The character $y_{32} = g(s_2 \vee s_3 \vee s_4 \vee s_5 \vee s_6)$ corresponds to transition of machine to state s_{32}.

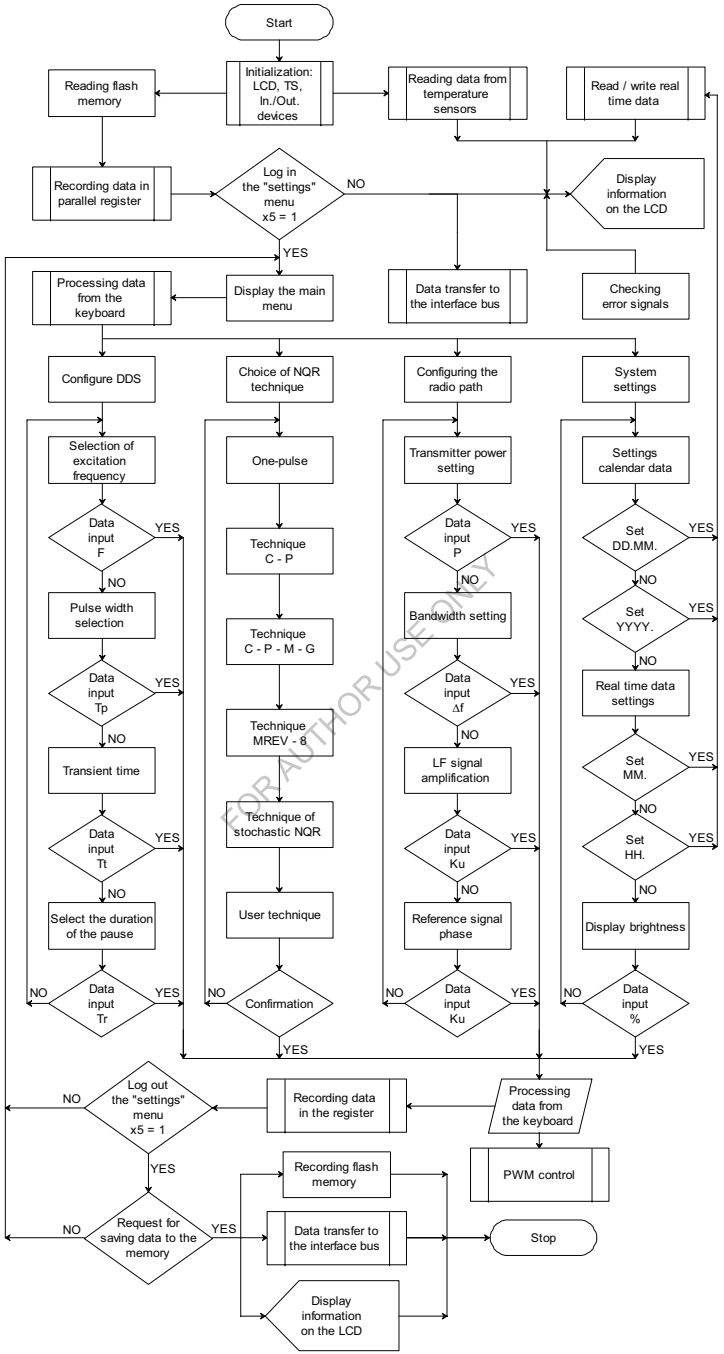

Fig. 3.15 The algorithm of FPGA program

Table 3.2 Input and output data of finite state machine

Input data	Input destination xN	State of the machine	State description sN	Output data
x1	Initialization timer	s1	Initialization	y1 = 1
		s2	Start the technique №1	y2[4:0] = 'b00000
x2	Loading methods	s3	Start the technique №2	y2[4:0] = 'b00001
		s4	Start the technique №3	y2[4:0] = 'b00010
x3	Save timer	s5	Start the technique №4	y2[4:0] = 'b00011
		s6	Start the technique №5	y2[4:0] = 'b00100
x4	Exit timer	s7	Setup the synthesizer	y2[4:0] = 'b00101
		s8	Choice of technique	y2[4:0] = 'b00110
x5	The command "enter menu"	s9	Setup the RF path	y2[4:0] = 'b00111
		s10	System settings	y2[4:0] = 'b01000
x6	The command "up"	s11	Selection of excitation frequency	y2[4:0] = 'b01001
		s12	Pulse width selection	y2[4:0] = 'b01010
x7	The command "down"	s13	Transient time	y2[4:0] = 'b01011
		s14	Select the duration of the pause	y2[4:0] = 'b01100
x8	The command "confirmation"	s15	Single-pulse technique	y2[4:0] = 'b01101
		s16	Technique C - P	y2[4:0] = 'b01110
x9	The command "deviation"	s17	Technique C - P - M - G	y2[4:0] = 'b01111
		s18	Technique MREV - 8	y2[4:0] = 'b10000
x10	Sleep timer	s19	Technique of stochastic NQR	y2[4:0] = 'b10001
		s20	User technique	y2[4:0] = 'b10010
x11	Exit sleep mode	s21	Excitation intensity	y2[4:0] = 'b10011
		s22	Bandwidth	y2[4:0] = 'b10100
x1M	Activate the technique №1	s23	LF signal amplification	y2[4:0] = 'b10101
		s24	Reference signal phase	y2[4:0] = 'b10110
x2M	Activate the technique №2	s25	Setting the system date	y2[4:0] = 'b10111
		s26	Setting the system time	y2[4:0] = 'b11000
x3M	Activate the technique №3	s27	Display brightness	y2[4:0] = 'b11001
		s28	Duration of sleep mode	y2[4:0] = 'b11010
x4M	Activate the technique №4	s29	Request to save settings	y2[4:0] = 'b11011
		s30	Do not save	y2[4:0] = 'b11100
x5M	Activate the technique №5	s31	Save	y2[4:0] = 'b11101
		s32	Sleep mode, screen saver	y3 = 1

Fig. 3.16 in the form of oriented multigraph shows a fragment of diagram of machine states which corresponds to algorithm in Fig. 3.15 (transient states are not signed). Transition functions f: $S \times X \rightarrow S$ and output functions g: $S \rightarrow Y$ of finite state machine are written in very high speed integrated circuit hardware description language (VHDL).

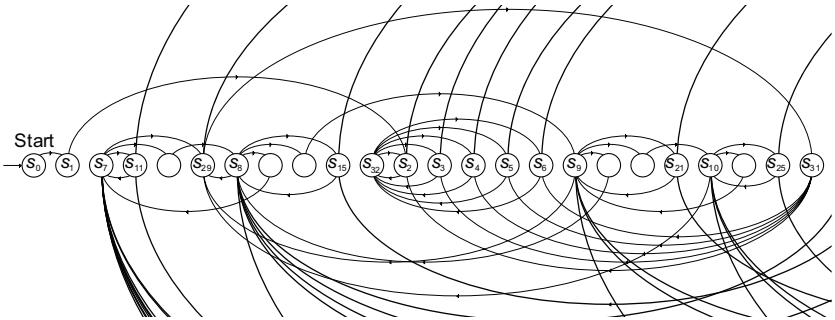

Fig. 3.16 Diagram of states of the synthesized finite state machine

Configuration structure of FPGA (Fig. 3.17) was developed in the environment for design of projects in Altera CAD – Quartus II Web Edition, using the method of complex graphic-syntactic programming. In this structure, the main module “core”, based on the finite state machine and additional submodules of combinational (lpm_mult, lpm_decode, lpm_compare, lpm_mux) and sequential (dff, latch, lpm_ff, lpm_counter) logic, in conformity with the output data from the keyboard initialization module “key_ini”, ensures performance of functions set by program algorithm and output of control signals: Data_State[4..0]; Init_Enable; Logo/Main; Main/Screen; Digits (Pulse1-5, DDS, RF, SYS), necessary for operation of other structure modules. Synchronous dynamic memory "Data_Memory" is necessary for storing numerical data entered from the keyboard for the purpose of their subsequent redirection by the module "BUS_Controller" to the spectrometer execution units [3, 24]. The data registers designed to store the spectrometer parameter settings are implemented on the basis of the LPM_DFF megafunction library (parallel register).

Recording data in registers is done according to the code on the address bus. Thus, the system of 36 separate 4-bit LPM_DFF modules with a total memory capacity of 148 bits allows you to save the settings of a number of parameters: DDS frequency, duration of the excitation pulse and transient process, pause between pulses, sequence type, transmitter power, transmission and amplification of NQR spectrometer radio channel. The synchronization is provided by the FPGA-integrated PLL system and dividers “div”, forming the frequencies: 24 MHz – for the core; 100 MHz – for graphical subsystem; 6.25 MHz – for display. The output of the image on the liquid crystal display (LCD) is provided by the graphical subsystem of the configuration structure, the main principle of which is laid down in the synthesis of sign-symbol graphics - fonts and vector dynamic images and multiplexing of these data with elements of the background graphics (Fig. 3.18). The module "Disp_Sync_Gen" generates pulses of raster synchronization, and "Graphics" - provides reading of 16-bit background graphics data from an external Flash-ROM AM29LV640MH of 64 Mbps (Fig. 3.17).

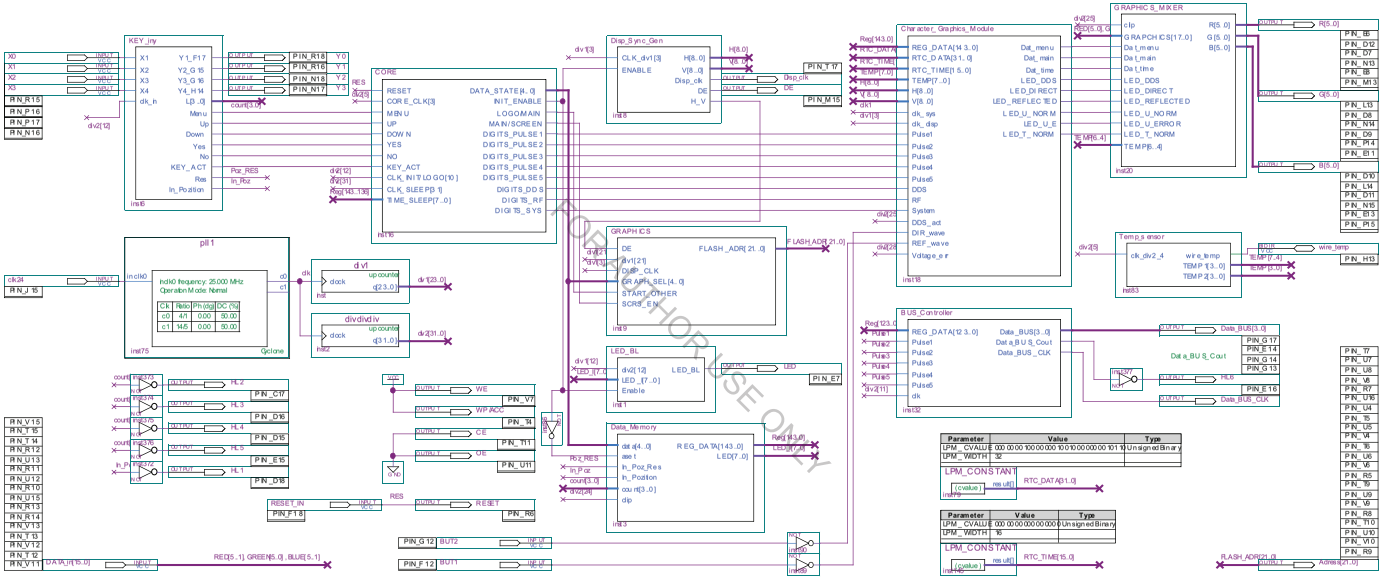

Fig. 3.17 Configuration structure of the FPGA in the window of the Quartus II

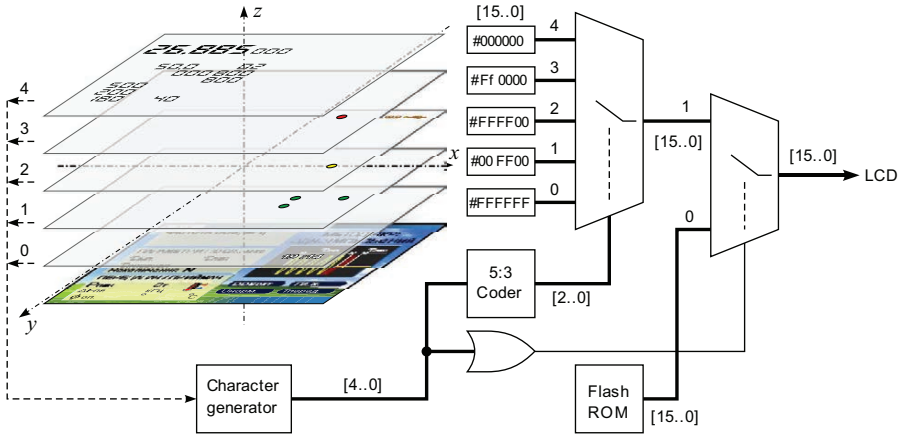

Fig. 3.18 The principle of multiplexing graphic data

The structured segment of Character_Graphics_Module character generator module, corresponding to one visible character on the LCD screen, is shown in Fig. 3.19. The main element of this module is the M4K-ROM "ROM_Big_mod", of volume 109 kbit, containing graphical representation data of 10 digits from 0 to 9. Sequential paging of graphic symbols is provided by feeding a 11-bit code to the address memory input. The addressing of individual pages is ensured by adding a multiplexed numeric constant to the original address of the first character, which varies when the data on the DATA [3..0] bus is changed. For fonts with different graphical representations, their files have been generated like *.hex. The initialization of the TD035STEB2 RCI controller and the graphics output through the sixteen-bit data bus is provided by the following operations [26]:

- supply of a clock signal with a frequency of 6.5 MHz;
- supply of synchronization pulse in a line of duration 2 μs to DE line;
- output of the color data of the first pixel of the first line to the bus [15..0];
- output of the color data of the 240-*i*-th pixel of the first line to the bus [15..0];
- output of the color data of 240-th pixel of the first line to the bus [15..0];
- supply of synchronization pulse in a frame of duration 12 μs to DE line;
- output of the color data of the first pixel of the second line to bus [15..0];
- output of the color data of the 240-*i*-th pixel of the 320-*k*-th line to the bus [15..0];
- output of the color data of the 240-th pixel of the 320-th line to the bus [15..0];
- setting the lines of bus [15..0] into high impedance state.

Reading the temperature data starts with the initialization routine, which generates a reset pulse of 30 μs duration and takes the presence pulses of 60 – 240 μs duration.

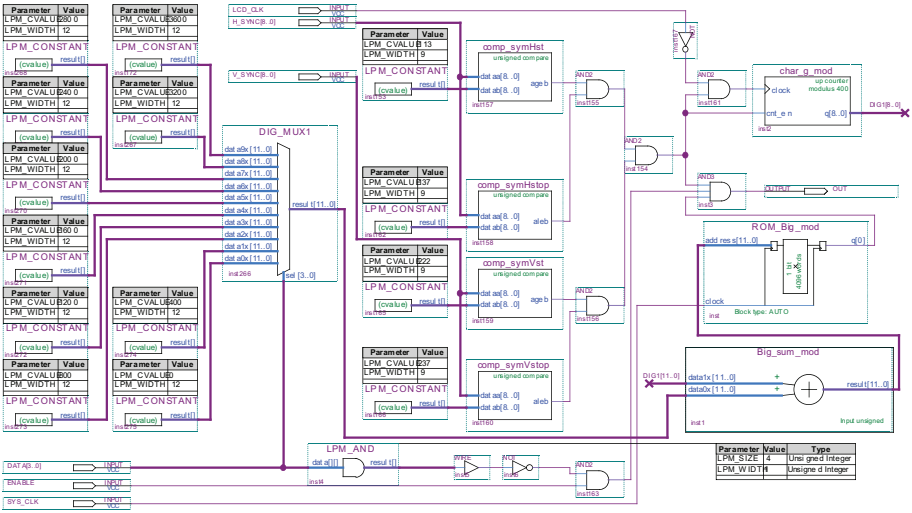

Fig. 3.19 Structured segment of character generator module in the window of Quartus II

Other procedures and functions of configuration structure were implemented by Megafunction means using the library of parameterized modules (LPM). Project compilation in Quartus II Web Edition has shown that the developed configuration structure used 3699 (31 %) base logic units and 160 kbit (68 %) of FPGA memory.

3.5 Conclusions

A parametric estimation of the efficiency of using the main methods of generating a harmonious sinusoidal oscillation for the synthesis of digital signals based on embedded hardware systems is carried out. From the results of studies of non-linear distortions and comparison of the accuracy of the forms of signal generated by points discretization, linear interpolation, and the use of the CORDIC approximation algorithm, we can conclude that:

1. The advantages of synthesizers based on direct tabular synthesis with linear interpolation of the argument of the oscillatory function for fractional values of phase increment is a simple hardware implementation and a low level of nonlinear distortion. The disadvantage is the distortion of the shape of the generated signal;

2. The advantages of synthesizers with the hardware computing core CORDIC as a converter phase-amplitude is the lowest level of nonlinear distortion and increase in the accuracy of the signal form due to the increase in the number of iterations. The disadvantage is the growth of computational loads and calculation time with increasing number of iterations.

The CORDIC algorithm minimizes the need for the multipliers used, so it can be

used if they are little effective or generally absent in the existing hardware.

A multi-functional programmer of pulse sequences for NQR Fourier spectrometer has been developed on the basis of FPGA. The experimental test results have shown that the device assures shaping of pulsed sequences necessary for the pursuance of relaxation research in the frequency range of 1 – 50 MHz.

The proposed programmer allows shaping of one, two and multi-pulsed sequences which enables the experiments on measuring relaxation times using the methods of Hahn, Carr-Purcell, Meiboom-Gill, et al. Owing to a wide range of change in pulse lengths and the possibility of shaping various sequences, this programmer assures a change in parameters T_1, T_2, T_{2*}.

Digital shaping of pulse sequences implemented in the proposed product assures high stability and accuracy of all temporal relations. The programmer guarantees phase binding of high-frequency filling of video pulses to pulse fronts.

The structure of the digital quadrature receiver of nuclear quadruple resonance signals based on the field-programmable gate array EP4CE15E22C8 eventually can be used over time in the implementation of portable systems for the registration of double NQR-NMR and NQR-NQR resonances, multidimensional NQR spectroscopy, NQR tomography of semiconductor solid state devices.

The digital multifunctional control system for pulsed NQR Fourier radio spectrometer of laboratory type is developed, the main hardware-software methods of which are realized using FPGA with a static configuration EP1C12F324. The basis for the algorithm of IC configuration is the synthesized finite state machine, the alphabet of the output sequences Y of which is determined by the plurality of machine states S, and the plurality of input characters is given by the alphabet X. Transition functions f: $S\times X\rightarrow S$ and output functions g: $S\rightarrow Y$ of finite state machine are described in VHDL language.

References

1. Samila Andriy, Lastivka Galina, Politansky Leonid, Kazemirskiy Taras. Waveform generation for the digital synthesis systems based on embedded hardware. “Modern problems of radio engineering, telecommunications, and computer science” : The International Conference TCSET’2018, Ukraine, Lviv-Slavske, february 20–24 2018. Lviv, 2018. P. 831–834.
2. Vankka J. Direct Digital Synthesizers: Theory, Design and Applications. Helsinki: Helsinki University of Technology, 2000.
3. Yu. Bobalo, Z. Hotra, O. Hotra, L. Politans’kyy, A. Samila, "Implementation of pulsed radiospectroscopy methods of NQR based on FPGA," Metrol. Meas. Syst., vol. 22, Issue 3, pp.363-370, 2015.
4. Polikarovs'kih O.I., Shevchuk O.I., "Metody formuvannya synusoyidalnyh

syhnaliv u tsyfrovyh syntezatorah sitky chastot," Vimirjuval'na ta obchisljuval'na tehnika v tehnologichnih procesah, vol. 2, pp.100–105, 2009.
5. Polikarovs'kih O.I., "Zastosuvannya novoho teoretyko-chyslovoho bazysu dlya pobudovy vysokoshvydkisnyh obchyslyuvalnyh syntezatoriv chastoty (DDS)," Vimirjuval'na ta obchisljuval'na tehnika v tehnologichnih procesah, vol. 1, pp.20–26, 2013.
6. Polikarovs'kih O.I., Mishan V.V., "Metody pidvyschennya yakosti spektralnyh harakterystyk vysokoshvydkisnyh obchyslyuvalnyh syntezatoriv chastoty (DDS)," Visnik Hmel'nic'kogo nacional'nogo universitetu, Technical sciecnes, vol. 5, pp.208–211, 2013.
7. Mandal A., Mishra R., "FPGA implementation of pipelined CORDIC for digital demodulation in FMCW radar," Infocommunications J., vol. 5, Issue 2, pp.17–23, 2013.
8. http://jcoppens.com/univ/data/pdf/dsp/apr1.pdf
9. Mandziy B.A., Zhelyak R.I. Osnovy teoryi syhnaliv: pidruchnyk. Lviv: Vydavnychyy dim «Initsiatyva», 2008.
10. https://www.mathworks.com/help/simulink/examples/digital-waveform-generation-approximating-a-sine-wave.html.
11. Shen, Jie, Liu, Ying, Li, Jianqi, Li, Gengying. (2005). A powerful graphical pulse sequence programming tool for magnetic resonance imaging. Magnetic Resonance Materials in Physics, Biology and Medicine, 18(6), 332–342.
12. http://www.spincore.com/CD/RadioProcessor-G/RadioProcessor-G_Manual.pdf. (2014 July).
13. Grzelak, S., Kowalski, M., Czoków, J., & Zielinski, M. (2014). High resolution time-interval measurement systems applied to flow measurement. Metrology and Measurement Systems, 21(1), 77-84.
14. Kay, L. E., Nicholson, L. K, Delaglio, F., Bax, A., Torchia, D. A. (1992). Pulse sequences for removal of the effects of cross correlation between dipolar and chemical-shift anisotropy relaxation mechanisms on the measurement of heteronuclear T1 and T2 values in proteins. Journal of Magnetic Resonance, 97(2), 359–375.
15. Khandozhko, A. G., Khandozhko, V. A., Samila, A. P. (2013). A pulse coherent NQR spectrometer with effective transient suppression. Eastern-European Journal of Enterprise Technologies, 6/12(66), 21–25.
16. http://www.altera.com/products/software/quartus-ii/subscription-edition/qts-se-index.html. (July 2014).
17. Bopche, M. A., Deshmukh, A.Y. (2011). FPGA based direct digital synthesis function generator. International Journal of VLSI and Signal Processing Applications, 1(2), 8–14.

18. Ridiko, L. I. DDS: Direct Digital Synthesizers. http://www.digit-el.com/files/articles/ dds.pdf. (2014 July).
19. Rudakov, T. N., Shpilevoi, A. A. (1997). An Input Device for the Receiving Channel of a Nuclear Quadrupole Resonance Spectrometer. Instruments and Experimental Techniques, 40(2), 215–216.
20. Hotra O., Samila A., Politansky L. Synthesis of the configuration structure of digital receiver of NQR radiospectrometer. Przegląd Elektrotechniczny. 2018. Vol. 94. No. 7. P. 58–61.
21. Cyclone IV Device Datasheet. CYIV-53001-2.0. https://www.altera.com/content/dam/altera-www/global/en_US/pdfs/literature/hb/cyclone-iv/cyiv-53001.pdf (July 2017)
22. Samila A., Hotra O., Politansky L., Khrapko S. Application of a statically configured FPGA in the digital control system of the NQR radio spectrometer. Proceedings of SPIE 10808 : Photonics Applications in Astronomy, Communications, Industry, and High-Energy Physics Experiments, Poland, Wilga, 2018. Wilga, 2018. P. 108081K-1–9.
23. Buzug, T. M., Kaufmann, S., Marquina-Sanchez, R., Ryschka, M., Sattel, T. F., "A Control Unit for a Magnetic Particle Spectrometer," Springer Proceedings in Physics Magnetic Particle Imaging 140, 309-312 (2012).
24. Samila, Andriy, Khandozhko, Alexander, Hryhorchak, Ivan, Politans'kyy, Leonid, Kazemirskiy, Taras, "A Control Unit for a Pulsed NQR-FFT Spectrometer," IAPGOS 5(4), 55-58 (2015).
25. "Cyclone Device Handbook," 7 June 2008 https://www.altera.com/content/dam/altera-www/global/en_US/pdfs/literature/hb/cyc/cyclone_device_handbook.pdf. (15 October 2016).
26. "TFT LCD Specification, Model No.: TD035STEB2," http://d1.ourdev.cn/bbs_upload782111/files_17/ourdev_476815.pdf. (5 May 2015).

Chapter 4
Hardware implementation of NQR radiospectroscopy devices

4.1 Measuring setup for the study of NQR

The pulse method for detecting nuclear quadrupole resonance signals requires the use of high-power radio-frequency excitation pulses and high-sensitivity receiving equipment [1–4]. A block diagram of a laboratory coherent radio spectrometer, proposed for pulse observation of NQR in GaSe and InSe semiconductors, is shown in Fig. 4.1.

The feature of the proposed radio spectrometer is its implementation on the basis of a multifunctional software-controlled digital computational core. Based on the syntax for modeling dynamic modes of logical structures, simulation models and software algorithms have been developed for implementing the basic functional units of the NQR pulse spectrometer in a single module based on Intel's FPGA EP4CE15E22C8 [5].

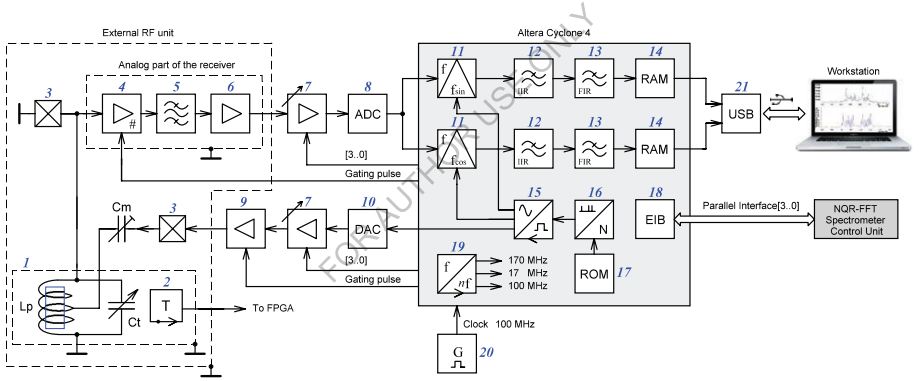

Fig. 4.1 Block diagram of the measuring setup for the study of nuclear quadrupole resonance (NQR): (1) NQR sensor unit; (2) digital thermometer; (3) diode limiters; (4) gated RF amplifier; (5) bandpass filter; (6) matching amplifier; (7) variable gain amplifiers; (8) analog to digital converter; (9) RF transmitter; (10) digital to analog converter; (11) double balanced mixers; (12) integrator-comb filters; (13) compensating filters; (14) random access memory; (15) direct digital synthesizer; (16) multi-pulse generator; (17) read only memory; (18) control module driver; (19) phase-locked loop; (20) crystal oscillator; (21) universal serial bus

The source of the carrier frequency is a three-channel DDS (***15***) based on a 48-bit phase accumulator with the possibility of high-speed frequency and phase shift keying [6]. It provides the generation of NQR excitation pulses in the frequency range of 1 – 50 MHz. The step of setting the frequency of carrier oscillations is $\Delta f_{out} \approx 1 \times 10^{-6}$ Hz. The pulse sequence programmer (***16***) provides the formation of 90º-degree excitation pulses with a duration of 0.1 – 20 μs and a minimum repetition period of 0.1 μs. The duration of the pause between the excitation pulses is adjustable in the range of 0.1 μs – 1 s. Other time lengths, for example, in the Carr-Purcell se-

quence [7], the length of 180-degree pulses and pauses between them is set automatically according to the selected program recorded in the read only memory (***17***). The frequency of the carrier wave, the duration of a 90º-degree excitation pulse, the duration of the pause between pulses and the type of sequence come from the spectrometer control unit to the digital computational core through a four-bit parallel interface.

The analog path of the radio spectrometer is implemented as a functionally complete transmitter-receiver unit containing a gated amplifier (***4***), a band-pass filter (***5***), and code-controlled amplifiers (*7*). The output broadband power amplifier (***9***) is a high-frequency transmitter loaded on an LC circuit (***1***), in the coil of which the test substance is located. The transmitter allows one to develop powerful δ-shaped pulses in the coil with an initial pulse power of 1 kW in the frequency range of 1 – 50 MHz [8].

The radio spectrometer receiver was developed with SDR technology using the DDC principle, which significantly reduced the number of analog path stages and, therefore, significantly reduced the noise contamination of the FID signal and the asymmetry of the detected signal parameters. In the experimental model of the spectrometer, a high-speed 12-bit ADC AD9230BCPZ (170 MSPS conversion rate) was used to digitize the response signal in the resonance frequency range of 1 – 50 MHz [9]. Quadrature signals of the reference frequency enter the inputs of the multipliers (***11***), where their multiplication with the information signal occurs. Since ADC data and DDS reference signals are 12-bit, we get a 24-bit number as a result of multiplication. The multiplication operation will lead to the transfer of the signal spectrum to the low frequency range. In this case, further work with the digital signal sampled at 170 million times per second, is no longer appropriate and resampling to a lower frequency should be made. Before this operation, a LPF is required. In the SDR structure, a series connection of an infinite impulse response (IIR) filters (***12***) is applied, which provide a reduction of the sampling rate by 10 and compensatory FIR-filters (***13***), which serve to equalize the frequency response of the path [10].

Fig. 4.2 Measurement setup for the observation of NQR: 1 – portable digital multipulse NQR spectrometer, 2 – graphical display, 3 – settings panel, 4 – NQR signal sensor, 5 – tuning capacitor, 6 – probe coil, 7 – signal generator, 8 – oscilloscope

A data acquisition system based on a two-channel bidirectional universal serial bus (USB) interface FT2232H (***21***) for processing the response signals of a nuclear spin system is used. The LabVIEW software for FFT and averaging FID signals is developed [11]. The interval between measurements is set by the frequency of the starting pulses, which are synchronized with the USB interface.

4.2 Hardware implementation of a NQR Signal Sensor

The requirements for the NQR sensor are quite stringent. It should withstand RF voltages and quickly restore sensitivity after the action of a powerful excitation pulse. These requirements can be fulfilled by implementing the NQR sensor according to the principle shown in Fig. 4.3. The test sample is placed inside the inductor Lp of the oscillating circuit, adjusted by the capacitor Ct to the resonance frequency (Larmor frequency).

The circuit is physically connected, both with the pulse transmitter, and with the receiver. The intensity of the RF field H_1 in the zone of location of the test sample is expressed by the formula [12]:

$$H_1 \approx 3\left(PQ/\nu_0 V\right)^{\frac{1}{2}},$$

where P is the transmitter power in watts, ν_0 is the resonance frequency in MHz, V is the probe coil volume in cubic centimeters.

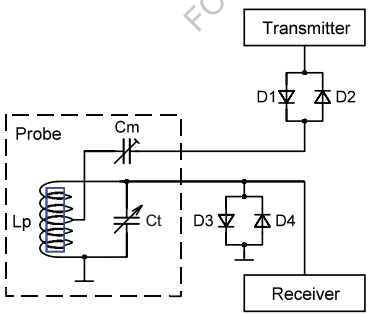

Fig. 4.3 Basic structure of the NQR sensor

The maximum value of H_1 is not the only value that needs to be optimized. It is also necessary to take into account the homogeneity H_1, the rise and fall times of the envelope of the RF pulse, and the sensitivity of the circuit (SNR) when the FID signal passes through it.

Having considered the formula for H_1, one can see that in order to obtain a strong RF field, the volume of the probe coil must be minimized, and the Q factor should be as large as possible. The Q factor of the inductor is expressed by the

formula:

$$Q = 2\pi\nu_0 L / R = \omega_0 L / R,$$

where R is resistance in Ohms, ν_0 is frequency in Hz, L is inductance in H.

Therefore, it is desirable for the probe coil by radio frequency radiation to have a high inductance and low resistance. Still, at the beginning and at the end of the pulse it would be better to have a small Q since the rise and fall times of the tank circuit are related to the Q by the ratio:

$$Q \approx 1.5\nu_0 T_r,$$

where T_r is the free decay time constant of the tank circuit in μs.

The signal/noise ratio in the pulse experiment depends on a number of parameters [13]:

$$\text{SNR} \approx \zeta\gamma I(I+1)C\left(QV\nu_0 T_2 / \beta T_1\right)^{\frac{1}{2}}, \tag{4.1}$$

where ζ is the fill factor of the receiving coil, γ is the gyromagnetic ratio of the corresponding resonant core, I is the spin quantum number of the core, C is a composite constant which includes several coefficients, T_1 and T_2 are the spin-lattice and spin-spin relaxation times, β is the passband of receiver-detector system.

To optimize the SNR, it is desirable to have a large volume of sample under study and a large quality factor Q of parallel oscillating circuit. There is also a limitation $Q < 1.5\nu_0 T_r$. So, if we compare the large Q value required for the receiver and the small Q for the transmitter, then it is clear that when choosing the quality factor, it is necessary to satisfy conflicting requirements. Some compromise is also needed for the probe coil volume. In addition, to achieve the greatest sensitivity of the receiver, the inductance of the probe coil must be large.

The use of quarter-wave cable segments and counter-parallel pairs of diodes ensures a quick change of the system Q when the pulse is switched on and off, therefore it is possible to obtain almost optimal values of the field intensity H_1 and sensitivity.

Usually, to detect signals receiving the NQR response signals, either series or parallel resonance circuits are used. The proposed measurement setup used a parallel oscillating circuit (Fig. 4.3). The capacitor Ct is tuned so that the input circuit has a resonance at the Larmor frequency, which is very important for detecting relatively weak NQR signals (about μV). The capacitor Cm changes the impedance of the circuit and is used for matching. The difficulty is that both of these tunings depend on each other. However, only with proper tuning can you achieve maximum sensitivity. For a parallel circuit, you can obtain the following expressions to determine the ca-

pacities [14]:

$$\mathrm{Cm} = \frac{r}{\sqrt{r\omega^2 Z_0\left(L^2\omega^2 + r^2 - rZ_0\right)}}; \tag{1.2}$$

$$\mathrm{Ct} = \frac{L\omega^2 Z_0 - \sqrt{L^2 r\omega^4 Z_0 - r^2\omega^2 Z_0^2 + r^3\omega^2 Z_0}}{L^2\omega^4 Z_0 + r^2\omega^2 Z_0}, \tag{4.3}$$

where L is the inductance of the probe coil, ω is the angular resonance frequency, Z_0 is the input impedance of the sensor, r is the active resistance of the probe coil.

To optimally adjust the capacitors Ct and Cm, the dependence of their values on the resonance frequency was calculated taking into account expressions (4.2) and (4.3). The initial data were the following parameters: $Z_0 = 50\ \Omega$, $r = 0.01\ \Omega$, $L = 1.1 \times 10^{-6}$ H. The calculation results are shown in Fig. 4.4.

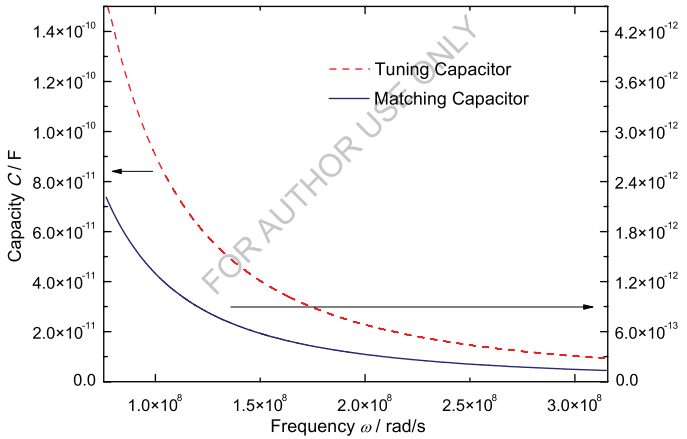

Fig. 4.4 Dependence of nominal values of capacities Ct and Cm on resonance frequency

4.3 Analog signal chain

In the measuring setup developed for the study of NQR, a variant of the receiving unit was proposed, a simplified diagram of which is shown in Fig. 4.5. Gating is performed by applying opposite polar voltages +Us and −Us to the second gate of the dual gate junction gate field effect transistors (JFET) Q1 and Q2.

For the isolation of the receiving circuit and the transmitter in the absence of an excitation pulse, quadruplicate groups of diodes D1–D14 of type 1N4148 are applied, loaded on resistors of 1 kΩ (R2, R3). Combining the pairwise connected diodes into

groups is due to the need for current to flow up to ~4 A into the probe coil for the duration of the excitation pulse. The purpose of such a circuit is to weaken the leakage of the carrier frequency and noise through the diode capacities from the transmitter, as well as partially suppress the transient in an oscillating circuit.

For samples with a volume of ≤0.25 cm^3, inductors (Lp) with a diameter of 7 – 10 mm are used. Samples with a small volume were used to study the NQR in the initial GaSe and InSe crystals prepared for the manufacture of heterojunctions by the "optical contact" method. To preserve the quality factor of the circuit and match with the low-impedance output of the RF power amplifier, the transmitter output is connected to a part of the probe coil turns. A tap to match the output impedance of the transformer with the input impedance of the oscillating circuit is carried out from 25% to 50% of the turns of the Lp and is set experimentally.

The protection of the input stage of the amplifier from the effects of radio frequency radiation is performed on the resistor R1 and high-speed bypass diodes D1, D2. The switching speed of the 1N4148 diodes is 4 ns.

Despite the presence in the schematic shown in Fig. 4.5 of a protective circuit of the elements R1, D1, D2, at the moment of activation of the excitation pulse in the amplifying path of the receiver, a transient process occurs, overloading it. It turned out that the inclusion of a protective link of the types R1, D1, D2 at the inputs of each receiver cascade does not lead to a noticeable attenuation of this effect in the case connection between the cascades of broadband matching transformers.

Fig. 4.6 shows the transient process at the output of the preamplifier caused by radio frequency radiation.

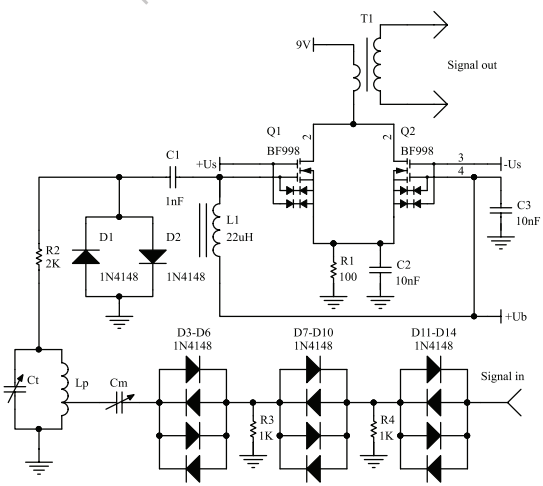

Fig. 4.5 Circuit diagram of the input stage of the NQR spectrometer

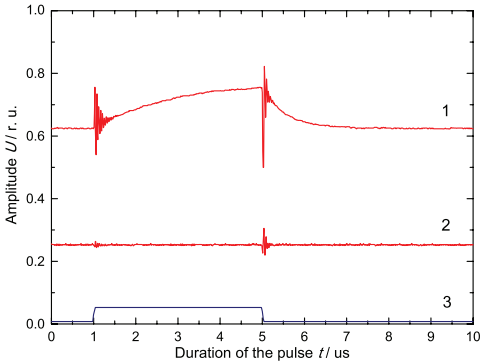

Fig. 4.6 Transient process in the spin signal amplifier: (1) Without a suppression circuit; (2) With the application of the proposed transient suppression circuit; (3) Gating pulse.

A key device for protecting a wideband preamplifier was proposed by Rudakov [15], but the carrier frequency suppression ratio was only 60 dB. In our case, effective gating of the device (up to 100 dB) is provided by three subsequent pairs of same-type dual gate JFETs connected in parallel with respect to the power source (Fig. 4.7).

The circuit diagram and PCB of the analog signal chain are designed using Altium Designer software. The PCB (Fig. 4.8a) is located in a metal case, where electromagnetic shields are between the separate stages (Fig. 4.8b).

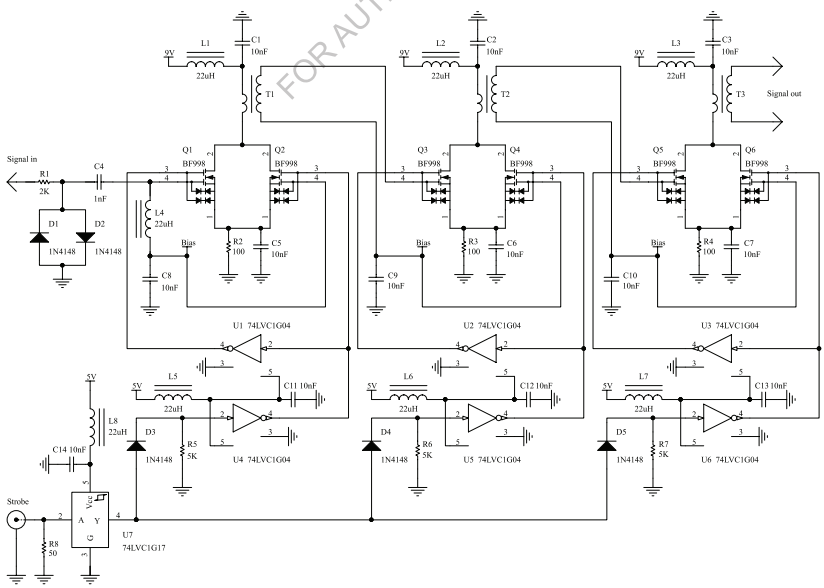

Fig. 4.7 The circuit diagram of the proposed gated amplifier

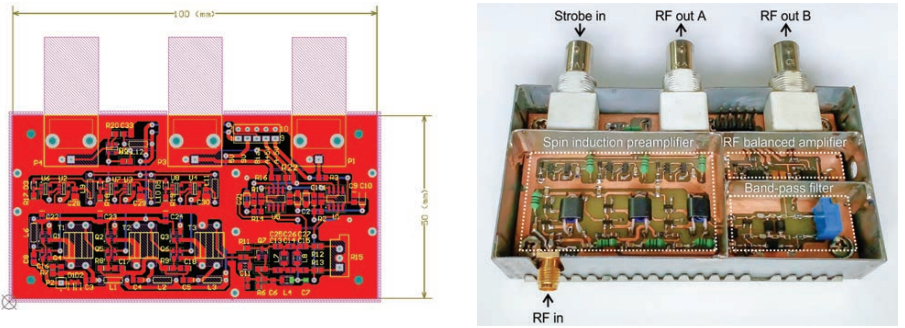

a) b)

Fig. 4.8 The design of the analog signal chain based on the gated amplifier: (a) printed circuit board; (b) device photo

The study of the degree of suppression of the carrier oscillation and the frequency response of the analog signal chain based on the gated amplifier was carried out as follows. A test sinusoidal signal with the amplitude of 0.5 mV was fed from an OWON AG2052F signal generator to the input of the device under study. When studying the carrier oscillation suppression ratio, the amplitude of the signal from the generator assumed a maximum value of 5 V. The amplitudes of the signals at the input and output of the device under investigation were monitored using a Siglent SDS1202CNL digital oscilloscope. The carrier suppression ratio of the device under test (DUT) is within 80 – 100 dB (Fig. 4.9) and the noise factor is about 7 dB in the operating frequency range (Fig. 4.10). For the proposed receiver, the noise factor is slightly higher than in commercial devices. However, the high gain is superior when there is a need to use analog-to-digital conversion for processing of weak signals. The measurement data were analyzed with a Siglent SSA3032X spectrum analyzer.

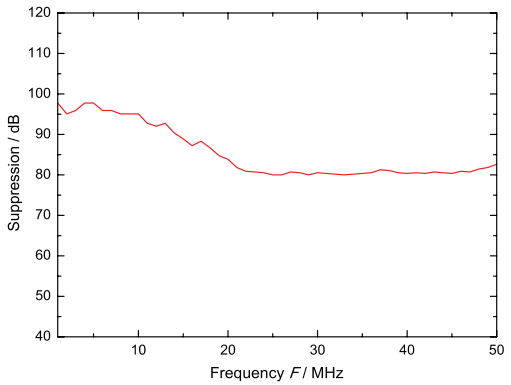

Fig. 4.9 Carrier suppression ratio of the analog signal chain based on the gated amplifier

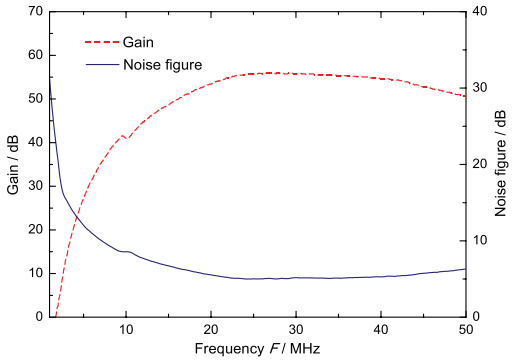

Fig. 4.10 Gain and noise figure of the analog signal chain based on the gated amplifier

The experimental amplitude characteristics of the analog signal chain based on the gated amplifier, obtained for frequencies of 10 MHz, 20 MHz and 30 MHz are shown in Fig. 4.11. From the dependence given, it can be seen that, for all three cases, the high linearity of the characteristics in the range of input signals with amplitudes from 10 uV to 0.5 mV is preserved. The plots use the logarithmic scale of the axes for easy visualization of the range of weak signals. At the output of the generator, a 40 dB attenuator is applied to attenuate the amplitude of the test signal to 5 uV. Minor nonlinearities of amplitude characteristics in the cut-off zone at $U_{\text{p-p}} < 20$ uV (Fig. 4.11) are due to the growth of $1/F$ type noise in the analog path of the measuring setup with a decrease in the operating frequency. When using a reconfigurable bandpass filter, the input sensitivity of the receiver is about 3 – 5 uV, which allows NQR research to be carried out in samples of comparatively small size even without the use of accumulation and averaging algorithms.

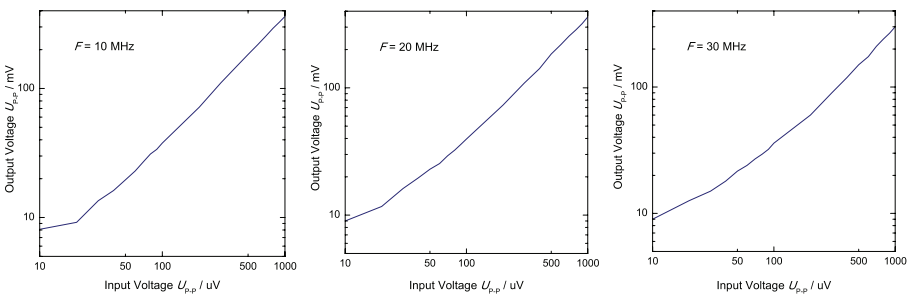

Fig. 4.11 Experimental amplitude characteristics of the analog signal chain based on the gated amplifier

4.4 Hardware implementation of a broadband radio-frequency transmitter

Based on the results of simulation modeling, the basic structure of a broadband RF transmitter of pulsed NQR spectrometer was developed (Fig. 4.12), which comprises the pre-drive, driver and final (power) amplification stages, as well as the matching blocks of the input, output and interstage impedances. The use of a three-stage circuit is dictated by the need to amplify weak signals whose power level is about -2 dBm.

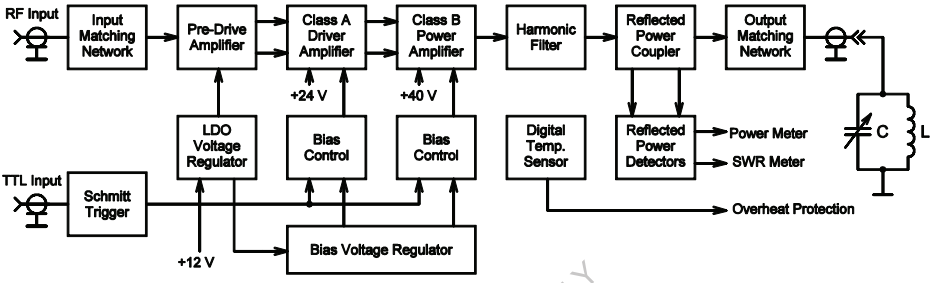

Fig. 4.12 Block-diagram of proposed broadband RF transmitter

The circuit diagram of the proposed transmitter is shown in Fig. 4.13. A preamplifier provides amplification of weak signals from the output of the spectrometer frequency synthesizer [4, 9, 16], as well as matching between the latter's output resistance and the input resistance of transmitter. Pre-amplification stage is based on a low-power RF transistor and operational amplifier with a low noise level. Class A high-linearity drive stage is implemented according to a push-pull circuit based on RF transistors RD16HHF1. It assures output power of the order of 45 dBm, which is necessary for full driving of active components of transmitter output stage. Total quiescent current of this stage is 1 A. Frequency-response equalization of transmitter and reducing the likelihood of its oscillations is assured by the introduction of a negative feedback. Class B output push-pull stage assures pulse power of the order of 57 dBm on the load 50 Ohm. Each branch of the output stage comprises four MOSFET IRF510 connected in parallel. Compensation of the effect of variation in transistor parameters on the value of drain current is achieved by including a resistor of the nominal value 0.5 Ohm into drain circuit of each transistor. For control of reflected wave and optimal matching between transmitter output resistance and the load, a detector based on current-voltage converter and reflected wave power coupler was employed (Fig. 4.13).

Technical implementation of pulsed operation of RF transmitter of NQR spectrometer is shown in Fig. 4.15 as a schematic circuit diagram of bias control module. The source of bias voltage is voltage stabilizer based on two integral low dropout linear regulators U1 and U3 which forms 5 V for transmitter output stage and 9.2 V for

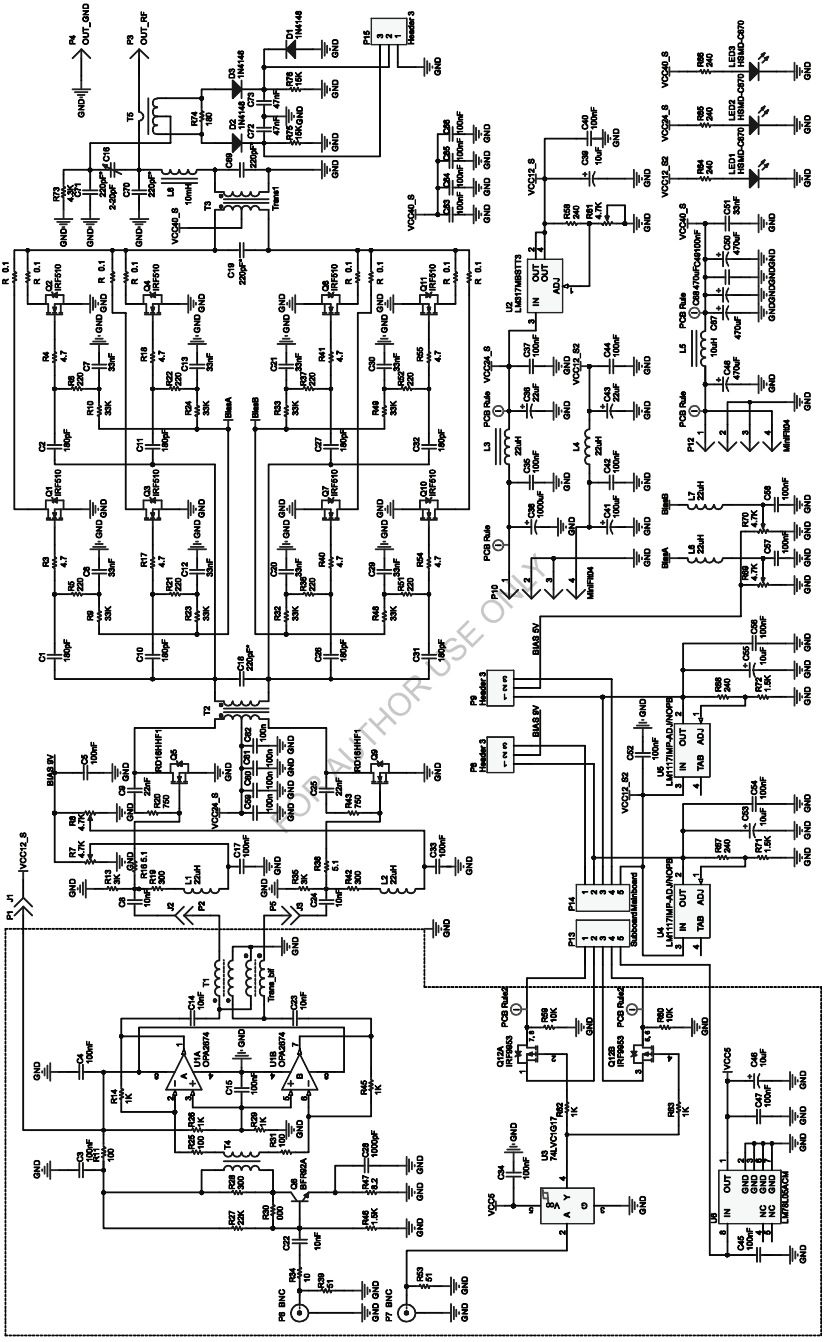

Fig. 4.13 Circuit diagram of the proposed broadband RF transmitter

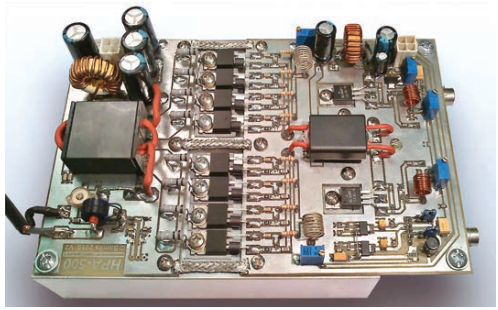

Fig. 4.14 View of the NQR spectrometer transmitter

drive stage. Electronically-controlled switches Q1A and Q1B are based on isolated-gate dual *p*-channel field-effect transistor IRF9953 [17]. The specific feature of this transistor is low gate charge and switching loss assuring a reduction of transient processes in pulse key operating modes. Electronic control is provided from spectrometer main board by "TTL" signal, which through the Schmitt trigger U2 comes to transistor gates Q1A and Q1B. Voltage dividers R1, R5 and R9, R11 are responsible for the nominal value of bias voltages, and thus are based on selected resistors with a low temperature coefficient of resistance and a small parameter spread. Bias control in drive stage is provided by potentiometers R2, R3, and in the output stage – by R14, R15, respectively. To avoid penetration of parasitic RF currents, and, hence, transmitter oscillations, blocking LC units were installed in bias circuits. Switches P1 and P2, if necessary, disable automatic bias control mode and allow passing to manual control.

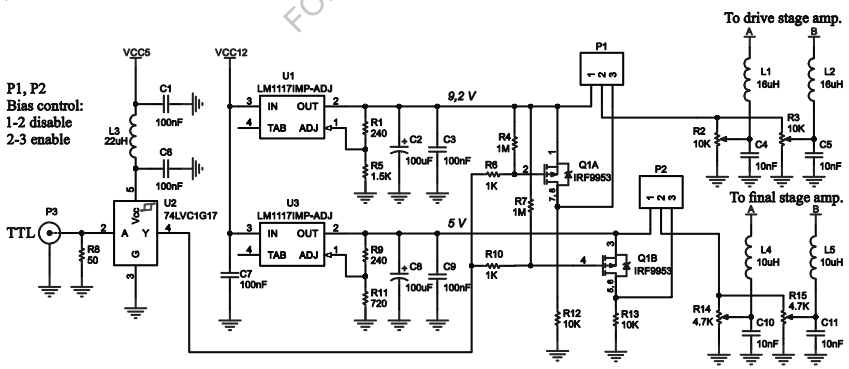

Fig. 4.15 Schematic circuit diagram of bias control module

In the process of experimental research on proposed RF transmitter, a dependence of the module and argument of complex gain $G(j\omega)$ on frequency ω of amplified signal was evaluated. Device parameters were studied at resistive load nominal value 50 Ohm. Parameters of the signals were determined by means of a digital oscilloscope Siglent SDS1102CML. Transmitter frequency response in operating range 1 –

50 MHz is shown in Fig. 4.16a. It is seen that frequency band with the ripple of ±1 dBm is 2 – 38 MHz (Fig. 4.16a, curve 1). Above 37 MHz there is a monotonous response roll-off. Frequency-response equalization on retention of ripple at a level of about ±0.4 dBm in the range of 2 – 38 MHz (Fig. 4.16a, curve 2) was put into practice with correction of input signal level. Correction was realized with calibration of transmitter parameters by the firmware of the main system unit of radio spectrometer. Transmitter with correction provides an average output power 400 – 500 W for the specified frequency range. Research on phase response has shown that phase shift $\Delta\varphi$ is proportional to amplified signal frequency practically over the entire range of operating frequencies Δf.

Rise and fall times determine the accuracy of excitation pulse shape and are one of the main parameters for pulse transmitter where transient processes are caused by reactive circuits. Linear distortions (curvature of pulse leading edge and top) in pulse signal amplifiers are evaluated by comparing their real and ideal transient characteristics. The oscillograms of the output and control signals are given in Fig. 4.16b. Delay time of the output signal relative to the input (build-up of voltage function $U(t)$ to the value 0.5) was about 100 ns. Pulse setup time (build-up of function $U(t)$ from the value 0.1 to 0.9) was about 350 ns. The research showed the absence of visible voltage surges at transmitter output. This suggests the absence of excitations in the process of pulse setup. From the obtained experimental results it may be concluded that total rise time of radio pulse for the developed broadband transmitter did not exceed 500 ns.

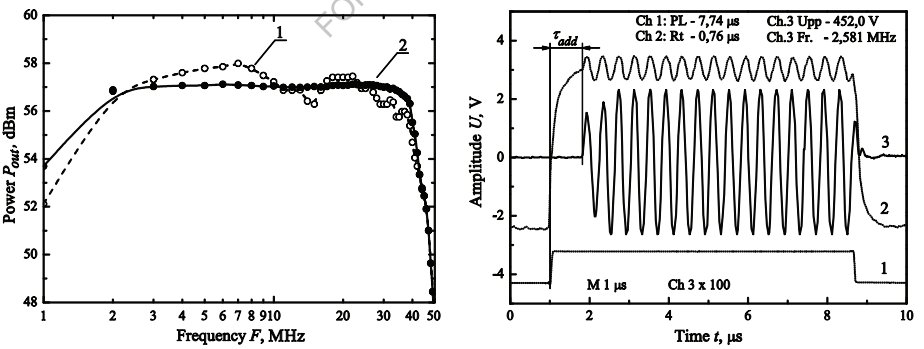

Fig. 4.16 Experimental results: frequency response (a): 1 – without correction, 2 – corrected; voltage oscillograms in pulsed bias mode (b): 1 – control TTL signal, 2 – gate-drain voltage on output stage transistors, 3 – transmitter output signal

To study transmitter board heating the temperature investigations of its surface were performed with the use of Testo-875 thermal imager. The temperature field of the board obtained by thermal-imaging investigation in continuous and pulsed bias

modes ($P_{out} \approx 500$ W, a series of 5 pulses of total duration 100 μs, operation time 10 min) is shown in Fig. 4.17a and Fig. 4.17b, respectively. From the obtained results it follows that heating of device reduced considerably in pulsed bias mode. Specifically, for output stage transistors the average surface temperature decreased by ~ 20 °C, and for drive stage transistors – almost by 10 °C. Proposed mode allows use the RF transmitter without forced air cooling and with stand-alone power system.

Ingenious ideas of the schematics and design of RF transmitters for NQR spectrometers have been presented by the authors of many scientific works. In particular, in [18], a broadband transmitter is described which comprises a shaper of radio-frequency pulses and a power amplifier with a gating system. The fundamental difference between our device and the transmitter described in [18] is all-transistor implementation which makes it possible to reduce weight, overall dimensions, power consumption, as well as simplifies considerably implementation of the power scheme.

The basic specifications of the developed device. Amplifier type – pulsed, power output ~ 500 W, coefficient of amplification – at least 52 dB, the operating frequency range 1 – 50 MHz, amplitude-frequency characteristic unevenness in the range 2 – 38 MHz not more than ± 0.4 dB, sensitivity -2 dBm, pulse setting time 350 ns, rated load resistance 50 Ohm, supply voltage 40 V, overall dimensions 200 × 120 × 65 mm.

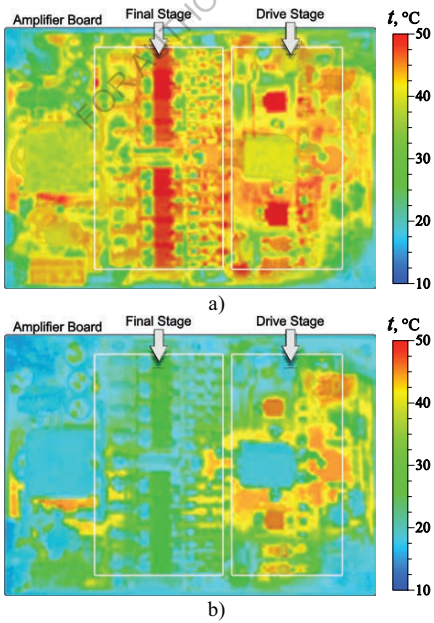

Fig. 4.17 Surface temperature distribution of transmitter board in continuous bias mode (a) and pulsed bias mode (b)

4.5 Hardware implementation of the digital computational core

For firmware implementation of a pulse sequence shaper a system board of pulsed NQR-spectrometer was developed. It consists of digital-to-analog and analog-to-digital converters, low-pass filter, matching and buffer amplifiers, configuration and supply circuits, other functional elements (Fig. 4.18). The product proposed here is based on FPGA EP1C6T144C8N of Altera Cyclone family.

The non-volatile memory of FPGA has information recorded on 30 various types of sequences the use of which assures implementation of a wide range of radio-spectroscopy and relaxation methods in NQR, in particular, for determination of relaxation times T_1 and T_2 (CPMG-type sequence), provision for accumulation of weak NQR signals (SSFP and SLSE sequences) with fast and low relaxations, averaging of nonuniform spectral line broadening with the use of phase-alternated pulse sequence (PAPS), nutational spectroscopy.

DAC is implemented by an external 14-bit digital/analog converter AD9772AASTZ. Filtration of side spectral components caused by nonlinearity of converter operation is provided by an 7th order elliptic analog low-pass filter with cutoff frequency 70 MHz. The amplitude of generated oscillations is controlled by an amplifier AD8369ARU, whose gain is assigned by data word along control bus with FPGA. Matching of device output resistance with the input resistance of high-frequency power amplifier is done using operational amplifier AD8009 with the bandpass of 1 GHz. Interface ports JTAG and Active Serial are provided for loading program algorithm into configuration memory. The device front panel has coaxial connectors for connection of transmitter and receiver paths of radiospectrometer, indicators of synthesizer operation and data transfer. Data exchange with computer through USB interface is via hardware USB-UART controller FT2232H.

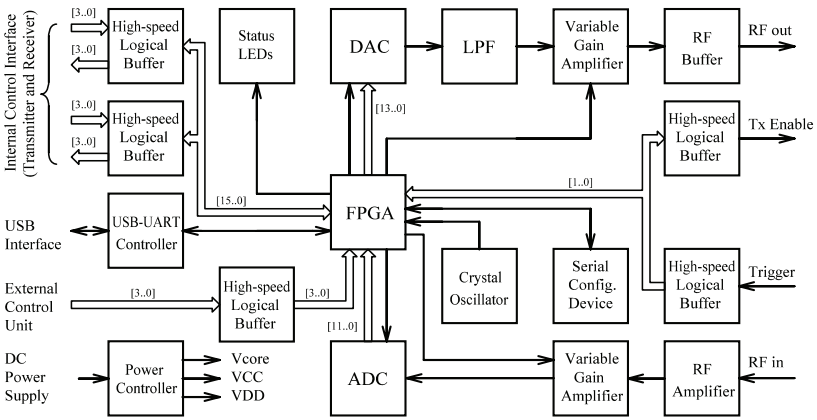

Fig. 4.18 Block diagram of the spectrometer system board

The developed spectrometer system board (Fig. 4.19) provides for not only pulse sequence shaping, but also implementation of the functions of NQR response processing and full control of functional units of NQR Fourier spectrometer. In particular, a channel for ADC based on 12-bit converter AD9230BCPZ-170 and matching amplifier AD8138 is provided for the implementation of digital synchronous detection and subsequent digital processing of NQR response signals, as well as TTL-compatible channels using high-speed logic buffers 74LVC244.

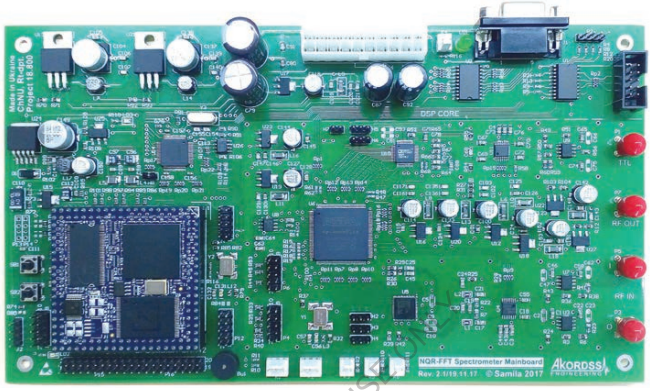

Fig. 4.19 View of the NQR spectrometer system board

The device was studied both in single-pulse mode and multi-pulse mode. Fig. 4.20 shows the voltage oscillograms at the output of device when shaping some sequences most commonly encountered in NQR. The range of operating frequencies of the elaborated device was selected as 1 – 50 MHz, restricted to NQR frequencies of scientifically relevant isotope cores ^{14}N, ^{35}Cl, ^{63}Cu, ^{69}Ga, ^{71}Ga, ^{113}In, ^{115}In, etc.

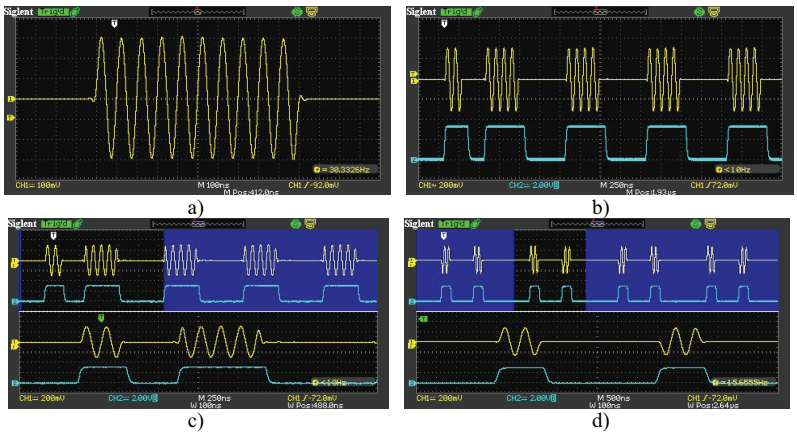

Fig. 4.20 Voltage oscillograms at the output of pulse sequence shaper: single RF pulse (a), Carl-Purcell (b), Meiboom-Gill (c), MREV-8 (WAHUHA) (d)

4.6 Hardware implementation of the control system

Structurally, the radio spectrometer control system is executed in the form of a modular structure (Fig. 4.21), which includes the core board with the core on the basis of EP1C12F324, LCD TD035STEB2 and I/O ports. Information on the work of radio spectrometer and current settings is displayed on a 3.50-inch LCD. Sound indication is provided by an electromagnetic sound emitter. Matrix keyboard 4×4 provides operator with navigation on the menu and introduction of settings of radio spectrometer parameters, current values of which are stored in a nonvolatile memory. The formation of clock and synchronizing pulses of the device is provided by a thermostabilized quartz oscillator with a frequency of 24 MHz.

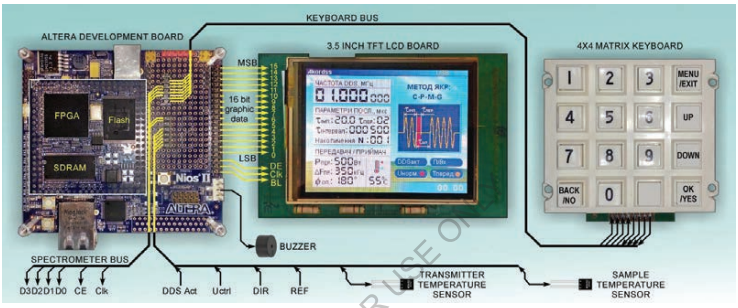

Fig. 4.21 Modular structure of the developed control system of the NQR radio spectrometer

Control of the temperature in the radio spectrometer measuring cell and transmitter heating is provided by two digital DS18B20 temperature sensors connected to IC through the 1-Wire Interface. The selected resolution of the temperature converters is 0.125 °C. For measuring the frequency, a separate channel of the frequency meter is provided. The device also implements a real-time clock based on the DS3231SN chip with standalone power. The presence of said units will allow to fix quickly and efficiently not only the resonance frequencies of the NQR, but also the time and operating temperature of the experiment, which is especially important in the study of samples with the temperature dependence of the parameters of the resonance spectra [19, 20]. For control of abnormal situations (excess of maximum output power, overheating of the spectrometer units, instability of supply voltages, etc.), there are separate ports of 1-Wire type which receive error signals (DDS_Act, Uctrl, DIR, REF). In case of deviation from the norm of the specified parameters, the warning symbols are displayed and the spectrometer operation is blocked.

The transfer of commands to the radio spectrophotometer's execution units is provided through a 4-bit interface bus (IB) with a data rate of 3.15 Mb/s. This bus allows transmission of a parallel parameter setting code to the motherboard, and then to the digital frequency synthesizer, radio pulse shaper, sequencer, reception and transmission path, controlled filters, and other functional units of the radio spectrometer.

Parameters of generated code sequences of NQR radio spectrometer control that are passed to its IB are given in Table 4.1. The power scheme of the device is conventionally divided into a control unit, a block of main and regular voltage stabilizers and an electronically controlled key. The latter allows implementation of the "standby mode" and the compatibility with the external power supply of ATX standard, potential free management of which is done through the port "P_ON".

The working model of the developed control system was tested along with the frequency synthesizer and the shaper of pulsed sequences of the NQR radio spectrometer [9]. The created multipage menu allows convenient and intuitive adjustment of parameters of the NQR spectrometer. The results of the model testing showed that its functionality corresponds to all the requirements for the portable equipment of relaxation and pulse-resonance spectroscopy.

Table 4.1 Parameters of code sequences

Parameter	Value range	Unit	Word length
Frequency synthesizer			
Carrier frequency	10÷50000000	Hz	28 bit
Generator of the excitation sequence			
Excitation pulse duration	0,1÷100	μs	12 bit
The duration of the "dead" time	0,1÷100	μs	12 bit
Pause duration	1×10^{-6} – 1	sec	24 bit
Sequence number	1–6	-	4 bit
Transmitter			
Output power	100 –1000	W	4 bit
Receiver			
Filter bandwidth	1 – 990	kHz	12 bit
LF signal amplification	0 – 99	dB	8 bit
Reference signal phase	0 – 359	deg	12 bit
Number of iterations	1 – 512	-	12 bit

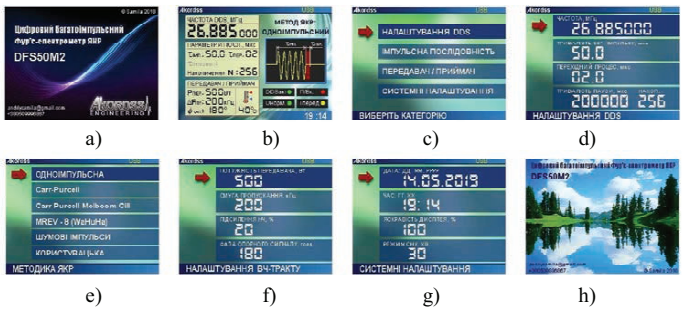

a) b) c) d)

e) f) g) h)

Fig. 4.22 Graphical interface of the control system of the radio spectrometer: start screen (a), user interface screen (b), menu entry (c), synthesizer settings (d), choice of technique (e), setup the RF path (f), system settings (g), screen saver (h)

4.7 Conclusions

A low-cost digital pulsed NQR radio-spectrometer is proposed, all main modules of digital processing and synthesis of which are implemented on the Intel's Cyclone IV FPGA. This significantly reduces the cost of the device and allows its operational configuration with FPGA programming. The volume of FPGA EP4CE15E22C8 hardware resources used was as follows: total logic elements – 9826 (64%), total registers – 2416, total pins – 61 (74%), total memory bits – 160,868 (31%), embedded multiplier 9-bit elements – 13 (12%), total PLL – 1 (25%).

A concept of construction of transmission path of portable NQR spectrometer was developed. In order to reduce power consumption and, as a consequence, total power dissipation, pulsed bias control of transistor operating points was used. As a result, the dissipated power was reduced by 98.39 – 45.8 % for radio pulses of relative duration $0.001 \le D \le 0.1$. The proposed method for increasing the energy efficiency of transmitter can be used in the development of portable setups for the pursuance of the research in the field of NQR spectroscopy and relaxometry.

The digital multifunctional control system for pulsed NQR Fourier radio spectrometer is developed. Experimental tests of the working model in combination with frequency synthesizer and shaper of pulse sequences of the NQR radio spectrometer have been carried out, which confirmed the functionality of the development and its compatibility with the existing standards of NQR spectroscopy equipment.

References

1. Samila A., Hotra O. A Low-Cost Digital Pulsed Coherent Spectrometer for Investigation of NQR in Layered Semiconductor GaSe and InSe Crystals. Electronics. 2020. Vol. 9, Issue 12. P. 1996-1-12.
2. Samila, A.P.; Politansky, L.F.; Hotra, O.Z. A portable digital multipulse NQR spectrometer for the study of the sensory properties, structure and defects in layered semiconductors. In TCSET'2020 International Conference 2020, Lviv-Slavske, Ukraine.
3. J.C. Harding, D.A. Wade, R.A. Marino, E.G. Sauer, S.M. Klainer, A pulsed NQR-FFT spectrometer for nitrogen-14, J. Magn. Reson. 36 (1979) 21–33, http://dx.doi.org/10.1016/0022-2364(79)90212-9.
4. A. Samila, V. Khandozhko, L. Politansky, Energy efficiency increase of NQR spectrometer transmitter at pulse resonance excitation with noise signals, Solid State Nucl. Magn. Reson. 87(2017) 10–17, https://doi.org/10.1016/j.ssnmr.2017.06.001.
5. Cyclone IV Device Datasheet - Intel, https://www.intel.com/content/dam/www/programmable/us/en/pdfs/literature/hb/cyclone-iv/cyiv-53001.pdf, (ac-

cessed Feb 02, 2019).
6. Andriy Samila, Galina Lastivka, Leonid Politansky, Taras Kazemirskiy, Waveform generation for the digital synthesis systems based on embedded hardware, TCSET'2018 International Conference, Lviv-Slavske, Ukraine, 2018, February 20-24; pp. 831–834, https://doi.org/10.1109/TCSET.2018.8336326.
7. L. E. Kay, L. K. Nicholson, F. Delaglio, A. Bax, D. A. Torchia, Pulse sequences for removal of the effects of cross correlation between dipolar and chemical-shift anisotropy relaxation mechanisms on the measurement of heteronuclear T1 and T2 values in proteins, J. Magn. Reson. 97(1992) 359–375, https://doi.org/10.1016/0022-2364(92)90320-7.
8. V. A. Zabrodin, V. P. Tarasov, B. A. Shumm, L. N. Erofeev, A transmit-receive section of a pulsed nuclear magnetic resonance spectrometer, Instrum. Exp. Tech. 50 (2007) 86–90, https://doi.org/10.1134/S0020441207010113.
9. Yu. Bobalo, Z. Hotra, O. Hotra, L. Politans'kyy, A. Samila, Implementation of pulsed radiospectroscopy methods of NQR based on FPGA, Metrol. Meas. Syst. 22 (2015) 363-370, http://dx.doi.org/10.1515/mms-2015-0029.
10. O. Hotra, A. Samila, L. Politansky, Synthesis of the configuration structure of digital receiver of NQR radiospectrometer, Przegląd Elektrotechniczny. 94 (2018) 58–61, https://doi.org/10.15199/48.2018.07.14.
11. Andriy Samila, Olexandr Hres, Georgiy Rozorynov, Hardware and software implementation of data acquisition system for pulsed NQR spectrometer, TCSET'2018 International Conference, Lviv-Slavske, Ukraine, 2018, February 20-24; pp. 1166–1169, https://doi.org/10.1109/TCSET.2018.8336402.
12. Gilbert Clark, W. Pulsed nuclear resonance apparatus. Review of Scientific Instruments 1964, 35, 316–333.
13. G. V. Mozzhukhin, G. S. Kupriyanova, D. V. Shibalkin, V. V. Fedotov, Optimizatsiya priyemo-peredayushchey sistemy YaKR-detektorov azotsoderzhashchikh soyedineniy [Optimization of the receiving and transmitting system of NQR detectors of nitrogen-containing compounds], Vestnik rossiyskogo gosudarstvennogo universiteta im. I. Kanta : Fiziko-matematicheskiye nauki. 3 (2007) 46–54 (in Russian).
14. Design of Impedance Matching Networks for NMR and NQR Studies in the HF Band. (September 2016). http://www.phys.ufl.edu/~majewski/letters/match.pdf
15. Rudakov, T.N.; Shpilevoi, A.A. An Input Device for the Receiving Channel of a Nuclear Quadrupole Resonance Spectrometer. Instrum. Exp. Tech. 1997, 40, 215–216.
16. A.G. Khandozhko, V.A. Khandozhko, A.P. Samila, A pulse coherent NQR spectrometer with effective transient suppression, East.-Eur. J. Enterp. Technol. 6 (12) (2013) 21–25, http://dx.doi.org/10.15587/1729-4061.2013.19700.

17. Datasheet of IRF9953
18. V.V. Fedotov, G.V. Mozzhukhin, G.S. Kupriyanova, Wide band transmitter for NQR spectrometer, Pribory i technika Experimenta. 3 (1986) 155–156.
19. Balazjuk, V., Khandozhko, V., Kovalyuk, Z., Raranskii, N., Samila, A., "Temperature and baric dependence of nuclear quadruple resonance spectra in indium and gallium monoselenides," Proc. SPIE 9066, 90661G1-7 (2013).
20. Samila, A. P., Khandozhko, V. O., Kovalyuk, Z. D., "The nuclear quadrupole resonance and sensory properties of GaSe and InSe layered semiconductors," Journal of Nano- and Electronic Physics 7(3), 030241-5 (2015).

Chapter 5
Hardware and software implementation of NQR data acquisition system

5.1 Hardware implementation of data acquisition system

A key for the organization and performance of a radiophysical experiment is the availability of a convenient data acquisition system (DAS) [1]. In the case of NQR research by the pulsed method, it is possible to formulate a number of requirements to DAS, such as high speed and throughput, probe pulse triggering synchronization, possibility of multiple triggers for the implementation of digital accumulation and averaging of resonance signals. At the same time, an integral part of DAS is a convenient and universal interface for communication with a PC. Proceeding from the above requirements and the range of hardware interface solutions, for the implementation of DAS, the FT2232H microcircuit of the multiprotocol, bidirectional USB↔245FIFO converter, which provides data transfer rate up to 480 MB/s was selected [2].

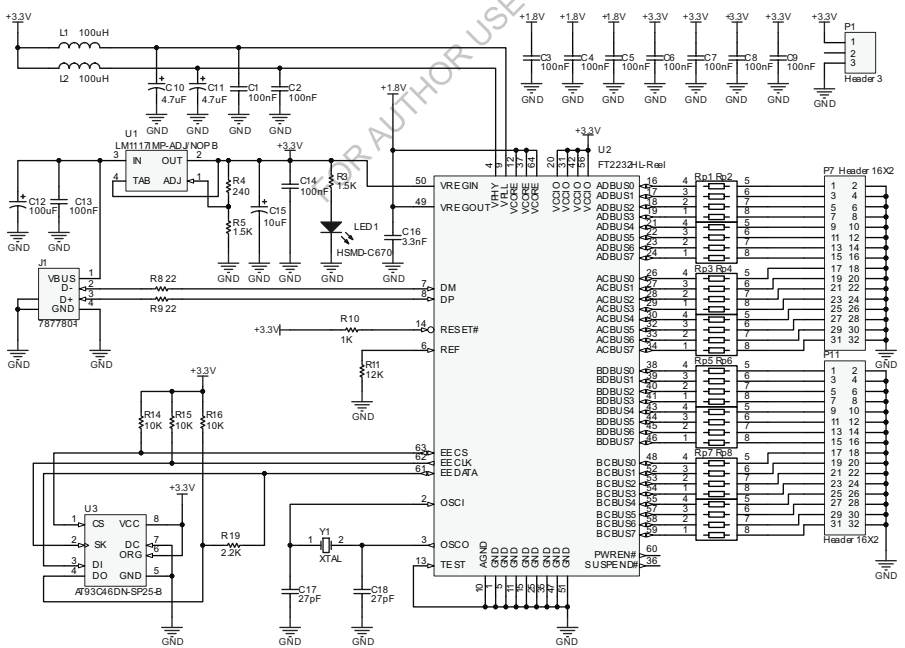

Fig. 5.1 The circuit diagram of the DAS hardware

The FT2232H microcircuit provides the ability to work with serial and parallel interfaces. The presence of 8 kB of buffer memory allows recording 65536 points in one cycle, which at the data transfer rate of 15 MB/s (asynchronous FIFO FT245 mode) is equivalent to the time interval of the FID signal ~4.4 ms. With regard to the fact that the NQR spectral width for most atomic isotopes does not exceed 1 MHz, the use of the asynchronous FIFO FT245 mode is quite sufficient for the implementation of DAS. In so doing, the second channel FT2232H is used to transfer instruction commands for controlling NQR radio spectrometer.

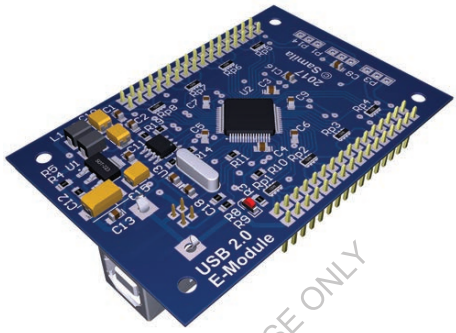

Fig. 5.2 3D model of the USB interface developed for the NQR pulsed spectrometer DAS

5.2 Synthesis of the LabView virtual instrument

The task of visualization and processing of radiophysical experiment data was solved by creating the National Instruments LabVIEW based software. The LabVIEW CAD provides a wide range of capabilities for many measuring instruments and functions for mathematical processing of measurement results.

The virtual tool of DAS is synthesized by means of graphical object-oriented programming. The source code for the implementation of the virtual tool is its block-diagram which reflects graphical representation of programmable task. Fig. 5.3 shows a block-diagram of virtual tool subroutine with a function of processing data array obtained from a real object using USB-interface based on FT2232H and the external ADC and subsequent visualization of the FID signal. The use of Timed Loop synchronized loop allowed implementation of multiple experiments mode for digital data averaging. The Flat Sequence Structure (upper part of schematic in Fig. 5.3) is implemented on the basis of FTDI libraries and serves to initialize the hardware USB device, transfer it to receive mode and bytewise transfer of data to other virtual tools of Timed Loop.

The FID signal on exposure to radio-frequency excitation pulse for k-th resonance frequency has the form of an exponentially damping oscillation:

$$s(t) = A\sum_{k=1}^{d} K_k e^{-[\beta_k + i\omega_k(T)]t} + n(t),$$

where A is general magnitude the value of which is determined by the power of excitation signal; K_k is scale coefficient for the amplitude of k-th component; β_k is signal damping coefficient depending on the duration of relaxation processes inside spin system; $\omega_k(T)$ is resonance frequency of NQR depending on temperature T; $n(t)$ is noise component of FID signal.

The complex Fourier series of the sampled FID signal represented by a sequence of N references on the observation range $T_c = NT_s$ will be given by:

$$s_s(t) = T_s \sum_{k=\infty}^{\infty} \dot{C}_k e^{j2\pi k \frac{t}{T_c}},$$

where $k = 0, \pm1, \pm2, \ldots$, T_s is sampling interval, and complex coefficients of the series are complex amplitudes of spectral components:

$$\dot{C}_k = \frac{1}{N}\sum_{n=0}^{N-1} s(n) e^{-j2\pi k \frac{n}{N}}.$$

The direct use of discrete Fourier transform (DFT) for N samples requires an increase in PC computing resources. However, in our case the size of the sequence satisfies the condition $N = 2^m = 65536$, so for calculation we use FFT.

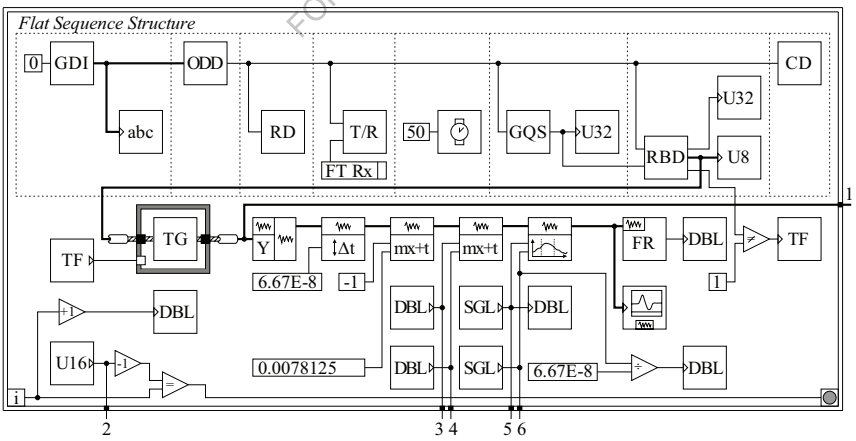

Fig. 5.3 Block-diagram of virtual tool subroutine for reading and processing of experimental data array: abc – ASCII terminal, DBL – terminal of double-precision numbers, FR – carrier frequency definition block, SGL –terminal of single-precision numbers, TF – terminal of logic data, TG – synchronization block, U8(U16) – terminal of unsigned integers. Procedure statements of FTDI device: GDI – memory selection, ODD – provision of access, RD – reset, T/R – memory selection, GQS – reading of data byte in a buffer, RBD – reading of data byte, CD – end of access

To implement FFT in order to visualize the averaged FID signal in the frequency domain and to analyze the individual components of NQR spectrum, a block-diagram of virtual tool DAS subroutine was implemented which is shown in Fig. 5.4. The block diagram, based on the FFT and PS/PSD modules, allows the use of algorithms for window digital processing of the spectral characteristics of the FID signals (rectangular, Henning, Hamming, Blackman, etc.) and also provides an opportunity to display the energy spectrum of NQR.

Analysis of the amplitude spectrum of the sampled signal involves determination of modules (C_1, C_2, ..., $C_{N/2}$) and arguments (φ_1, φ_2, ..., $\varphi_{N/2}$) of complex Fourier spectrum coefficients and calculation of instantaneous values of spectral harmonics:

$$s_1(n) = 2C_1 \cos\left(2\pi \frac{n}{N} + \varphi_1\right);$$

$$s_2(n) = 2C_2 \cos\left(4\pi \frac{n}{N} + \varphi_2\right);$$

.....

$$s_{N/2}(n) = C_{N/2} \cos\left(\kappa 2\pi \frac{n}{N} + \varphi_{N/2}\right).$$

Similar to the interval T_s in the time domain, there is an interval between the components of C_k, which determines the frequency resolution

$$\Delta f = \frac{f_s}{N}.$$

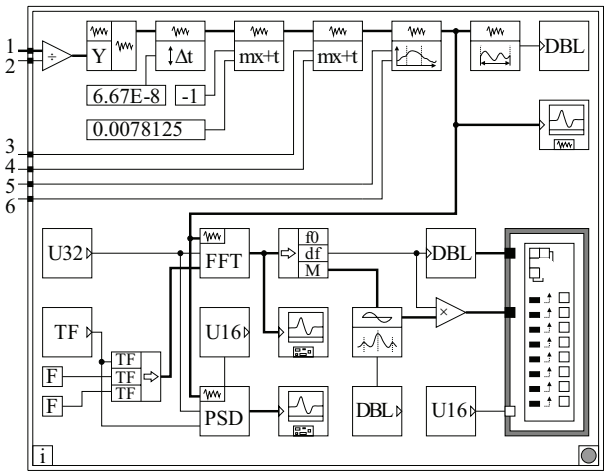

Fig. 5.4 Block-diagram of virtual tool subroutine for spectral analysis of the FID signal

The FID signal is digitized at sampling frequency $f_s = 15$ MHz, so the interval between N samples is about 6.67×10^{-8} s. With a constant f_s, the frequency interval Δf for $N = 65536$ is 229 Hz and increases to 0.9 kHz with a decrease of N to 16384 (the case of recording NQR multiplet broadband spectra, duration of the FID signal ≈ 650 μs).

Graphical user interface (GUI) of virtual tool synthesized for DAS of pulsed NQR spectrometer is shown on Fig. 5.5.

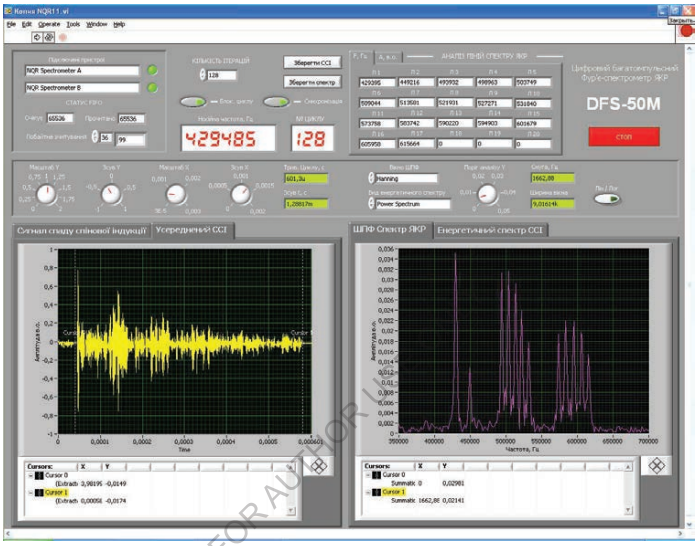

Fig. 5.5 GUI of the LabVIEW virtual tool, developed for DAS of pulsed NQR spectrometer

5.3 Experimental investigations of DAS

Experimental tests of the developed DAS for pulsed NQR spectrometer were conducted under laboratory conditions with the use of the test FID signal typical of NQR isotope ^{115}In of InSe. The specific feature of this crystalline structure is the availability of polytype modifications leading to complex multiplet NQR spectra. So, the main criteria for the selection of NQR isotope ^{115}In as a test signal were: the number of spectral components – 12 lines, wide frequency range ≈ 600 kHz, high spectrum resolution – up to 5 lines per frequency bandwidth 40 – 50 kHz. The test signal NQR ^{115}In which corresponds to spin transition at a frequency of 20.5 MHz was synthesized in MATLAB Simulink and loaded into the memory of generator (Fig. 5.6) [3]. To digitize the signal and buffer the data into the hardware module of the USB interface, a debug board containing a programmable logic integrated circuit EP1C6Q240C8 and ADC AD9280ARS was applied.

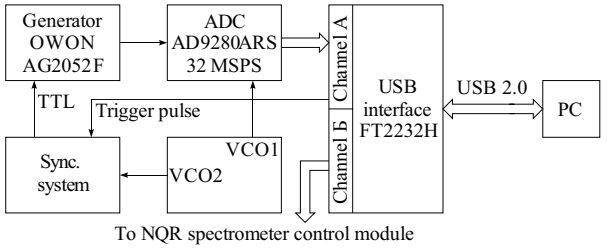

Fig. 5.6 Laboratory stand for experimental tests of the developed DAS of pulsed NQR spectrometer: VCO1 – 15 MHz, VCO2 – 50 MHz, TTL –clock input of digital signal generator OWON AG2052F

The condition for the correct performance of radiophysical experiment is the presence of synchronization between the beginning of DAS operating cycle and the start of NQR probe pulse. To implement the synchronization task, a configuration structure on programmable logic integrated circuit was developed (Fig. 5.7). It consists of three timers and ensures formation of the trigger sync pulse of NQR spectrometer at its output, in conformity with the arrival of USB-initialization pulse package to its input. The first timer sets the duration of a blanking pulse (5 μs) necessary for shunting the input of the radiospectrometer receiving channel during the action of the probe pulse and the transient process in spectrometer coil, the second – the duration of the sync pulse (1 μs), the third – the duration of experiment repetition cycle (500 ms). The LPM Counter modules serve as meters of clock pulses with a frequency of 15 MHz and set the value of time intervals according to the values of constants LPM Constant.

Table 5.1 gives a comparison of technical characteristics of the developed DAS to the nearest prototypes. The use of the proposed DAS in portable NQR radiospectrometers will significantly reduce the cost of laboratory equipment while ensuring the high level of conditions for radiophysical experiments in the fields of NQR and relaxation spectroscopy.

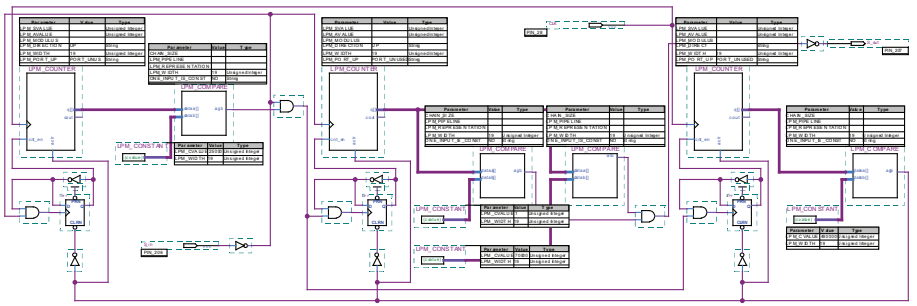

Fig. 5.7 Trigger sync pulse formation circuit

Table 5.1 Comparison of technical characteristics of the developed DAS to the nearest prototypes

Parameter	Developed DAS	DAS based on USB oscilloscope BORDO-421 [4]	SpinCore RadioProcessor-G [5]
ADC sampling frequency	7.5 – 15 MHz[a]	100 MHz	75 MHz
ADC capacity	16 – 8 bit[a]	10 bit	14 bit
Registered spectrum width	3.75 – 7.5 MHz[a]	50 MHz	9,4 MHz
Frequency resolution	229 Hz	763 Hz	72 Hz
Number of complex points	32768 – 65536[a]	65536	16384
PC interface	USB	USB	PCI
Cost of DAS equipment	50 c.u.[b]	365 c.u.	2500 c.u.

a) Programmatically set in the above ranges depending on parameters of external ADC (determined by the experimental conditions).

5.4 Conclusions

The result of solving the task of data acquisition of nuclear spin induction signal was development of a compact DAS for a pulsed NQR spectrometer through the hardware implementation of high-speed USB-interface and the synthesis of the LabVIEW virtual tool. Experimental studies of the proposed system have shown that:

- The formation of the trigger sync pulse makes it possible to use the system in multiple experiments mode for the purpose of digital accumulation and averaging of data;

- An indicator of high informativeness of the developed DAS is visualization of complex multiplet spectra of NQR with the bandwidth up to 7.5 MHz and frequency resolution ≈ 200 Hz.

References

1. Samila A., Hotra O. A Low-Cost Digital Pulsed Coherent Spectrometer for Investigation of NQR in Layered Semiconductor GaSe and InSe Crystals. Electronics. 2020. Vol. 9, Issue 12. P. 1996-1-12.
2. http://www.ftdichip.com/Support/Documents/DataSheets/ICs/DS_FT2232H.pdf.
3. Andriy Samila, Galina Lastivka, Leonid Politansky, "A Computational Model of Signal Transformations in Pulsed NQR Spectrometer, "The International Conference TCSET 2016 “Modern problems of radio engineering, telecommunications, and computer science”, Ukraine, Lviv-Slavske, pp. 37–39, 2016.
4. A.G. Khandozhko, V.A. Khandozhko, A.P. Samila, A pulse coherent NQR spectrometer with effective transient suppression, East.-Eur. J. Enterp. Technol. 6 (12) (2013) 21–25, http://dx.doi.org/10.15587/1729-4061.2013.19700.
5. http://www.spincore.com/CD/RadioProcessor-G/RadioProcessor-G_Manual.pdf.

Chapter 6
Experimental methods of the layered semiconductor materials NQR spectroscopy

6.1 Temperature and baric dependence of nuclear quadruple resonance spectra in indium and gallium monoselenides

The occurrence of quadruple moments of gallium and indium isotopes in GaSe and InSe makes it possible to use NQR method for studying the properties of crystalline structure. The presence of polytype modifications in the crystalline structure of GaSe and InSe results in complex multiplet NQR spectra of ^{69}Ga and ^{115}In isotopes. According to studies of NQR spectra, in GaSe and InSe there is the temperature dependence of resonance frequency typical of a number of compounds.

The temperature and pressure effect on the properties of layered semiconductor crystals GaSe and InSe was studied by many authors [1–7]. The emphasis was on the change in structural, kinetic and optical properties under pressure. The measurements were carried out in a wide range of pressures (up to 30 GPa). It was established that structural transformations take place in these compounds, namely hexagonal lattice goes to cubic one of NaCl type, for InSe at ≈ 10.5 GPa, and for GaSe – in the vicinity of 25 GPa [4]. Due to their capability of retaining properties and structure reproducibility in certain pressure range, indium and gallium monoselenides can be used for pressure sensors.

An attempt to use pressure effect for improving photoelectric parameters of heterojunction was made in [8] where photosensitivity of *p*-GaSe - *n*-InSe based heterostructure photodiode was studied as a function of uniaxial pressure applied in the range of 0 – 70 kPa. It was established that at a pressure of $P \approx 55 – 60$ kPa there is efficiency increase by more than 3.2 %. For practical use of heterostructure photodiodes with increased photosensitivity under constant pressure it is proposed to use packaging of such structures with the active area up to 1 cm^2. An example of using indium, gallium monoselenides and their intercalates for the manufacture of strain gauges is given in [9], where the sensitivity to change in electric resistance is studied as a function of layered crystal strain. The authors of this work employed all-round gas compression up to 150 kg/cm^2. The analysis results show that in the samples of layered lamella-shaped crystals of basic importance is uniaxial pressure applied normal to the plane of atomic layers, i.e. $F \| c$, where c is crystal optical axis. The highest strain sensitivity was obtained for dynamic pressures.

It is known that GaSe can be used as a temperature sensor whose operating principle is based on the temperature dependence of semiconductor crystal resistance. The temperature dependence of electrical parameters of gallium selenide is discussed

in a series of scientific papers [10–12]. The temperature dependence of resistivity which is particularly pronounced in the range of 10 to 110 K is observed in [10]. With further decrease in temperature, a change in crystal resistance attenuates considerably. In [11] it is shown that electric conductivity of GaSe crystal, non-irradiated with electrons, monotonously changes more than by an order in the range of 100 to 500 K. The temperature dependence of electric conductivity can be used for creation of resistance thermometer based on the undoped semiconductor crystal GaSe, which also follows from [12]. The temperature peculiarities of kinetic properties were also investigated in InSe (see, for instance [13]. Both compounds show essential temperature dependence of electric conductivity allowing their use as temperature sensors. However, low parameter stability and their non-reproducibility in time because of specific features of crystal layered structure make the use of thermometers based on indium and gallium monoselenides of little promise.

It is known that in a number of solids there is the temperature dependence of NQR frequency owing to which the measured frequency can be unambiguously related to the temperature of object under study [14]. The NQR-thermometer offers the advantage of temporally unrestricted stability, since the temperature dependence of frequency is determined only by molecular properties of substance and remains unvaried for all samples of this chemical substance. In this case the layered semiconductor compound GaSe possesses ^{69}Ga and 71Ga isotopes which in crystal anisotropic structure assure the effect of NQR. Our investigations have shown that in GaSe there is a relatively strong temperature dependence of the frequency of said quadruple nuclei, and the measured frequency is temperature criterion. In the temperature range of 250 ^{o}K to 390 ^{o}K the temperature dependence of frequency is close to linear and only with further reduction (to liquid nitrogen temperature) there is marked deviation from the linear dependence.

To prepare working samples, as a thermometric material in NQR-thermometer the undoped GaSe crystal is annealed in vacuum according to the following scheme: 400 ^{o}C for 4 hours, 200 ^{o}C – 6 hours; 150 ^{o}C – 10 hours. Annealing performed under the above temperatures results in structural defects ordering, i.e. polytypism and stabilizes their composition. The latter affects the quality of spectra of NQR resonance lines, namely the number of resonance absorption lines is reduced, and spectral resolution is increased [15]. The spectrum obtained by pulsed method of NQR with a fast Fourier transform for annealed GaSe crystal is represented in Fig. 6.1. Because of the presence in the crystal of ε- and γ-modifications of polytypism, the spectrum consists of two groups of lines displaced on the frequency scale by the distance of 52.14 kHz.

The object of temperature measurement is the frequency of the most intensive line from the first or second group (Fig. 6.1). The resonance frequency at 20°C is as

follows: for *a* line – 19110 kHz, for *b* line – 19162 kHz. Fig. 6.2 shows the temperature dependence of the frequency of two spectral lines (*a* and *b*), whence it is seen that in the range of 250 °K to 400 °K it is linear with conversion slope 1.54 kHz/degree. With further temperature reduction (to liquid nitrogen temperature), the dependence deviates from the linear one. For keeping track of temperature, one can use either steady-state NQR method, or pulsed method with fast Fourier transform of nuclear induction decay.

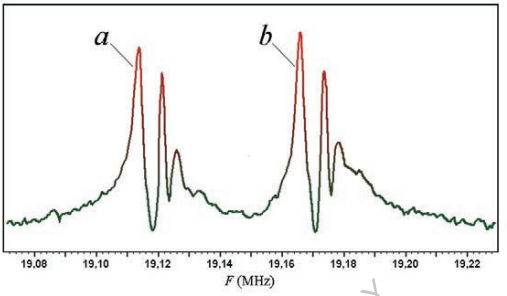

Fig. 6.1 NQR spectrum for ^{69}Ga isotope in GaSe: intensity of resonance lines on the scale of resonance frequencies

The NQR frequency at constant ambient pressure depends only on temperature and is determined by fundamental substance constants. For any configurations of sample-sensor geometry the frequency-temperature ratio is related unambiguously and the temperature scale is determined by selection of primary temperature standard. The accuracy of temperature measurement depends on the line width and in the example cited it is ±0.05 °C. With a decrease in temperature, the accuracy is improved to ±0.025 °C due to a reduction of resonance line width. The tested range of measured temperatures is 77 °K – 400 °K.

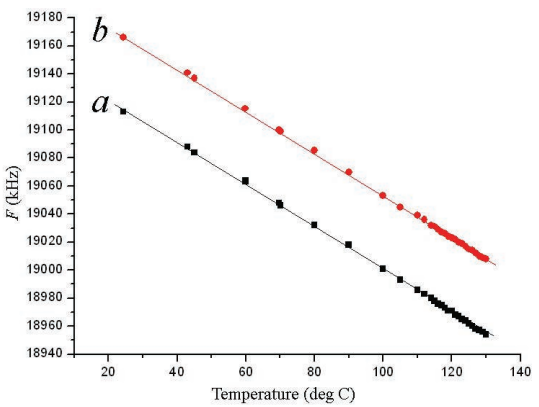

Fig. 6.2 Temperature dependence of NQR frequency for *a* and *b* spectral lines shown in Fig. 6.1

The InSe compound is a promising semiconductor material for solid-state electronics that retains stable physical parameters in time. Single-crystal test samples were also prepared by the Bridgman method. With a view to improve structural perfection and for ordering of polytypes, a long-term annealing with a gradual reduction of annealing temperature was used. The degree of monocrystallicity and structural perfection of samples were determined by X-ray topography methods, as well as NQR methods. The semiconductor compound InSe is characterized by NQR complex multiplet spectra, located in 4 ranges with the average frequencies 10.25 MHz; 20.5 MHz; 30.75 MHz and 41 MHz. Fig. 6.3 shows NQR spectrum of ^{115}In isotope in InSe after FFT of FID. The spectrum was obtained as a result of exciting a pulse of duration 3 μs and power 250 W at a frequency of 20.5 MHz. The registration temperature 20 ^{o}C.

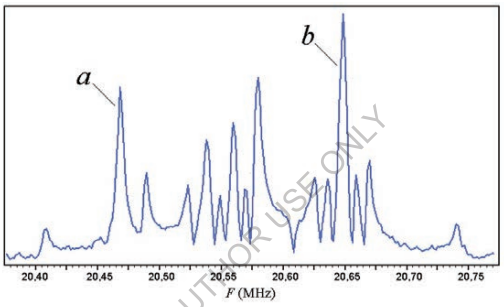

Fig. 6.3 NQR spectrum for ^{115}In isotope in InSe for spin transition at a frequency of 20.5 MHz

The temperature dependence of resonance frequency of ^{115}In was studied in the range of 0 ^{o}C to 100 ^{o}C (Fig. 6.4). The dependence was observed for two intensive spectral lines *a* and *b*. It was established that in this temperature range the temperature dependence of resonance frequency is close to linear. For InSe this result is different from the similar dependence in other compounds (for instance, $KClO_3$, $NaClO_3$), where it is, as a rule, nonlinear. Structural invariance of NQR spectra at temperature variation suggests the absence of any phase transitions in this temperature region. The relatively high frequency-temperature conversion ratio (2.35 kHz/degree) allows using the semiconductor compound InSe also as a thermometric material for high-precision thermometer based on NQR. In this case it is possible to create a standard thermometer with direct frequency-temperature conversion and the measurement accuracy at least 0.05 ^{o}C.

For performing the experiment, samples in the form of layered packages were used. The samples were made of single crystals grown by the Bridgman method. Reduction of crystal lattice defects was achieved by samples annealing at a temperature of 250 ^{o}C for 12 hours.

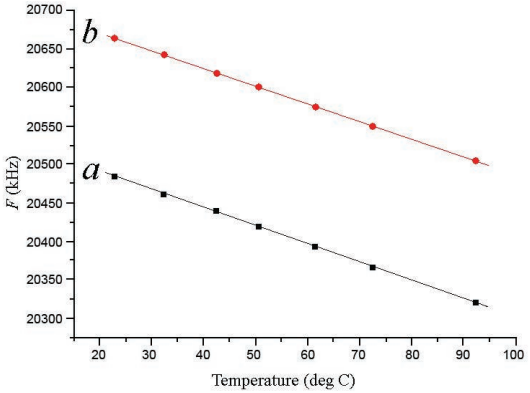

Fig. 6.4 Temperature dependence of NQR frequency for *a* and *b* spectral lines shown in Fig. 6.3

For the purpose of observing NQR, the pulsed method with Fourier transform of spin induction signals was employed. The dependence of NQR spectrum of ^{115}In in InSe on the pressure applied along the optical axis *c* was studied. The ^{115}In isotope has nuclear spin $I = 9/2$, and thus for NQR there are 4 spin transitions whose average frequencies are related as the integers 1:2:3:4. The instrumentally convenient third transition ($\pm 5/2 \leftrightarrow \pm 7/2$) with a frequency of ≈ 30.5 MHz was selected for the observation. Due to the presence of polytypes, the NQR spectra in InSe are quite complex (Fig. 6.5).

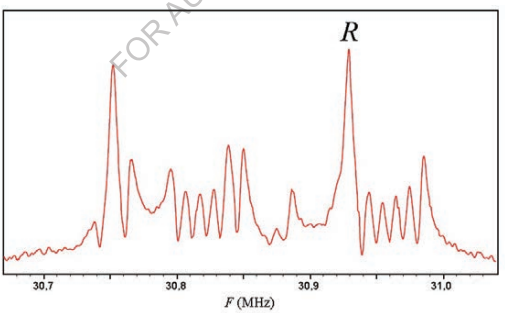

Fig. 6.5 NQR spectrum of ^{115}In in InSe in the initial crystal at atmospheric pressure and 25 °C. The *R* line is used to determine the dependence of *S*(*P*) intensity

As the pressure increases along *c* axis to 500 atm, the resonance spectrum intensity *S*(*P*) is attenuated. With intensity increase of individual lines, the spectrum shape is typically unvaried, indicating the absence of structural transformations in this pressure range. The samples were made as layered crystal packages of dimensions 7×8 mm^2 and thickness 3 mm clamped between two rigid sapphire plates (Fig. 6.6). To assure the rigidity and avoid bending of plates, the dielectric supports have been employed that fit into geometry of oscillating circuit coil.

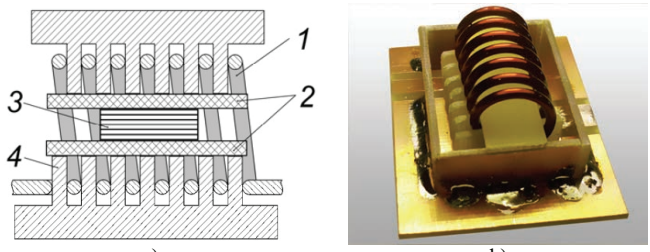

a) b)

Fig. 6.6 Sample pressure cell. Device section (a): 1 - NQR receiving coil, 2 – sample compression plates, 3 – oriented sample package, 4 – dielectric supports; real pressure cell (b)

The pressure value was regulated by a calibrated load applied to the sample in the manufactured high-frequency cell. Fig. 6.7a shows a change in the integral intensity of NQR spectrum due to applied pressure at a constant temperature of 25 ^{o}C. The plot in Fig. 6.7b represents a change in the amplitude of a single spectral line and is adequately described by a linear dependence within the limits of error.

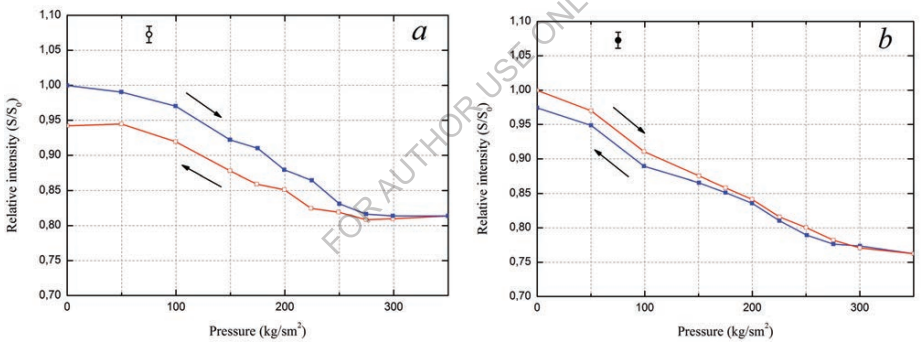

Fig. 6.7 Dependence of NQR spectrum parameters in InSe on the uniaxial pressure: integral intensity of resonance spectrum (a), peak intensity of a single spectral line *R* in Fig. 6.5 (b)

It was established that a deviation from the linear dependence in the range of 250 kg/cm^2 to 350 kg/cm^2 is due to noises caused by SNR reduction with pressure increase. This effect is more pronounced when calculating spectrum area (Fig. 6.7a) and less appreciable when defining the intensity of a single line (Fig. 6.7b). The latter was selected from the multiplet spectrum as the most intensive one (shown by letter *R* in Fig. 6.5). Resonance signal attenuation can be due to formation of a plurality of defects and the appearance of strain with increasing pressure on crystal, as noted in a series of papers, for instance in [4].

Measurement of resonance dependence was performed in a stepwise fashion: adjustment of fixed pressure, then a pause for crystal “shrinkage”, next – NQR spectrum registration with digital noise averaging. Spectrum reversion to initial inten-

sity after pressure relief from crystal served as a criterion for selection of pause duration. Similar results were obtained on a thinner package (1.5 mm thick), except that "shrinkage" time for InSe sample proved to be less by 30 % to 50 %.

The uniaxial pressure $F \| c$ was also created for a layered crystal GaSe. As shown by the previous experimental investigations, the specific feature of InSe crystal structure complicates the investigation of its peculiarities under uniaxial strain. First of all, it is rather difficult to assure the reciprocal character of applied pressures. It should be noted that in conformity with the assertions given in [2, 9], in the layered crystals the pressure $F \| c$ is, in fact, equivalent to the bulk pressure. With pressure increase, one should expect a change in the interlayer atomic bonds, as well as inter-plane distances. The latter should result in the modification of NQR spectra. However, despite the reversible character of NQR under pressure, the multiplet spectral structure was virtually unchanged up to 350 kg/cm^2. This emphasizes the fact that in given pressure area the crystal structure on the whole remains unchanged. The stability of resonance frequency for ^{69}Ga in GaSe shows that interatomic distances and angles between bond directions do not change appreciably. From the previous experiment it follows that the relatively lower elasticity of InSe crystals as compared to GaSe leads to considerable time of crystal mechanical relaxation after pressure relief, that is, to reconstruction of the initial NQR spectrum.

The modulus of elasticity C11 for InSe is 7.3×10^{12} Pa, and for GaSe – 10.3×10^{12} Pa [2]. Such difference is consistent with a faster reconstruction of NQR spectra in GaSe after pressure relief as compared to InSe. The shape of NQR spectra in GaSe is simpler and consists of two groups of lines (Fig. 6.1) caused by ε- and γ-polytype modifications [6].

Like in InSe, with increase in uniform pressure on the plane of layered package of crystalline GaSe, the resonance signal ^{69}Ga was monotonously attenuated. Two samples were investigated up to the pressure of 350 kg/cm^2 and 500 kg/cm^2 (Fig. 6.8). A change in spectrum intensity in the sample of dimensions $7\times8\times3$ mm^3 is shown in Fig. 6.8a. The value of pressure was controlled in the process of its gradual increase (curve *1*). The average time taken by one measurement was 30 min to 40 min.

For the dependence of GaSe line intensity shown in Fig. 6.8a, just as for InSe, a hysteresis is observed. It is evident that the area of hysteresis loop is related to stress and strain accumulation in the crystal. This is confirmed by the time necessary for the initial spectrum reconstruction after loading or unloading. Further pressure increase along the optical axis *c* results in sample plastic fracture. Plastic yield was observed under pressure at 600 kg/cm^2 to 700 kg/cm^2. Possible causes for InSe crystal failure at uniaxial pressure include structural defects and sample inhomogeneity.

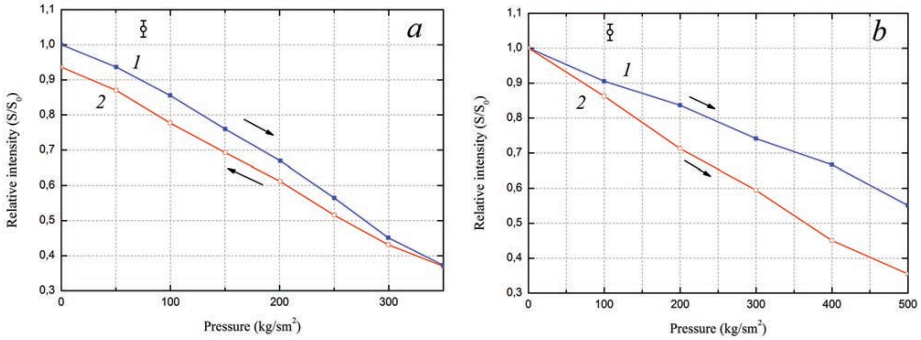

Fig. 6.8 Dependence of NQR signal intensity in GaSe with a change in uniaxial pressure on layered crystal package: peak intensity of resonance line ^{69}Ga with increase (1) and decrease (2) of pressure on the sample 7×8×3 mm^3 (a); integral intensity (1) and peak intensity (2) of the line with pressure increase for the sample 7×8×1.5 mm^3 (b)

6.2 Quality assessment of layer-structured semiconductor single crystals by nuclear quadrupole resonance method

The specific feature of InSe and GaSe semiconductor compounds is strong anisotropy of chemical bond which results, in fact, in crystal two-dimensionality with the ensuing physical properties [16, 17].

Undoped monoselenides are distinguished by low concentration of carriers ($\leq 10^{13} - 10^{14}$ cm^{-3}) and relatively low mobility (for InSe up to ~2×10^{-1} m^2/V·s, and for GaSe – 10 – 20 m^2/V·s) [18]. The salient feature of grown crystals is low electrical conductivity which, for instance, for undoped *n* – InSe is $10^{-1} - 10^{-2}$ S·m^{-1}. Low conductivity, especially in the direction of optical axis ***c***, provides a way for efficient use of high-frequency NQR and NMR radiospectroscopy for study of exactly monocrystalline samples, rather than powder materials. The possibility of studying the bulk undeformed samples by non-intrusive method is particularly important to obtain information on crystal structural perfection, the presence of defects, the nature of chemical bond. The absence of tangible skin-effect at frequencies up to 50 MHz offers the advantage of using NQR method in large-sized samples, specifically for ingots prepared by the Bridgman technique.

The elongated shape of cylinder ingot and preferred orientation of atomic layers along the direction of crystal growth enables one to use RF field of spectrometer coil for zone scanning of NQR over the entire length of grown single crystal.

With a view to achieve maximum intensity of NQR signal, the vector of RF field of spectrometer coil should be applied normal to atomic layers, namely parallel to optical axis ***c*** and, hence to axial symmetry axis of EFG [19].

The disadvantage of a two-way solenoid coil is expansion of working zone due

to inhomogeneous field which partially goes beyond the coil edges [20]. A saddle-shaped coil in which high-frequency filed vector is oriented normal to crystal growth direction, i.e. $\boldsymbol{B_1} \| \boldsymbol{c}$ (Fig. 6.9) is free from this disadvantage. With orientation of atomic planes in the direction of crystal growth, rotation of cylinder ingot about the geometrical symmetry axis results in two positions: $\boldsymbol{B_1} \| \boldsymbol{c}$ – condition of maximum signal intensity; $\boldsymbol{B_1} \perp \boldsymbol{c}$ – absence of signal. The availability of natural resonance line width, the presence of defects in the form of atomic lattice distortions and disorientation of crystal units even with axial symmetry of EFG in the case of $\boldsymbol{B_1} \perp \boldsymbol{c}$ leads to a tangible NQR signal [19].

To increase SNR under all other conditions, apart from increasing the volume of substance V and RF flux $\boldsymbol{B}_1$, it is necessary to improve the figure of merit of receiving coil. The use of samples in the form of cylinder ingots of layered material is acceptable for the observation of NQR, as long as the volume of coil is filled to the maximum and filling factor $\eta \approx 0.8 - 0.9$. In the presence of a container (glass ampoule) factor η can make 0.6 – 0.7.

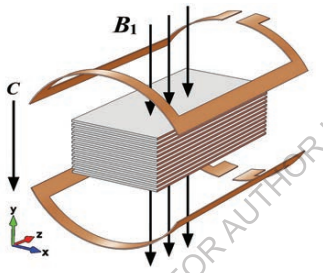

Fig. 6.9 Arrangement of layered crystal unit with respect to axes $\boldsymbol{c}$ and $\boldsymbol{B}_1$ of receiving saddle-shaped coil of NQR spectrometer

Comparison of the results obtained on the solenoid and saddle-shaped coils has shown that the latter yields spectra with better signal/noise ratio. This is particularly so with the influence of alien crosstalk and noise, which is attributable to a more homogeneous concentration of RF flux $\boldsymbol{B}_1$ deep into ingot. In the latter the radiation area is larger than coil dimensions and becomes blurred near the edge.

The experiment was performed with the use of NQR pulsed spectrometer with the output power of probing pulse 300 W [21].

By means of saddle-shaped coils the resonance spectra in the zones of monocrystalline *n*-type InSe ingot were consecutively observed. Crystal under study was placed in vacuum ampoule of diameter 18 mm, made of quartz glass. The spectra were registered as the ampoule with grown ingots (Fig. 6.10) travelled with respect to two-way coil with a selected step. Maximum resonance signal intensity is observed at crystal orientation – $\boldsymbol{B_1} \| \boldsymbol{c}$. Attenuation of signal intensity to minimal values occurs at crystal rotation about the symmetry axis of ampoule by 90°, which confirms the fact that in this monocrystalline ingot monoatomic In-Se-Se-In layers are arranged along the direction of crystal growth [19].

Comparison of spectra registered in different ingot zones suggests a conclusion on the homogeneity of crystal structure of this compound. The shape of multiple resonance lines is very responsive to distortions of crystal periodicity, the presence of deformation or impurity. Crystal lattice defects can be caused, for instance, by violation of technological modes of source materials preparation, in particular, crystal growth temperature instability or incorrect temperature mode of its annealing. Procedure of checking NQR spectra is especially helpful for crystals that passed thermal treatment. Criterion of crystal quality, in the first approximation, is linewidth and resonance spectrum resolution. Similar shape of spectra from different ingot zones, both in the intensity and multiplet configuration, allows claiming about the homogeneity and perfection of investigated single crystal region.

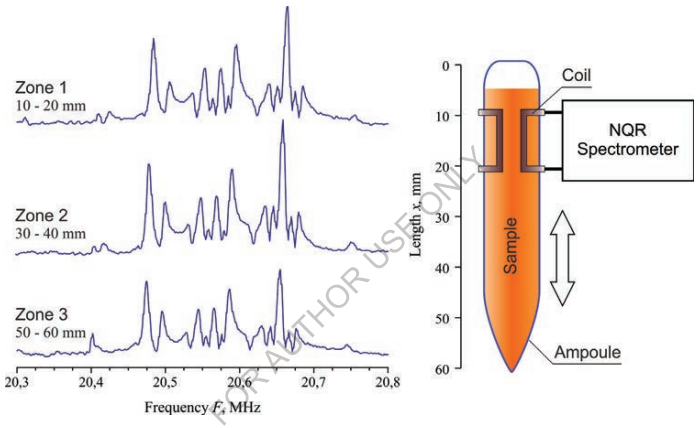

Fig. 6.10 Registration of NQR spectra in scanning mode along monocrystalline InSe ingot in the direction of crystal growth from the melt

Results of a more detailed investigation of monocrystalline InSe ingot by means of a saddle-shaped coil are represented as a spectrogram in Fig. 6.11, where NQR spectra were consecutively observed in the sample bulk zones. The spectra were registered along the ingot in the direction of crystal growth with a selected step of 1 cm. From the comparison of the spectra it is seen that resonance lines in D – F zones are fully identical, which points to structural ordering and homogeneity of crystal.

The initial plates of size 0.25 mm^2 from this ingot area were consecutively annealed in vacuum at temperatures 200 ^oC and 150 ^oC during 4 hours. The resulting *n*-InSe-*p*-InSe heterostructures under study had well-pronounced diode characteristics and satisfactory photoelectric parameters [22].

A marked reduction of NQR spectrum intensity in G – I zones is caused by sample volume reduction in RF field of the coil due to ingot conicity. A drastic reduction of signal intensity in B and C zones is related to precipitation of Zn impurity in the end part of the ingot.

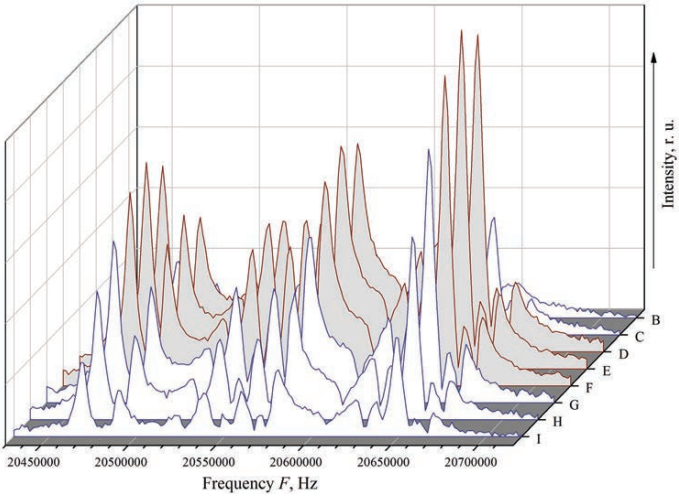

Fig. 6.11 Spectrogram of ^{115}In NQR in InSe obtained by coil travel along the ingot in the direction of crystal growth

6.3 The EPR and NQR in layered crystal of GaSe: Gd

Doping the layered semiconductor compounds of the A^3B^6 group with rare-earth elements imparts peculiar physical properties to the obtained materials. The anisotropy of the magnetoresistance in the crystals of GaSe: Gd was studied and the electroluminescence in the visible region of light was observed [23–25]. Experimental observations of the spin diffusion of a paramagnetic impurity by the NQR method are decisive, which is of particular importance when creating spintronics devices [26].

However, the question of the entry of gadolinium impurity into the GaSe crystal lattice remains unstudied. The authors of [18], from the electron paramagnetic resonance (EPR) spectra, showed realizing of the six types of Gd^{3+} paramagnetic centers in unannealed crystals. Whereas, after annealing in vacuum at 300 ^{o}C for 24 hours the mentioned crystals revealed strong simplification of the spectrum. At room temperature, a characteristic EPR spectrum is observed for the fine structure of Gd^{3+} [27]. At high temperatures (~ 300 ^{o}C), two types of nonequivalent impurity centers are observed, which can be account for the polytype structure of GaSe. The study of the orientational dependence of the EPR spectra led to the conclusion that the position of the Gd impurity has axial symmetry. In order to increase the resolution of the EPR spectra, we carried out studies of doped GaSe crystals at liquid nitrogen temperature. Three equivalent positions of the paramagnetic center of the Gd^{3+} ion, associated with the presence of polytypes in GaSe, have been established.

As it is already known, GaSe crystallizes in 4 polytypic modifications of β, ε, γ,

and δ. The formation of one or another polytype, or their mixture, essentially depends on the method of single crystals growing. In single crystals GaSe is grown from the melt (Bridgman, Czochralski methods), the ε-polytype is predominant [18]. As it is asserted, the smallest volume is occupied by the elementary cells of the ε- and β-polytypes, encompassing two layers and, at the same time, both modifications have hexagonal packing of layers (2*H*) with the same repetition period of the crystal structure. Such packing of layers in ε- and β-polytypes is difficult to distinguish in the diffractometric studies of such crystal structures. In particular, a change in crystal symmetry during the formation of polytypes leads to the redistribution of electron density in the lattice. That is why radio-spectroscopy methods are promising for structural studies of such materials. It's noteworthy, that the NQR spectra pointed out that the distinction between ε- and β-polytypic modifications was unambiguously established [27].

The GaSe single crystals grown by the Bridgman method were used for research. Doping with the impurity was carried out by introducing Gd at the rate of the composition of $Ga_{0,999}Gd_{0,001}Te$. A modified CEPR-2 spectrometer equipped with a goniometer and a low-temperature cryostat was used to observe the EPR spectrometr of Gd^{3+}. The samples were chopped plates 0,3 mm thick and 2×4 mm^2 in size. For the Gd^{3+} ion with the $4f^7$ electron configuration (the ground state of $^8S_{7/2}$), the EPR spectrum should consist of seven lines spanning rather wide range of magnetic fields.

A complex EPR spectra of Gd^{3+} consisting of several groups of lines of varying intensity in freshly grown crystals $Ga_{0,999}Gd_{0,001}Te$ were observed. After annealing the material in vacuum at the temperature of 300 ^{o}C for 24 hours, the spectrum became simpler, and the peak intensity of the lines decreased. The obtained EPR spectrum (Fig. 6.12) at 77 ^{o}K is a symmetric spectrum characteristic of the Gd^{3+} fine structure EPR (the numbers *1*, *2*, *3*, starting from the center line *"0"*, marked the high-field part of the spectrum).

The maximum length of the magnetic field at which the spectrum is observed is about 3 kGs. The width of each line in the spectrum did not exceed 4 Gs at 300 ^{o}K and dropped to about 2 Gs at temperature decrease down to 77 ^{o}K. The presence of the fine structure of the spectra and the relatively small width of the lines indicated a single entry of impurity ions and the absence of Gd-Gd pairs with exchange interaction. The position of the spectrum lines is practically independent of temperature in the range of 77 – 300 ^{o}K. However, a strong orientational dependence of the spectrum with respect to the external magnetic field B_0 is observed. In Fig. 6.12a the EPR spectrum is shown for a sample oriented in such a way that the main crystal axis $c \parallel B_0$. After the sample plate is rotated 90^o (in the position $c \perp B_0$), the full width of the spectrum decreases by a factor of about 2 (Fig. 6.12b). Note that when the sample plate is rotated, the structure of the spectra itself does not change, i.e., the lines

gradually moving do not change the order in the spectrum. The nature of the orientational dependence and equidistant arrangement of lines in the spectra indicates the axial character of the environment of the Gd^{3+} ion. The further confirmation to it is provided by the fact that the rotation of the sample plate with $c \perp B_0$ does not change the shape of the spectrum. Thus, we can conclude that the Gd^{3+} ion enters the hexagonal structure of the crystal by replacing one of the Ga atoms in the covalently bound Ga-Ga pair in the direction of the axis c. The axial location of the center is characterized by two values of the g-factor, which are determined by the location of the central line of the spectrum: $g_{\parallel} \approx 1{,}989$; $g_{\perp} \approx 1{,}992$.

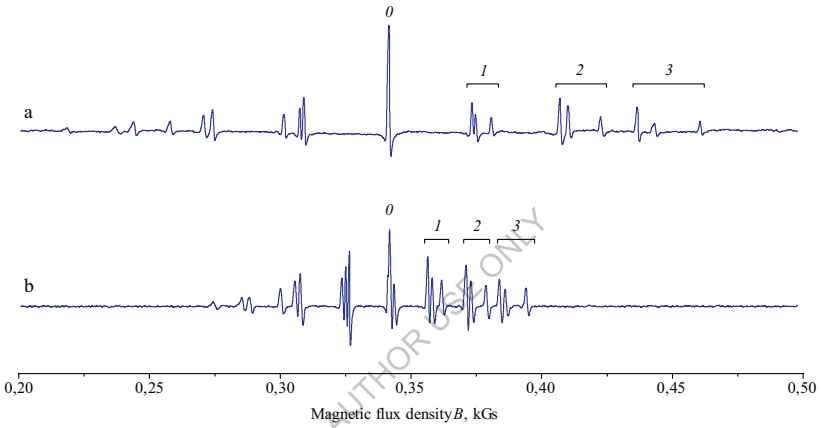

Fig. 6.12 The dependence of the EPR spectra of Gd^{3+} in GaSe: Gd on the mutual orientation of the main axis of the crystal c and direction of the magnetic field B_0: $c \parallel B_0$ (a); $c \perp B_0$ (b). The temperature of the spectra recording is 77 °K

Let us consider the options for the occurrence of the Gd impurity in the crystal matrix of a layered GaSe crystal. A possible mechanism for the entry of an impurity was discussed in [28]. The impurity can enter the covalent layer by replacing one of the two Ga^{2+} ions, or enter the interlayer space, creating bonds with the Se atoms, thereby forming compounds of the Gd_xSe_y type. In the latter case, the formation of more complex EPR spectra and broadening of spectral lines are likely [29]. The broadening process is also possible with the pair substitution of two Ga atoms in a covalent layer by two Gd atoms. However, the experiment reveals that there is a single inclusion of Gd into the GaSe crystal.

Let us find out the possible cause of the splitting of the lines of the Gd^{3+} EPR fine structure in GaSe. Obviously, there are three types of paramagnetic centers in GaSe: Gd, reflecting the equivalent states of an impurity in the crystal structure of a layered compound. This is also confirmed by the splitting of the central component of the spectrum into three lines with orientation of $c \perp B_0$ (Fig. 6.12b).

Let us consider the features of the formation of polytypes from the point of view of the crystalline environment of gallium ions. It was established that for the *β*-polytype, the geometrical arrangement of Ga ions with respect to Se ions in neighboring atomic layers is the same: Ga ions are located opposite to Se ions along with the *c* axis. However, in polytypic modifications *ε*- (and also *γ*-) as a result of the displacement of fourfold packets relative to other positions of gallium ions become nonequivalent. In this case, for part of the Ga ions, Se is located on one side along the *c* axis, and the intergap space is located on the other side (Fig. 6.13).

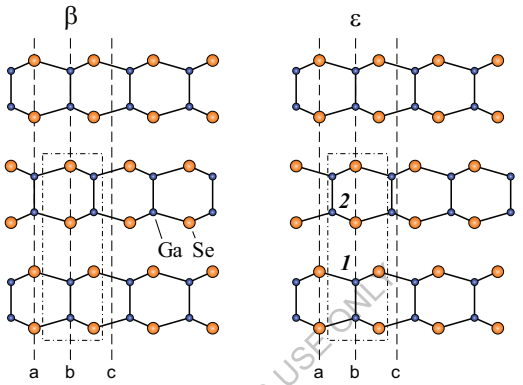

Fig. 6.13 The projection on the plane of the crystallographic structure (110) of two polytype modifications of GaSe. The dotted line highlights the elementary cells [30]

This fact is confirmed by the NQR spectra, which display two intense lines from Ga nuclei [31], indicating the difference in the electric field gradients in the positions of the nonequivalent position of gallium atoms.

For the *β*-polytype, all gallium ions are located in the crystal equivalently. The GaS compound crystallizes specifically in the *β*-modification, hence only one line is observed in the NQR spectrum [27]. Thus, in the *β*-modification there can only be one type of Gd^{3+} nodal center, in the direct vicinity of which along the *c* axis there are gallium atoms on one side, and those of selenium on the other, (Fig. 6.13, *β*, Ga-Gd-Se). In the *ε*-modification there can be two types of centers. One of them is identical to the Ga-Gd-Se center (indicated by *1* in Fig. 6.13), while the other has the center of the hexagonal cell next to Gd by the neighbor of the next layer (denoted by *2* in Fig. 6.13). Since two types of spectra are observed experimentally, it can be concluded that in this crystal the *ε*- and *γ*- polytypes prevail. The weak splitting of more intense side lines of the fine EPR structure can imply the presence of another polytype in the crystal, possibly a *β*-modification, which is thermodynamically unstable for GaSe [32]. The findings presented above prove that joint investigations with the use of the EPR and NQR methods make it possible to detect and identify polytypes in a layered GaSe crystal.

6.4 Conclusions

It is shown that semiconductor compounds GaSe and InSe can be used as thermometric substances with the application of nuclear quadruple resonance. The difference from the analogs of using other substances lies in the linear temperature dependence of resonance frequency in the temperature range of 250 ^{o}C to 390 ^{o}C with conversion slope 1.54 kHz/degree for GaSe and 2.35 kHz/degree for InSe. This affords opportunity to use digital readout of temperature directly, without complicated interpolation formulae. Stability and reproducibility of readings are assured by structural invariance of GaSe prepared by special annealing process of crystal grown by Bridgman method.

For the first time the effect of uniaxial pressure on NQR spectra in layered crystals InSe and GaSe was investigated to the values of 500 kg/cm^2. The pressure is applied along the crystal axis *c*. In the course of pressure increase on the surface of layered crystal, both the integral spectral intensity and the peak intensity of single lines are reduced. Resonance signal attenuation is unambiguously related to pressure increase. With pressure growth, the characteristic structure of resonance spectrum and NQR frequency do not alter appreciably, which testifies to the absence of phase transformations in crystals.

When measuring the pressure dependence of NQR, in semiconductor compounds InSe and GaSe a hysteresis is observed due to stresses and strains in a layered crystal. The use of layered compounds InSe and GaSe for measuring uniaxial pressure via NQR is possible at pressures up to 50 kg/cm^2 to 100 kg/cm^2, where hysteresis appearance is minor.

The possibility of research on the bulk samples of indium and gallium monoselenides by non-intrusive method is exceptionally important for efficient quality control of their structure as-grown by the Bridgman method. This is promoted by low conductivity of these monoselenides, which makes it possible to perform NQR studies in large volumes of semiconductor crystals.

In the investigation of the bulk samples of layer-structured semiconductor monocrystals by NQR method the best results were obtained with the use of a saddle-shaped coil of NQR spectrometer. Comparison of ^{115}In NQR spectra registered in different zones of InSe ingot allowed effective estimation of the homogeneity of crystal structure of this compound.

A joint study using the EPR and NQR methods makes it possible to detect and identify polytypes in a layered GaSe. From the fine structure of the EPR spectra a single occurrence of the Gd^{3+} impurity ion in a GaSe crystal with $g_{\parallel} \approx 1{,}989$; $g_{\perp} \approx 1{,}992$ was revealed. Fine correlation between the NQR and EPR spectra was observed, indicating that two groups of Ga atoms in GaSe are nonequivalent in the local

environment, which is due to the ε- or γ-polytypes. Additional splitting probably accounts for the presence of the β-modification phase in GaSe. The significant broadening of the NQR lines in GaSe: Gd and the orientational dependence of the EPR spectra on the magnetic field confirm that the Gd impurity (similarly to Ga atoms) is in the axial crystalline environment.

References

1. Khandozhko V., Raranskii N., Balazjuk V., Kovalyuk Z., Samila A. Temperature and baric dependence of nuclear quadruple resonance spectra in indium and gallium monoselenides. Proceedings of SPIE 9066 : Eleventh International Conference on Correlation Optics, Ukraine, Chernivtsi, 2013. Chernivtsi, 2013. P. 90661G-1–7.
2. Gatulle, M., Fische, M., Ciibvy, A., "Elastic constants of the layered compounds Gas, GaSe, InSe, and their pressure dependence, "Phys. stat. sol. (b) 119, 327-336 (1983).
3. Schwarz, U., Goni, A.R., Syassen, K. et all. "Structural and optical properties of InSe under pressure, "High Pressure Research 8, 396-398 (1991).
4. Pellicer-Porres, J., Segura, A., Munoz, V., "High-pressure x-ray absorption study of InSe, "Phys. Rev. B 60(6), 3757-3763 (1999).
5. Gauthier, M., Polian, A., Besson, J.M., Chevy A., "Optical properties of gallium selenide under high pressure, "Phys. Rev. B 40(6), 3837-3854 (1989).
6. Errandonea, D., Segura, A., Manjon, F.J. et all., "Crystal symmetry and pressure effects on the valence band structure of γ-InSe and ε-GaSe, "Phys. Rev. B 71(12), 125206(1)-125206(11) (2005).
7. Ruschansky, K.Z., "Vliyanie gidrostaticheskogo davleniya na staticheskie i dinamicheskie svoystva kristalla InSe: issledovaniya iz pervyh printsipov, "FTT 46(1), 177-184 (2004).
8. Drapak, S.I., Vorobets, M.O., Kovalyuk, Z.D. "Vliyanie odnoosnogo szhatiya na parametry fotopreobrazovaniya opticheskogo kontakta p-GaSe-n-lnSe, "FTP 39(5), 633-635 (2005).
9. Kovalyuk, Z.D., Pyrlya, M.M., Boledzyuk, V.B., Shevchik, V.V., "Pressure and strain sensitivity of InSe and GaSe layered semiconductors, "Ukr. J. Phys. 56(4), 366-370 (2011).
10. Pashayev, A.M., Gadjiyev, A.R., Tagiyev, T.B., Abbasova, T.M., "Hopping conductivity in GaSe monocrystals at low temperatures, "Semiconductor Physics, Quantum Electronics & Optoelectronics 4(4), 287-289 (2011).
11. Ismailov, A.A., Isakov, G.I., Ahmedzade, N.D., Shirinov, M.M., "Vliyanie generatsionno-rekombinatsionnyh protsessov na elektroprovodnost monokristallov GaS i GaSe, obluchennyh elektronami, "Mezhdunarodnyy nauchnyy zhurnal

"Alternativnaya energetika i ekologiya", NTC «TATA» 6(86), 48-51 (2010).
12. Geydarov, A., "Elektricheskie svoystva GaSe poluchennogo kosvennym metodom iz gazovoy fazy, "Zhurnal neorganicheskoy himii 52(10), 1618-1620 (2007).
13. Lashkarev, G.V., Dmitriev, A.I., Baida, A.A, Kovalyuk, Z.D., Kondrin, M.V., Pronin, A.A., "Anomalii staticheskoy I dinamicheskoy provodimosti monoselenida indiya, "Fizika i tehnika poluprovodnikov 37(2), 145-150 (2003).
14. Gorbatiy, V.R., "Suchasniy stan YaKR termometrii, "Sbornik nauchnyh trudov po materialam mezhdunarodnoy nauchno-prakticheskoy konferentsii SWORLD 2(3), 48-50 (2010).
15. Lastivka, G.I., Sidor, O.N., Kovalyuk, Z.D., Khandozhko, A.G., "Vliyanie otzhiga na spektry YaKR i harakteristiki geterofotodiodov GaSe-InSe, "Vostochno - Evropeyskiy Zhurnal peredovyh tehnologiy 4/5(46), 28-34 (2010).
16. Samila A. P., Lastivka G. I., Khandozhko V. A., and Kovalyuk Z. D. Prompt Quality Monitoring of InSe and GaSe Semiconductor Crystals by the Nuclear Quadrupole Resonance Technique. Semiconductors. 2016. Vol. 50, No. 8. P. 1034–1037.
17. Kyazym-zade, A.G., Agaeva, A.A., Salmanov, V.M., Mokhtari, A.G., "Optical detectors on GaSe and InSe layered crystals, "Technical Physics 52/12, 1611-1613 (2007).
18. Terhell, J.C.J.M., "Polytypism in the III-VI layer compounds, "Progr. Cryst. Growth and Characterization of Polytype Struct. 7, 55-110 (1983).
19. Kovalyuk, Z.D., Khandozhko, A.G., Lastivka, G.I., Samila, A.P., "The electric field gradient asymmetry parameter in InSe/ Semiconductor Physics, "Quantum Electronics and Optoelectronics 2, 164-166 (2011).
20. Brayilovskyy, V.V., Samila, A.P., Khandozhko, O.G., "Optymizatsiya topolohiyi napruzhenosti vysokochastotnoho polya davacha radiospektrometra, "Visnyk of Lviv Polytechnic National University 646, 46-51 (2009).
21. Khandozhko, A.G., Khandozhko, V.A., Samila, A.P., "Impulsnyy radiospektrometr YaKR s effektivnym podavleniem perehodnogo protsessa, "Vostochno - Evropeyskiy Zhurnal peredovyh tehnologiy 6/12(63), 21-25 (2013).
22. Khandozhko, V.A., Kudrinskiy, Z.R., Kovalyuk, Z.D., "Fotoelektricheskie svoystva geteroperehodov na osnove InSe I yadernyy kvadrupolnyy rezonans w iskhodnyh materialah, "Vostochno - Evropeyskiy Zhurnal peredovyh tehnologiy 1/5(61), 33-38 (2013).
23. Samila Andriy, Lastivka Galina, Khandozhko Alexander, Kovalyuk Zahar. The EPR and NQR in layered crystal of GaSe: Gd. Proceedings of SPIE 11369 : Fourteenth International Conference on Correlation Optics, Ukraine, Chernivtsi, 2019. Chernivtsi, 2020. P. 1136919-1–5.

24. Gürbulak, B., Yildirim, M., Tüzemen, S., Efeoglu, H., Yogurtçu Y.K., "Temperature dependence of galvanomagnetic properties for Gd doped and undoped p-type GaSe, "J. Appl. Phys. 83(4), 2030-2034 (1998).
25. Abay, B., Glider, H.S., Efeoglu, H., "Excitonic absorption and Urbach-Martienssen tails in Gd-doped and undoped p-type GaSe, "Semiconductor science and technology 15, 535-541 (2000).
26. Furman, G.B., Goren, S.D., "Spin Diffusion Barrier near Paramagnetic Impurities in Pure NQR, "Z. Naturforsch 57a, 307-314 (2002).
27. Bastow, T.J., Cambell, I.D., Whitfeld, H.J., "A 69Ga, 115In NQR study of polytypes of GaS, GaSe and InSe, "Sol. St. Com. 39, 307-311 (1981).
28. Slyn'ko, V.Ye., Khandozhko, A.G., Kovalyuk, Z. D., et al., "Ferromagnetic states in the In1-xMnxSe layered crystal, "Phys. Rev. B. 71, 255301-1-5 (2005).
29. Yarembash, Ye.I., Eliseev, A.A., [Khal'kogenidy redkozemel'nykh elementov], Nauka, Moscow, 260 (1975).
30. Depeursinge, Y., Baldereschi, A., "Polytypism and layer-layer interaction in the III-VI layer semiconductor, "Physica 105b, 324-328 (1981).
31. Kovalyuk, Z.D., Slyn'ko, Ye.I., Khandozhko, O.G., "Yadernyy kvadrupol′nyy rezonans v politypnykh spolukakh GaSe ta InSe, "Fizyka i khimiya tverdoho tila 2(4), 579-583 (2001).
32. Brodin, N.S., Blonsky, I.V., [Eksitonnyye protsessy v sloistykh kristallakh], Naukova Dumka, Kyiv, 256 (1986).